Photon Management in Thermal and Solar Photovoltaics

by

Lu Hu

Submitted to the Department of Mechanical Engineering
in partial fulfillment of the requirements for the degree of

Doctor of Philosophy in Mechanical Engineering

at the

MASSACHUSETTS INSTITUTE OF TECHNOLOGY

September 2008

Author .....
Department of Mechanical Engineering
August 27, 2008

Certified by .....
Gang Chen
Warren and Towneley Rohsenow Professor
Thesis Supervisor

Accepted by .....
Lallit Anand
Chairman, Department Committee on Graduate Students

Photon Management in Thermal and Solar Photovoltaics

by

Lu Hu

Submitted to the Department of Mechanical Engineering on August 27, 2008,
in partial fulfillment of the requirements for the degree of
Doctor of Philosophy in Mechanical

Abstract

Photovoltaics is a technology that directly converts photon energy into electrical energy. Depending on the photon source, photovoltaic systems can be categorized into two groups: solar photovoltaics (PV) and thermophotovoltaics (TPV). In solar photovoltaic systems, the photon source is the sun, whereas in thermophotovoltaic systems the photons are from artificially designed thermal emitters that operate at a lower temperature. The differences in the photon sources lead to different research emphases on the two photovoltaic systems in this work. This thesis investigates ways to control photon emission and absorption for solar energy and TPV applications. Several topics are discussed, including photon transport in multilayer structures, measurement of near-field thermal radiation, optical absorption in silicon nanowire structures, surface-plasmon enhanced near-bandgap optical absorption in silicon, and selective absorber surface for solar thermal applications.

For thermophotovoltaic systems, the work is focused on thermal emission and photon transport. The study of photon transport in multilayer structures is presented. Results based on wave-optics and ray tracing methods are compared. The analysis shows that for structures contain a large number of layers, the coherence length of the emitting source is no longer a valid criterion to indicate whether ray tracing method is valid. Instead, wave inference effects always play a role. The effects of photon localization are also discussed.

Surface-mode enhanced near-field thermal radiation is explored in this work as an effective way to tailor the thermal emission for TPV systems. Calculations based on fluctuation-dissipation theorem and Maxwell's equations are presented to study radiative heat transfer between two closely-spaced glass plates. The theoretical analysis shows that the radiative heat transfer between closely-spaced glass plates is enhanced by surface phonon polaritions and the flux can exceed the far-field upper-limit imposed by Planck's law of blackbody radiation. An experimental system was built to test near-field radiative heat transfer between two parallel glass plates, and the experimental results show good agreement with the theoretical predictions.

For solar photovoltaics, the emphasis in this work is on improving optical absorption in silicon-based cells. Two nanostructures, silicon nanowire arrays and silicon embedded with small silver particles, have been analyzed as potential candidates for solar energy

harvesting. The study on silicon nanowire structures reveals that nanowires have desirable antireflection characteristics. Several parameters, such as the length and diameter of the nanowires as well as the spacing between the wires, have been studied to provide the basis for the optimization of nanowire based solar cells. The study shows that nanowire structures have low reflectance over a broad spectrum and can absorb short-wavelength photons efficiently. However, the analysis also indicates that silicon nanowire is not efficient in absorbing long-wavelength photons. Longer wires in comparison to the thickness of dense films are generally required to compensate low absorption of the near-bandgap photons.

The analysis of surface-plasmon assisted photon absorption is presented to address the problem of inadequate absorption of near-bandgap photons in silicon. Instead of increasing the optical path of photons for more absorption, surface plasmons are explored to enhance the local electromagnetic field and thus the optical absorption. An extended Mie scattering formulation is used to calculate the optical absorption around spherical silver particles embedded in silicon. It is found that local field enhancement by surface plasmon can lead to 50 times more absorption near the bandgap of silicon. An analytical model is developed to study the concentration effects of the surface plasmon field. It is shown that the net absorption gain reaches maximum when the spherical shell surrounding the particle has an outer diameter of 1.26 times of the particle diameter. The absorption loss in the metallic sphere, however, is a main obstacle to overcome.

Finally, a different approach of solar energy utilization is discussed in this work. Selective absorber surfaces are studied for solar thermal energy harvesting. The surfaces consist of subwavelength periodic metallic structures. Finite-Difference-Time-Domain (FDTD) analysis is conducted on the metallic structures. The effects of lattice spacing and structure thickness are presented. The numerical simulation indicates that the metallic structures have good spectral selectivity: high absorptance in visible range and low emittance in infrared. Fabrication of the selective absorber surface is attempted. Preliminary experimental results are given in this work. As a proof of concept, nickel is plated in porous anodic aluminum. The resultant structure shows good spectral selectivity which is not found in bulk nickel or aluminum.

Thesis Supervisor: Gang Chen
Title: Warren and Towneley Rohsenow Professor

Dedication

To my wife, for her love and support.

Acknowledgments

The road toward Ph.D. is certainly a long yet exciting journey. I have been fortunate for being continuously receiving generous help and encouragement along the way. I am grateful to all the individuals who helped me to make this journey possible.

My most sincere thanks go to my thesis advisor, Professor Gang Chen. Looking back, I feel very grateful for Gang to give me the opportunity to join the nanoengineering group. Gang is a fantastic mentor and a constant source of inspiration. No matter how busy he is, he is always willing to put aside his own work for a discussion. Gang is also the most responsive and diligent advisor that I have worked with. He could always be counted on to quickly give back his comments on every draft paper I sent to him. It is his guidance and support that made me a better researcher in the field of nano science and nano engineering.

I would like to thank my thesis committee members, Professor John Lienhard and Professor Borivoje Mikic, for their encouragement and guidance. The stimulus discussions with them have been instrumental in shaping my thesis. Without their encouragement, chapter 6 would not be possible. I also want to thank Professor Peter So for helpful discussions on the near-field thermal radiation experiment, and Dr. Yong Zhang and Dr. Shuo Chen for their assistance on SEM imaging.

I have benefited greatly for working with the members in the nanoengineering group. Dr. Bao Yang and Dr. Ronggui Yang, who are now professors at University of Maryland at College Park and University of Colorado at Boulder, gave me tremendous help and set great examples for me when I first joined the group. Special thanks go to Dr. Arvind Narayanaswamy, who is now a professor at Columbia University, for collaborating on the near-field thermal radiation experiment. I am indebted to Dr. Xiaoyuan Chen for

collaborating on more than half of my thesis work. Dr. Chen's expertise and insights in optics are invaluable treasure to the group, from which I certainly benefit the most. I also want to express my gratitude to Professor Ruiting Zheng for offering generous help on electrochemistry, and to Jinwei for helpful discussions. Our UROP student Derek Li helped me tremendously on preparing aluminum samples. Daniel helped me with the FTIR measurement. I particularly want to thank the officemates and colleagues that made my stay at MIT an enjoyable experience, especially Tom and Aaron, who joined the group in the same year as I did. It has been a pleasant experience of spending all these years together in the same group. I also want to thank Ase, Jim, Shin and Shireen for all the delightful moments and friendship over the years.

Last but not least, I owe a great debt to my wife, Xin. Without her love, patience and constant encouragement, this thesis work would not be possible. Finally, I want to thank my parents for their unconditional love and support. I hope that I have made you proud.

Contents

List of Figures

List of Tables

Chapter 1

Introduction and Background

In both thermophotovoltaic (TPV) and solar photovoltaic (PV) systems, the energy in photons is directly converted into electricity in the photovoltaic cells. The two technologies share significant similarities in operational principles. Photons from electromagnetic radiation are the driving energy source for both technologies. During operation, the photons from the illuminating source are intercepted by the photovoltaic cells, which are usually composed of semiconductor materials. The photons are absorbed in the photovoltaic cells and electrons are excited from valence band to conduction band to generate electron-hole pairs. The photogenerated positive (holes) and negative (electrons) charges are then separated across the semiconductor p/n junction and collected on the electrodes to generate electricity.

Key differences do exist between TPV and solar PV energy conversion. Although photons for both systems arise from electromagnetic radiation, or more exactly, thermal radiation, the temperatures of the thermal radiators are drastically different for these two types of photovoltaic energy conversion systems. In TPV systems, the thermal radiators are artificially designed emitters. The typical surface temperature of the thermal emitters is in the range of 1300 – 1800 K [1], where the peak of the spectral radiative flux lies in the infrared spectrum. In a solar PV, the photons are received from the sun which has a surface temperature of approximately 5777K, where the peak radiation is in the visible spectrum (0.4 – 0.7 μm), corresponding to photons with higher energies compared to those in the infrared spectrum [2]. To ensure high photo-electric conversion efficiency, it is important to match the radiation spectrums with the bandgap of the photovoltaic cell.

The differences in the photon spectrums lead to different requirements for the photovoltaic cells in the TPV and solar PV systems. Higher bandgap semiconductor materials such as silicon are widely used in solar PVs [3, 4], while lower bandgap materials such as semiconductors from the III-V family are employed for TPVs to ensure sufficient conversion efficiency of the infrared spectrum [1]. In comparison to the solar PVs, TPVs have an additional flexibility in terms of system optimization: the spectrum of the emitters can be tuned to match the photovoltaic cells. High-power narrow-band emitters with emission peak slightly above the bandgap of the PV cell are desired for maximum conversion efficiency [1]

Numerous studies have been devoted to the development of photovoltaic cells for improved internal quantum efficiencies, including the first, second, and third generations of solar cells and the III-V family semiconductor photovoltaic cells for TPV applications. Interested readers should refer to reviews [1, 3, 4], which provide thorough summaries of the research status in photovoltaic cells. This thesis work is focused on an equally important issue in the TPV and solar PV energy conversion – photon management, which includes two aspects: photon generation and photon absorption. As mentioned earlier, both photovoltaic systems rely on photons from thermal radiation as the energy source. The photons for solar PV are from the sun and the characteristics of the solar spectrum are relatively fixed. Consequently, in this work the emphasis for solar PV will be on improving photon absorption in the photovoltaic cells. In contrast, for TPV systems, the focus will be on the thermal emitters, including emission-filter design and thermal radiation spectrum tuning. In this chapter, a general introduction and the related background information will be given to far-field and near-field thermal radiation, and selective absorption of the solar spectrum for energy conversion.

1.1 Thermal radiation: far-field and near-field

Among the three modes of heat transfer – conduction, convection and radiation, thermal radiation is unique in terms of the mechanism of energy transport. For conduction, energy is carried by electrons or phonons in solids; in gases and liquids, energy is conducted by molecular collisions. For convection, energy is transported by macroscopic flow motion of fluid particles. Both conduction and convection require the presence of media for the energy transport. In contrast, the energy of thermal radiation is carried by electromagnetic waves which do not require a medium to propagate. Unlike the other energy carriers, photons can travel a long distance before they are scattered, which is also a unique characteristic of thermal radiative energy transport.

From a microscopic point of view, electrons and ions in any matter are in constant random thermal motion at a finite temperature. The thermal motion of charges generates randomly oscillating electric currents in the medium, giving rise to electromagnetic radiation. Since the thermally-excited electromagnetic radiation is chaotic in nature and contains a broad spectrum of energy states, the resultant radiation spectrum is broad and consists of electromagnetic waves with different wavelengths. The radiated photons are in thermal equilibrium with the radiating matter. Consequently, the distribution and intensity of the thermal radiation spectrum depends on the temperature and the optical properties of the specific material.

When describing the radiation characteristics of real objects, it is useful to introduce the concept of a blackbody. A blackbody is an idealized object that can emit the maximum radiative energy at a given temperature. Max Planck is the first one that successfully explained the blackbody radiation and gave the spectral distribution of blackbody emission [5]:

$$I_{\lambda b}(\lambda,T)=\frac{2hc_0^2}{n^2\lambda^5\left[\exp\left(hc_0/n\lambda k_bT\right)-1\right]} \tag{1}$$

where h and k_b are the Plank and Boltzmann constants, respectively, λ is the wavelength in vacuum, T is the absolute temperature of the blackbody, c_0 is the speed of light in vacuum, n is refractive index of the transparent medium that surrounds the blackbody surface, and subscript b denotes blackbody radiation. Further investigation of Eq. (1.1) reveals that the radiation intensity has a maximum at a wavelength that obeys Wien's displacement law [2]:

$$\left(n\lambda T\right)_{\max}=2898\ \mu m\cdot \mathrm{K} \tag{2}$$

The wavelength is often referred to as the peak wavelength of thermal radiation. It is clear that peak wavelength is inversely dependent on temperature, where higher temperature leads to smaller peak wavelength and vice versa. For example, blackbody radiation from the sun has a maximum at 0.50 μm which is in the visible range. Blackbody radiation at room temperature (300 K) has a maximum shifted to 9.7 μm. A related quantity is the coherence length of thermal radiation, which length is often employed as an indication of whether the transport falls into the wave regime or the particle regime [6, 7]. The coherence length of thermal radiation is given by [8]:

$$l_c=2167.8\ \mu\mathrm{m}\cdot\mathrm{K/T} \tag{3}$$

1.1.1 Far-field radiation

Cautions need to be taken when applying Planck's law of blackbody radiation (Eq.(1.1)). In his work [9], Planck clearly states that "*Throughout the following ... the linear dimensions of all parts of space considered, as well as radii of curvature of all*

surfaces ... are large compared with the wavelengths of the rays considered". It suggests that the Planck's law is applicable only when the characteristic scale of the objects is larger than the wavelength of the thermally radiated electromagnetic waves, i.e. the far-field scenario. The peak wavelength of thermal radiation is usually chosen as a characteristic wavelength for the whole thermal radiation spectrum. For most applications, the far-field description of thermal radiation is sufficient, since the peak wavelength of thermal radiation at room temperature is 9.7 μm, which is much smaller than the length scales of the objects.

In the far-field regime, the calculation of radiative heat transfer between objects is relatively straightforward. The radiative properties (emissivity and reflectivity, etc.) of an object are associated with the specific object and thus can be determined independently. The properties will not change in the presence of another object (e.g. an emitter surface or a radiation receiver surface). The radiative heat transfer can then be calculated based on energy balance and the geometric relations between objects. An example is the radiation network method for solving the radiative heat exchange between surfaces, which can be found in many heat transfer text books [10, 11]. Parameters needed for the far-field radiative heat transfer calculation include emissivity, reflectivity, transmissivity and absorptivity. These four quantities are correlated by energy balance and Kirchoff's law. The energy balance requires

$$\rho + \tau + \alpha = 1 \tag{4}$$

Kirchoff's law relates the monochromatic directional emissivity to the monochromatic directional absorptivity:

$$\varepsilon_\lambda(\theta, \varphi, T) = \alpha_\lambda(\theta, \varphi, T) \tag{5}$$

which states that a matter at thermal equilibrium emits the same amount of radiative energy as it absorbs in a specific wavelength and a specific direction. Kirchoff's law essentially is a requirement imposed by the second law of thermodynamics and has deep physical root in the principle of detailed balance [12]. Equation (5) also suggests that a thermal emitter at a specific wavelength must be optically absorptive at the same wavelength.

1.1.2 Near-field radiation: theory and experiment

The radiative transfer problem belongs to the near-field regime when the peak wavelength of thermal radiation is much less than the distance between objects. Evanescent modes of electromagnetic fields exist on the surfaces of thermal emitters. These surface modes have high energy density, quantified by large photon local density of states (LDOS) [13-15]. As indicated by their name, the evanescent modes do not propagate in the direction normal to the surface. Instead, the magnitude of these modes decays rapidly and vanishes at a distance comparable to the wavelength. The evanescent modes usually do not contribute to the radiative heat flux since they do not carry energy across the interfaces between objects and stay localized. However, when a second surface is brought into the proximity of the first surface, a backward-decaying evanescent mode is formed on the second surface, which couples with the forward-decaying evanescent mode on the first surface. The coupled evanescent waves generate modes that carry energy in the direction normal to the surfaces, the magnitude of which depends on the distance between the objects as well as the temperatures.

In the near-field regime, the radiative properties of a surface are no longer quantities that are independent of neighboring objects. Instead, the emissive power of a surface can be altered by the presence of another surface and has a strong dependence on the gap between the surfaces. Unlike calculations for far-field thermal radiation, the

approach employing Planck's law plus Kirchoff's law is no longer valid for near-field radiation. To calculate the near-field radiative flux, a direct calculation is required which traces back to the origin of thermal radiation: the random thermal motion of charges. The pioneering work by Rytov is among the first to model the thermal radiation phenomenon from a microscopic point of view, where random thermal electromagnetic fields are obtained by solving statistical Maxwell's equations [16, 17]. Polder and Van Hove simplified Rytov's approach by taking thermally-generated electric currents as the radiation source and using the fluctuation-dissipation theorem to determine the radiation magnitude [18]. Polder and Van Hove's approach was the most widely adopted formalism for calculating near-field thermal radiative heat transfer. The method was followed by a number of researchers for various applications, with improvement in the mathematical treatment of Maxwell's equations by introducing the dyadic Green's functions [19]. Examples include modeling near-field thermal radiation enhanced by surface waves [20-22], analyzing thermal radiation in one-dimensional photonic crystals [23], and studying thermal emission control with multilayer thin films [24]. It should be noted that all these analysis did not take into account the effects of nonlocal dielectric constants. Instead, macroscopic dielectric constants were used for the calculation. The macroscopic treatment may become problematic when distances between objects are comparable to the spacing of atoms. More recently, the nonlocal effects are studied by Chapuis *et al* by distinguishing the transverse and longitudinal components of the permittivity [25].

It is not surprising to see that the earliest experimental efforts on near-field thermal radiation are related to cryogenics, where the peak wavelength of thermal radiation is much longer due to reduced temperature so that near-field radiative heat transfer becomes important. The experimental study on near-field thermal radiation in the US began in Tien's group in 1960s, where Domoto *et al* measured radiative heat transfer between two metallic surfaces at cryogenic temperatures for gaps between 50 μm and 1 mm, reporting an increase in radiative heat transfer with decreasing spacing, but the

maximum radiative heat transfer was only 1/29 of that predicted by the Planck's law [26]. Hargreaves pushed the measurements to gaps as small as 1 μm between two chromium surfaces, which gave a radiative heat transfer rate at 50% of the blackbody upper limit [27]. Xu *et al* measured the radiative heat flux between a squeezed indium needle and a planar thermocouple for reduced gap sizes between 50 nm and 200 nm, but the experiment is inclusive due to the sensitivity of the technique [28]. More recently, Kittel *et al* measured near-field radiative transfer between a scanning thermal microscope tip and a flat substrate and reported saturated radiative flux as the gap approaches zero [29]. Interpretation of their experimental data, however, is complicated by the complex geometry of the tip.

One potential application for near-field thermal radiation is thermophotovoltaic power generation. The large power density and the pseudomonochromatic nature of the emission spectrum are beneficiary to thermophotovoltaic systems, whose efficiencies increase for high photon fluxes and narrow-band emitters [21, 30, 31].

1.2 Solar spectrum and selective absorption of photons

Solar radiation can be approximated as thermal radiation from a blackbody at 5777K, which corresponds to a large total emissive power at the surface of the sun, approximately 63.2 MW/m^2. However, the earth is separated from the sun by a large distance (1.49×10^{11}m), leading to a small view factor (2.18×10^{-5}) between the sun and the earth [32]. The experimentally measured extraterrestrial solar power received on the earth outer surface is approximately 1367 W/m^2 [33]. The solar irradiation is further reduced by scattering and absorption as it penetrates through the atmosphere. The exact solar irradiation spectrum and intensity received at the earth surface vary by geological locations and atmosphere conditions, making it difficult to chart the performance of PV devices since PV devices are spectrally selective and the measured performance depends

on the incident spectrum. To standardize the performance evaluation of PV devices, the American Society for Testing and Materials (ASTM), the PV industry and government research and development laboratories, define two terrestrial solar spectral irradiance distributions (ASTM G173) for selected atmosphere conditions [34, 35].

1.2.1 Air Mass 1.5 spectra

Figure 1-1 is a reproduction of the standard reference spectra based on the ASTM G-173 data [34]. The extraterrestrial spectrum, plotted in red, is a compilation of experimentally measured solar irradiance outside the earth's atmosphere. The extraterrestrial spectrum serves as the basis for calculating the reference terrestrial spectra. The curves in blue and black colors are the global tilt and direct plus circumsolar spectra, which are terrestrial spectra calculated through the use of radiative transfer models with specified atmosphere conditions [36]. The term "global", which more accurately should be "total", means the irradiance include both direct radiation from the sun and the diffusive irradiance from the sky and the ground. The receiving surface is assumed to be tilted 37^{o} from the horizontal. A detailed definition of the placement of the receiving surface and a drawing can be found in [37]. The direct plus circumsolar spectra is the sum of the direct beam irradiance from the sun, and the forward diffusive scattering toward the receiving surface within $\pm 5^{o}$ angle to the surface normal [38]. The reference spectra are also called the Air Mass (AM) 1.5 spectra, which are representative of solar spectra under average conditions in the United States. Air mass refers to the relative path length of the direct solar beam through the atmosphere. AM 1.5 corresponds to a 48.2^{o} angle of the sun from the zenith (path length ratio of $1.5 = 1/\cos 48.2^{o}$) [37]. The absorption bands of the gases are clearly shown in the figure on the global tilt and directional irradiance curves.

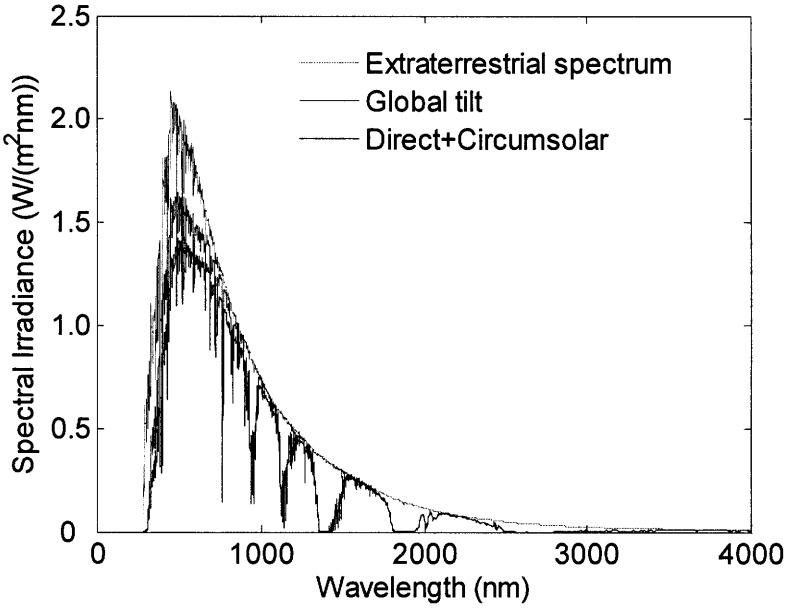

Figure 1-1: The Air Mass (AM) 1.5 solar spectral irradiance. The extraterrestrial spectrum is a compilation of experimentally measured solar irradiance outside the earth's atmosphere. The global tilt and directional plus circumsolar spectra are terrestrial spectra calculated through the use of radiative transfer models with specified atmosphere conditions.

The total solar irradiance intercepted by the earth is 1.74×10^5 TW, which is enormous compared to the 13 TW power consumed by the entire human society (2005 data) [39]. Despite the fact that one hour of the solar irradiance delivers more energy than the earth uses in one year, solar generated power is only a tiny fraction of the world's power consumption. The gap between the actual usage of solar power and its immense potential is partly due to the low efficiency and high cost of the available technologies. Currently there are two major technologies that convert solar irradiance into electricity: solar photovoltaics and solar thermal. For both technologies, the absorption of the solar irradiance is a critical factor in determining the overall system efficiency as well as the cost. Solar PV and solar thermal, however, have different emphasis on the spectrum. Before further elaboration of the two technologies, the fraction of solar irradiance is defined to quantify the distribution of the AM 1.5 solar power:

$$f(\lambda) = \frac{\int_0^{\lambda} I_s(\lambda)\, d\lambda}{\int_0^{\infty} I_s(\lambda)\, d\lambda} \tag{6}$$

The denominator is the total power of the AM 1.5 solar spectrum, obtained by integrating the AM 1.5 data set. The numerator is the power contained in the spectral range between 0 and λ.

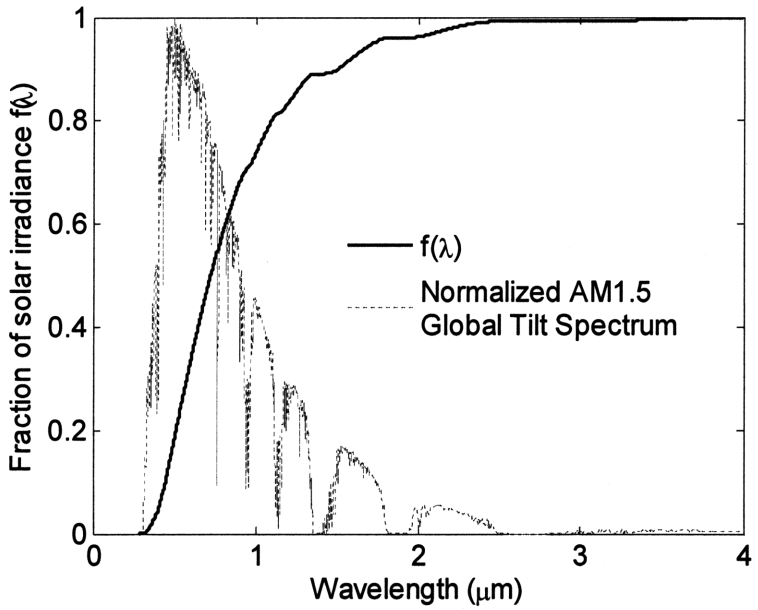

Figure 1-2: The fraction of solar irradiance based on the AM 1.5 global tilt data. More than 95% percent of the solar energy is contained from 0.28 μm to 1.8 μm. At the bandgap of silicon (1.1 μm), the fraction is 0.8.

Figure 1-2 shows the fraction f(λ) as a function of the wavelength. Below 0.28 μm, the solar energy is negligible and the fraction is zero. More than 95% of the solar energy is concentrated in the spectrum from 0.28 μm to 1.8 μm. Another number of the interest is the fraction at the bandgap (1.1 μm) of crystalline silicon, which is 0.8.

1.2.2 Selective absorption of the solar spectrum

The solar photovoltaic and solar thermal systems have different targets for the absorption of the solar spectrum, which will be separately addressed in the following sections. In solar photovoltaic systems, an important parameter is the bandgap of the photovoltaic cells. Although various materials have been proposed for photo-to-electric energy conversion (examples include Si, SiGe, CdTe, CIS, polymer and dye-sensitized TiO_2 [40, 41]), silicon based PV units still almost completely dominate the market. Ironically, silicon is far from the ideal material for photo-to-electric power conversion. At room temperature, crystalline silicon has a bandgap at 1.1 eV, translating to a vacuum wavelength of 1.1 μm. The optical property of silicon is plotted in Fig. 1-3 in terms of penetration depth:

$$\delta = \frac{\lambda_0}{4\pi\kappa} \tag{7}$$

where λ_0 is the wavelength in vacuum and κ is the extinction coefficient (the imaginary part of the optical constant). The penetration depth measures the distance that the electromagnetic wave can travel before decays away. Larger penetration depth corresponds to weaker optical absorption and requires thicker materials to capture photons at the corresponding wavelength.

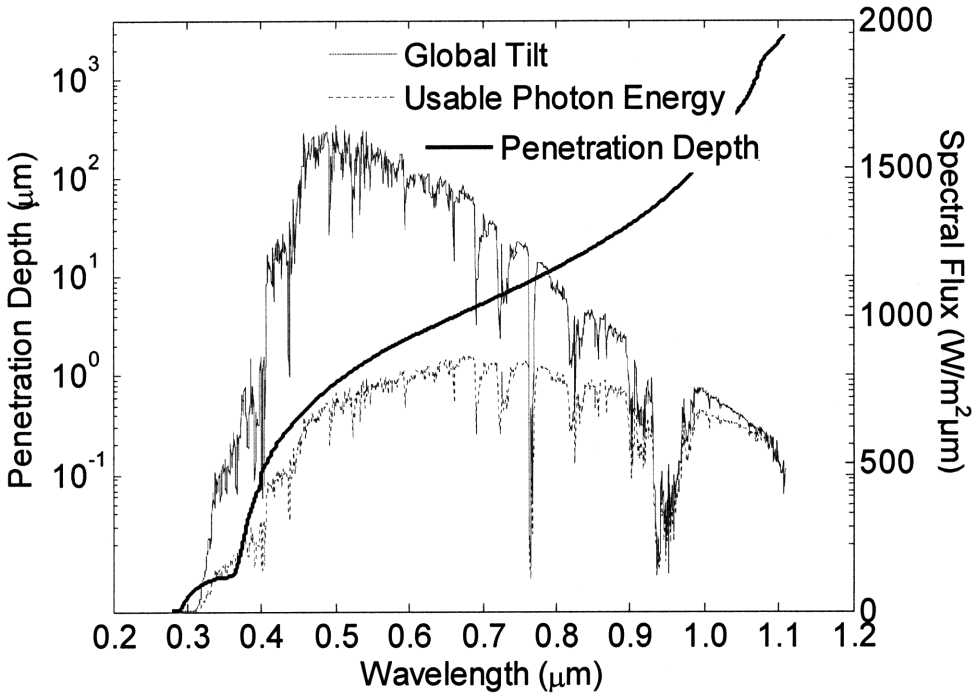

Figure 1-3: The penetration depth of crystalline silicon, plotted in log scale. The AM 1.5 global tilt spectrum and the usable photon spectrum are given in the same figure as references, plotted in linear scale.

The penetration depth of crystalline silicon is shown in Fig. 1-3, plotted in log scale. For wavelengths shorter than 0.7 μm, the penetration depth is 8.0 μm. The penetration depth almost increases exponentially for beyond 0.8 μm, suggesting very weak absorption of photons. The AM 1.5 global tilt spectrum is given in the same figure as a reference. A plot of the usable photon energy spectrum is also presented. The usable photon energy is defined as

$$I_u(\lambda) = I_0(\lambda)\frac{\hbar\omega_g}{\hbar\omega} = I_0(\lambda)\frac{\lambda}{\lambda_g} \tag{8}$$

where $I_0(\lambda)$ is the incident solar irradiance, $\hbar$ is the Plank's constant divided by 2π, $\hbar\omega$ is the photon energy, and λ_g is the wavelength corresponding to the bandgap of the photovoltaic cell. For the curve presented in Fig. 1-3, a bandgap of 1.1 μm is used. Equation (8) essentially states a one-photon process. Any photon that has energy above the bandgap of silicon can excite a pair of electron and hole. However, the excessive energy that exceeds the bandgap will relax into heat, which is counted towards the energy that can be converted into electricity. Correspondingly, we use the term "usable photon energy" to define the portion of energy flux that can be used to generate electricity.

The photons just above the bandgap have the largest usable energy. Ideally, solar cells made of silicon should selectively absorb photons above the bandgap to maximize conversion efficiency and reject photons below the bandgap to minimize temperature increase. However, as shown in Fig. 1-3, photons near the silicon bandgap need to travel more than 1000 μm to be absorbed. The inability to absorb long wavelength photons imposes technical challenges to solar cells based on silicon materials. Thick silicon layers are required to completely absorb all the photons above the bandgap, which not only impairs carrier collection but also increases the cost on materials [40, 42]. In addition, flat silicon surface has a high natural reflection of more than 30% in the visible spectrum, which can cause significant reduction in the overall energy conversion efficiency [43]. A number of techniques have been developed to increase photon absorption and reduce reflection in silicon. Commonly used methods include specially designed anti-reflection surface treatment to minimize reflection from the frontal surface and roughen the back surface to diffuse light inside the silicon layer [43-48]. However, applying textures to the surface may lead to increased electron-hole recombination and decreases the carrier collection efficiency [49]. An alternative way to increase long-wavelength photon absorption is to use noble metal particles as localized photon absorption centers to enhance the optical absorption [49, 50].

Solar thermal power generation is a completely different way of using the solar spectrum. Unlike solar PV systems, solar thermal power generation converts photon energy into heat, which then drives heat engines to generate electricity [51, 52]. Therefore, solar thermal electricity generation potentially can use up to 100% of the solar irradiance given complete absorption of the solar spectrum. However, loss mechanism does exist in the optical absorption process. Solar thermal systems rely on solar absorber surfaces to convert photons into heat. These surfaces not only serve as optical absorbers, but also emit photons at longer wavelengths in the infrared regime. Since the absorber are at elevated temperatures under working conditions, the thermal radiation from the surfaces is significant and may even be the primary heat loss mechanism. Therefore, an ideal selective surface for a solar thermal system requires complete absorption of the solar spectrum and near-zero thermal emissivity in the infrared. A wide range of selective absorbers for solar thermal applications are introduced in [53].

1.3 Mathematical tools for solving Maxwell's equations

This work covers the optical transport phenomena in three energy conversion systems, which may appear to be divergent topics. However, they not only share similarities in operating principles (solar PV vs. TPV), but also have common mathematical backgrounds. All the structures that are studied in this work have characteristic length smaller or comparable to the wavelength of interest, which require solving Maxwell's equations to fully take into account the electromagnetic wave interference, near-field effects, and diffraction effects. Different techniques are chosen to solve Maxwell's equations, which are best suited for the specific problem depending on the geometries as well as optical properties.

In chapter 2, multilayer structures are studied, where an analytical transfer matrix method is applied to solve the plane wave scattering in the simple 1-dimensional (1D)

system. In chapter 3, the problem of near-field radiative heat transfer is solved by tracing back to the origin of thermal radiation and summing up the contribution of all the random current sources. Therefore, an integral equation approach with the dyadic Green's function technique is implemented to calculate thermal radiation emitted by point current source. In chapter 4, we are dealing with periodic 3-dimensional (3D) nanowire systems, for which no analytical solutions are known to exist. A numerical transfer matrix method is employed to solve the light scattering from the nanowire structures. The 3D transfer matrix method is a finite difference frequency domain method, which is particularly suitable for general materials whose dielectric functions do not follow a Drude or Lorentz model [54]. In chapter 5, light scattering is studied for metal particles embedded in silicon. Because the standard Mie theory cannot be applied to absorbing hosting media, a modified Mie scattering scheme is used for spherical particles embedded in silicon. Finally, in chapter 6, light interaction with periodic structures is explored. The dielectric functions of metals follow Drude and Lorentz models, which is suitable for the Finite-Difference Time-Domain (FDTD) method. We apply FDTD method because one of the major advantages of FDTD is that the response of a structure to a wide range of frequencies can be obtained with a single run by applying a broad band pulse as the source. Although in theory the FDTD method can be applied to any materials, the simulation can be greatly simplified if the dielectric function of a specific material can be expressed with Debye model, Drude model, or Lorentz model [55].

In addition to the summary, all these analytical and numerical techniques will be introduced in specific chapters with more detailed background information regarding each topic.

1.4 Outline of thesis

The purpose of this thesis is to study photon transport in solar photovoltaic and thermophotovoltaic systems, as well as solar thermal applications. Because of the differences in the photon sources, different emphases are given to the three systems. For thermophotovoltaic systems, the focus will be on emitter design, aiming at increasing photon flux as well as spectrum monochromaticity. The spectrum of interest is the infrared. For solar photovoltaic systems, optical absorption on the receiver end will receive the attention. The target material to be studied will be silicon, which is the dominant semiconductor material in the solar photovoltaic industry. The interaction of light with nanostructures in the solar spectrum will be discussed. In the end, the thesis will provide analysis for selective absorber surface, dealing with both the solar spectrum and the infrared spectrum.

Chapter 2 presents theoretical study of thermal radiative transport through multilayer structures. Multilayer films are often used in TPV systems as emission filter. Two approaches are generally used to model the photon transport in films: ray tracing and wave optics, which treat photons as particles and waves, respectively. It is generally believed that ray tracing methods can be applied to study the optical properties of single and multilayer thin dielectric films (up to 3 layers) when the layer thickness is larger than the coherence length of the radiation field. However, this criterion has not been tested for multilayer systems containing a large number of layers. In this chapter, radiative properties are studied for one-dimensional dielectric multilayer structures illuminated by blackbody radiation sources. The total hemispherical transmittances are calculated for periodic structures and structures with random variation in layer thickness, using wave optics and ray tracing methods. Simulation results show that for periodic structures, the transmittance calculated using wave optics approaches a nonzero constant value with an increasing number of layers, while the transmittance obtained using the ray tracing

method asymptotically approaches zero. For random structures, the transmittance given by wave optics drops to zero at different rates depending on the order of random variations in layer thickness. It is found that the wave interference effect always plays a role when dealing with multilayer structures that contain a large number of layers. The results are explained based on extended and localized waves.

In chapter 3, near-field radiative transfer between two glass plates (precision optical flats) are studied. The optical flats are made of amorphous SiO_2, which supports surface phonon polariton, a surface mode that contains a large energy density. In this work, small polystyrene particles are used as spacers to maintain a micron-sized gap between two optical flats. By carefully choosing the number of particles and performing the measurement in a high-vacuum environment, the experiment is designed to ensure that the radiative heat flux is the dominant mode of heat transfer (more than 98% of the total heat flux). The experimental results clearly demonstrate that the radiative heat flux across micron-sized gaps can exceed the far-field upper-limit given by Planck's law of blackbody radiation. A direct calculation, which traces back to the origin of thermal radiation, is performed to model the near field thermal radiation between two glass plates, where the fluctuation-dissipation theorem and Green's function approach are employed [17, 19]. The measured radiative heat flux shows reasonable agreement with theoretical predictions.

In chapter 4, the optical absorption is analyzed for a new type of nanostructure photovoltaic cells – cells based on silicon nanowire arrays. Nanowire arrays are of interests to third generation solar cells either as electrodes or as photosensitive regions. Efficiency of such photovoltaic devices requires effective photon capturing. In this chapter, the optical absorption in silicon nanowire arrays is studied by solving the full-wave vector Maxwell equations using the 3D transfer matrix method. The effects of wire diameter, length and filling ratio on the optical absorption of nanowire arrays are investigated. The study reveals that nanowire arrays with moderate filling ratio have much lower reflectance compared to thin films. In high frequency regime, nanowire

arrays have higher absorptance than their thin film counterparts. While in the low frequency regime near the silicon bandgap, adequate absorption of photons requires longer wires with lengths comparable to the thickness of the films.

In chapter 5, we address the issue of inadequate optical absorption in silicon for the long-wavelength regime. Plasmons are collective oscillations of the conduction band electrons excited by incident electromagnetic waves. Under proper conditions, surface plasmons can be excited and bounded to the surface of objects that contain large population of free electrons. Surface plasmons are known to be able to enhance the intensity of local electric field, which can lead to potential applications in solar photovoltaic applications. An extended Mie scattering theory is used in this work to analyze the surface-plasmon enhanced light absorption in silicon. The calculation results show that the optical absorption in silicon can be enhanced up to 50 times at resonance frequency by embedded spherical silver nanoparticles due to the local field enhancement by surface plasmons. The analysis reveals that the surface-plasmon field is concentrated in a spherical shell that encloses the particle. The enhancement reaches maximum when the thickness of the shell is 0.26 times of the radius of the particle. The maximum absorption enhancement is found to be induced by silver particles with intermediate radii. The enhancement with larger particles is limited by the retardation effect, while the smaller-particle assisted absorption is hampered by electron scattering on the particle surface.

In chapter 6, we turn to the design and fabrication of selective absorbers. The selective absorber is a critical component in solar thermal applications. An ideal selective absorber should have the ability to absorb photons in the solar spectrum while minimizing radiation heat loss in the infrared. However, such materials do not exist in nature. Metals are known to be highly absorptive due to strong electron interaction with light. The challenge with metals is that they are too absorptive and have large optical constants which mismatch with the vacuum and thus reflect most of photons back. We propose a 3D photonic structure featured with submicron sized metal cones. The

theoretical analysis is based on the FDTD method. The calculations show that with a lattice spacing of around 100 nm and a length around 1 μm the proposed structure has the desired optical properties. Fabrication of the structures has been attempted in the lab. Preliminary experimental results show that the structure has reasonably good spectral selectivity.

Chapter 7 summarizes the findings and results presented in chapter 2 to chapter 6. Potential future studies are discussed and suggested.

Chapter 2

Radiative Transport in Multilayer Structures

2.1 Introduction

The coherence theory of light deals with the correlation of electromagnetic fields at two space/time points. To measure the correlation, the coherence length of waves was introduced and has been used extensively as a scale for observation of interference phenomena [56]. The coherence length is often employed as an indication of whether the transport falls into the wave regime or the particle regime. In the particle regime, ray tracing methods, i.e. energy methods can be used and the intensity of the electromagnetic fields is directly superposed. On the other hand, in the wave regime, it is the fields that need to be superposed, where the phase and amplitude of the electromagnetic waves are obtained by solving Maxwell's equations. Optical coherence theory has been employed to analyze radiative properties of single layer and multilayer thin films with a small number of layers (up to 3 layers) [6, 7, 57, 58]. These studies found that in general, the wave method results approach the ray tracing results when the films are much thicker than the coherence length of the radiation field, which for blackbody radiation is of the order of the wavelength given by Wien's displacement law [8, 59-62]. Based on these studies, it is generally assumed that ray tracing methods can be applied to study the optical properties

of single and multilayer thin dielectric films when the layer thickness is larger than the coherence length of the radiation field.

The above conclusion, however, has not been tested for structures with a larger number of layers. In recent years, studies on the phonon transport, which shares many similarities to photon transport in periodic structures, suggest that this may not be the case. It was observed that the phonon transmissivities in superlattices calculated from the wave method and from the ray tracing method do not approach each other, but the cause of this phenomenon was not elaborated [63]. The similarity between phonon and photon transport leads us to believe that similar behavior will occur for the thermal radiative properties of multilayer structures and prompts us to re-examine the coherence of blackbody radiation in multilayer structures. In the present work, we study the total hemispherical transmittance of alternating multilayer thin film structures, using both the wave method and the ray tracing method, for periodic structures and structures with random thickness variations. The simulation results show that for perfectly periodic structures, wave optics yields a transmittance that soon approaches a nonzero plateau for a large number of layers. The ray tracing result asymptotically approaches zero as the inverse of the number of layers. The transmittance given by wave optics drops to zero at different rates depending on the order of random variations of thickness added to the perfectly periodic structures. These behaviors are observed for both thin and thick layers, as compared to the coherence length of the blackbody radiation. These results imply that for one-dimensional multilayer thin film structures with perfectly aligned interfaces, there may not be an incoherence regime in which the ray tracing method can be applied.

The phenomenon, although surprising from the coherence length point of view, may be explained by localization theory, which addresses the problem of wave propagation in disordered media. The localization theory was proposed by Anderson in his classic paper to study the quantum transport of electrons in crystal lattices [64]. He found that the absence of diffusion, i.e. localization, occurs with the introduction of randomness to the lattice potential. Researchers soon discovered that almost all classic

wave equations have localized solutions when solved for a random medium [65, 66]. The localization of electromagnetic wave has been experimentally observed [67]. A proper scaling theory for the exponential decay of the localized modes has also been developed [68]. It was found that all the states in one or two-dimensional systems can be localized in the presence of infinitesimal disorder, while in three-dimensional systems, the picture is not very clear since some modes may not be localized even with a high degree of disorder [69-71].

Although our current study is mainly focused on fundamental understanding, the 1-D multilayer structures may find potential applications in thermophotovoltaic devices for radiation spectral control [72]. Compared to 2-D or 3-D photonic crystal structures [73, 74], the geometries of 1-D structures are much simpler and are more easily fabricated. Better understanding of radiation transport in multilayer structures is also critical in rapid thermal processing [58], and in solar applications where multilayer structures are widely used as optical filters [75].

2.2 Physical models and formalism

A model structure is shown in Fig. 2-1. It consists of multiple layers of thin films. In the current model, two non-absorbing materials with refractive indices of 4 and 2, respectively, are considered. These refractive indices are chosen arbitrarily, although there are close to those of some common materials. Absorption is not included because the focus is on the fundamental behavior of electromagnetic (EM) waves in periodic structures. Absorption can create artificial damping of waves that masks the phenomenon to be addressed in this work. A pair of layers forms the "unit cell" of the multilayer structure.

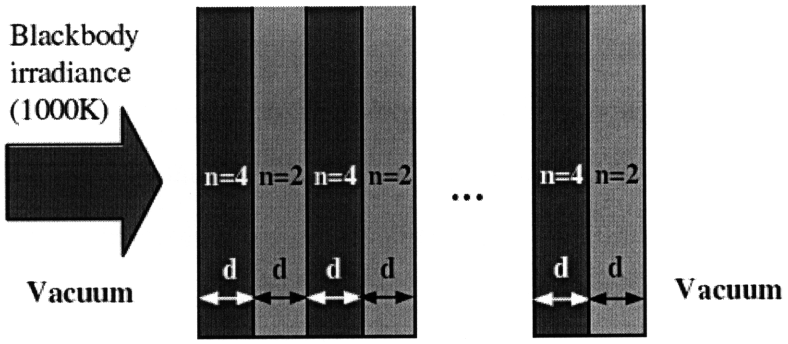

Figure 2-1: Schematic of the multilayer structure. The "unit cell" consists of two non-absorbing materials which have refractive indices of 4 and 2, respectively. The thickness of individual layer is d.

The multilayer structure is in vacuum and blackbody radiation is incident on one side of it. The spectral distribution is of the form (Planck's distribution),

$$I_{\lambda b}(\lambda,T)=\frac{2hc_0^2}{\lambda^5\left[\exp\left(hc_0/\lambda k_bT\right)-1\right]} \tag{1}$$

where h and k_b are the Plank and Boltzmann constants, respectively, λ is the wavelength in vacuum, T is the absolute temperature of the blackbody, c_0 is the speed of light in vacuum, and subscript b denotes blackbody radiation. In the present work, only temporal coherence of the blackbody radiation is considered. The coherence length of a blackbody radiation field is given by [8]

$$l_c=0.15\frac{hc}{k_bT}, \tag{2a}$$

and in vacuum, it can be rewritten as

$$l_c T = 2167.8\ \mu\text{m}\cdot\text{K} \tag{2b}$$

where c is the speed of light, and the other symbols have the same definitions as in Eq. (1). The expression in Eq. (2b) is very similar to Wien's displacement law [71]:

$$\lambda_{\max} T = 2897.8\ \mu\text{m}\cdot\text{K} \tag{3}$$

where $\lambda_{\max}$ is the wavelength corresponding to the peak blackbody radiation at a given temperature T. In this sense, in a homogeneous medium, the coherence length relates to the effective wavelength of the blackbody radiation. According to Eq. (2a), the coherence lengths at 1000K in n=2 and n=4 are 1.08 μm and 0.54 μm, respectively. For simplicity, the smaller value is taken as the coherence length l_c in the following text.

In our models, the multilayer structures are assumed to be one-dimensional. Surface roughness and nonparallelism are not considered. The disorder is introduced by varying the film thicknesses, i.e., adding a uniform random distribution to the nominal layer thickness. Wave optics and ray tracing methods were used to predict the overall transmittance of the structures. We further ignore the spatial coherence properties of the blackbody radiation source. At each angle of incidence, the incoming blackbody radiation is approximated by a plane wave.

2.2.1 Wave optics

The transfer matrix method is used to calculate the transmittance and reflectance for the multilayer structure [56]. These are standard methods for thin film structures and will not be explained in detail here. The transmittance of a multilayer structure containing m layers can be calculated from,

$$T_m = 1 - R_m = 1 - \left| \frac{(m_{11} + m_{12} p_{m+1}) p_0 - (m_{21} + m_{22} p_{m+1})}{(m_{11} + m_{12} p_{m+1}) p_0 + (m_{21} + m_{22} p_{m+1})} \right|^2 \quad (4)$$

where 0 and m+1 denote the materials adjacent to the first layer and the last layer, respectively, and m_{ij} is the element of the 2×2 overall transfer matrix M of the multilayer structure, which is the product of the transfer matrix of individual layers,

$$M = \prod_{j=1}^{m} M_j = \begin{bmatrix} m_{11} & m_{12} \\ m_{21} & m_{22} \end{bmatrix} \quad (5)$$

where

$$M_j = \begin{bmatrix} \cos\varphi_j & -\frac{i}{p_j}\sin\varphi_j \\ -ip_j \sin\varphi_j & \cos\varphi_j \end{bmatrix} \quad (6)$$

The elements in M_j are given by

$$\varphi_j = \frac{\omega n_j d_j \cos\theta_j}{c_0} \quad (7a)$$

$$p_{j,TM} = \sqrt{\frac{\mu_j}{\varepsilon_j}} \cos\theta_j \quad (7b)$$

$$p_{j,TE} = \sqrt{\frac{\varepsilon_j}{\mu_j}} \cos\theta_j \quad (7c)$$

where j denotes the j-th layer, counting from the side of incident radiation, ω is the frequency of the incident electromagnetic (EM) waves, n is the refractive index of the corresponding layer, d represents the layer thickness, θ is the angle which the propagation

direction of the wave makes with the normal to the layer interface, and ε and μ are the electric permittivity and magnetic permeability of the corresponding layer, respectively. The acronyms TM and TE represent transverse magnetic polarization and transverse electric polarization, respectively. It is assumed here that $\mu=\mu_0$ (permeability in vacuum) for all the layers, which is true for most materials in the infrared wavelength range.

2.2.2 Ray tracing

Ray tracing is extensively employed in designing optical instruments, analyzing radiation heat exchange through windows, etc. When the wavelength is far less than the feature size of the medium, Maxwell's equations reduce to the eikonal equation, which is the basis of geometric optics [56], or the ray tracing method. The ray tracing method tracks the trajectories of light rays and applies the laws of reflection and refraction successively. This method determines the paths of light rays based on simple geometric rules and excludes any possible interference effects.

For multilayer structures, the following recursive formulas have been developed for calculating the reflectance and transmittance of multilayer films [76].

$$R_m = R_{m-1} + \frac{\rho_{m,m+1} T_{m-1}^2}{1-\rho_{m,m+1} R_{m-1}} \tag{8a}$$

$$T_m = 1 - R_m \tag{8b}$$

where the results are for a structure with m layers, $\rho_{m,m+1}$ is the reflectivity (TE or TM) at the interface between layer m and outside medium (m+1), which can be calculated from,

$$\rho_{m,m+1(TM)} = \left(\frac{n_m \cos\theta_{m+1} - n_{m+1} \cos\theta_m}{n_m \cos\theta_{m+1} + n_{m+1} \cos\theta_m} \right)^2 \tag{9a}$$

$$\rho_{m,m+1(TE)} = \left(\frac{n_m \cos\theta_m - n_{m+1} \cos\theta_{m+1}}{n_m \cos\theta_m + n_{m+1} \cos\theta_{m+1}} \right)^2 \tag{9b}$$

2.2.3 Total hemispherical transmittance

The transmittance given in the above is the spectral directional value. Blackbody irradiance is isotropic, but each monochromatic component at a specific incident angle can be viewed as a plane wave. Integration over all angles and wavelengths is needed to calculate the total hemispherical transmittance of the multilayer structure. The spectral hemispherical transmittance for TE or TM waves is obtained by integrating over the hemisphere:

$$T_{\lambda,p} = \frac{\int_{\varphi=0}^{2\pi} \int_{\theta=0}^{\frac{\pi}{2}} T(\lambda,\theta) I_{b,\lambda} \cos\theta \sin\theta d\theta d\varphi}{\int_{\varphi=0}^{2\pi} \int_{\theta=0}^{\frac{\pi}{2}} I_{b,\lambda} \cos\theta \sin\theta d\theta d\varphi} = 2\int_{\theta=0}^{\frac{\pi}{2}} T(\lambda,\theta) \cos\theta \sin\theta d\theta \tag{10}$$

where p denotes the polarization status TE or TM, $T(\lambda,\theta)$ is given by Eq. (4) or (8b) depending on wave or ray tracing approach, and I_λ is the Plank distribution given by Eq. (1). The polarized total hemispherical transmittance can be calculated based on the spectral hemispherical transmittance in Eq. (10):

$$T_p = \frac{\pi \int_0^\infty T_{\lambda,p} \cdot I_\lambda d\lambda}{\sigma T^4} \tag{11}$$

where $\sigma = 5.67 \times 10^{-8}\,\mathrm{W/m^2 \cdot K^4}$ is the Stefan-Boltzmann constant. Blackbody radiation is unpolarized. The electric field has no definite orientation and can be resolved into equal TE and TM components. Then the unpolarized total hemispherical transmittance is the average of T_{TE} and T_{TM} :

$$T = \left(T_{TE} + T_{TM}\right)/2 \tag{12a}$$

Similarly, the unpolarized spectral hemispherical transmittance is given by

$$T_{\lambda} = \left(T_{\lambda,TE} + T_{\lambda,TM}\right)/2 \tag{12b}$$

2.2.4 Scaling of localization

Localization is a result of wave interference. Destructive interference of reflected and scattered waves effectively cancels the waves (in the case of an external incident wave) or confines the wave in a finite region (in the case of a source inside the medium). The localization length is often used as a measure of the attenuation of waves in random media. The definition of the localization length in one-dimensional systems is given by [77, 78]:

$$l = -\frac{2L}{\langle \ln T \rangle} \tag{13}$$

where L is the total thickness of the medium and $\langle \ln T \rangle$ is the ensemble average of the logarithmic transmittance. Equation (13) is a simple scaling rule which depicts the exponential decay behavior of localized waves. In our model, the individual layers have the same base thickness, we express the localization length in terms of the number of

layers. The localization length is determined by the randomness of the system as well as the frequency of the incoming waves. For a given frequency, the intensity of localized waves decays exponentially along the propagation direction, where the decay rate depends on the disorder of the medium. As an example, we calculated the spectral directional transmittance for normal incident waves. With random variation in the layer thickness being on the order of $4l_c$, the localization lengths for 1 μm and 2.898 μm waves are 5 layers and 10 layers, respectively. The latter wavelength is corresponding to the maximum intensity given by Eq. (3).

Rigorously, this definition is only valid when L is infinitely long. However, in computer simulations or experiments, only systems with finite dimensions can be dealt with. The localization length is thus being used as a comparison scale. For $l < L$, the waves will almost decay to zero at the boundary. In this sense, the system is effectively infinite to the waves with localizations lengths less than L and these waves exhibit exponential decay. For waves with a localization length l larger than the system length L, the transmittance may not obey exponential decay [77].

2.3 Results and discussion

Numerical methods were used to calculate transmittance, integrated over both wavelength and angle. For a temperature of 1000K, 99% of blackbody radiation emissive power is concentrated between 0.1μm and 30μm, which were selected as the integration upper and lower limits, respectively. The evaluation of transmittance based on ray tracing is straightforward. However, in the case of wave optics, due to interference effects the corresponding transmittance value is very sensitive to frequency change. It exhibits highly oscillatory behavior and needs special treatment for numerical integration. There exist some standard methods for integrating highly oscillatory triangular functions [79], but in general there is no preferred method for an irregularly oscillatory integrand such as

Eq. (4). We found that Simpson's method [80] with twice as many grid points is generally more effective than other more advanced integration techniques such as the Gaussian-quadrature family which is ideal for smooth functions, considering both computational time and accuracy. For integration over the incident angle, fewer grid points were used since the transmittance-angle function is smooth. Typically 40 grid points can yield satisfactory accuracy.

2.3.1 Periodic structures

In this work, periodic structures are defined as systems consisting of layers with identical thickness. As shown in Fig. 2-1, the multilayer structure is formed by alternating non-absorbing layers of the same thickness but different indices of refraction. For a system containing an even number of layers, the "unit cell" consists of two layers which have refractive indices of 4 and 2, sequentially. For a system containing odd number of layers, the first layer has a refractive index of 4 and the rest of the system can be viewed as constructed with a unit cell which still consists of double layers but with switched positions, i.e., 2 and 4, sequentially. The results for the odd and the even number of layers differ slightly but the trends are similar in all cases. For convenience, we will only present results for systems containing even number of layers while all the conclusion also hold true for odd layer systems.

If the individual layer thickness is less than the coherence length, interference effects are expected. Figure 2-2 shows the transmittance value with respect to the number of total layers for layer thickness smaller than the coherence length. The transmittance curves vary according to the layer thickness, which suggests strong wave interference in the systems. The result obtained using the ray tracing method is also plotted in the same figure for comparison. As expected, the ray tracing result does not agree with those obtained using wave optics because interferences of the waves exist.

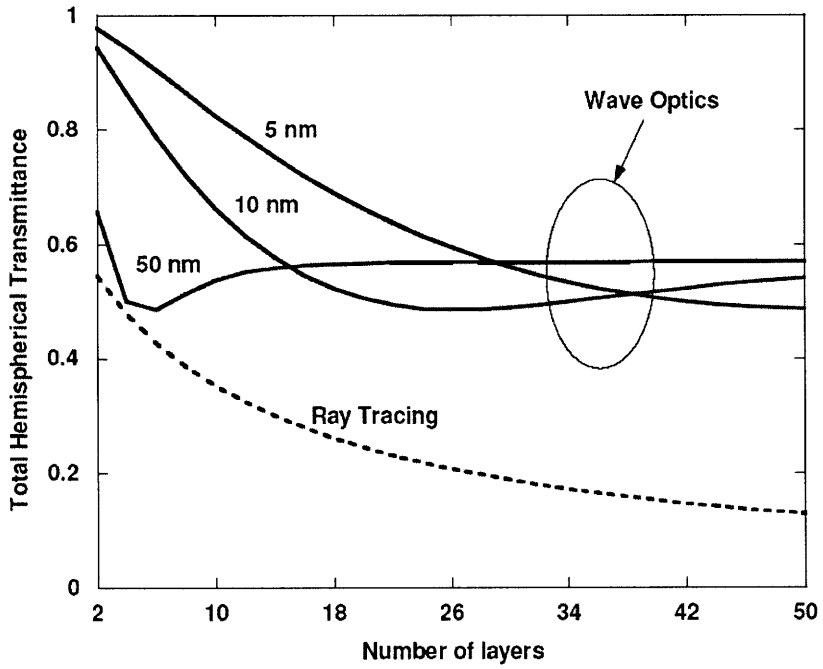

Figure 2-2: The total hemispherical transmittance of three periodic structures as a function of the number of total layers. The individual layer thicknesses of the structures are 5 nm, 10 nm and 50 nm, respectively, which are much less than the coherence length. The thickness dependence of the transmittance is due to interference effects.

Detailed analysis for the thickness dependence of transmittance is shown in Fig. 2-3 for structures with few numbers of layers. It reveals that for thick layers, the ray tracing approach is a good approximation for up to three layers, a result also shown in previous research [6, 7, 57, 58]. For a large number of layers, however, even when the layer thickness exceeds the coherence length, wave optics still does not give the same predictions as the ray tracing method, as shown in Fig. 2-4. The transmittances calculated using the wave optics method for different thicknesses overlap and approach a nonzero value, while those calculated using the ray tracing method asymptotically approaches zero. This implies that interference effects still need to be considered in periodic structures even if every single layer is thicker than the blackbody coherence length. The

ray tracing method fails to accurately predict the transmittance because it neglects phase information. It is interesting to notice that varying the nominal layer thickness does not affect the simulation results at a given temperature; the number of layers is the only determinant variable when the layer thickness exceeds the coherence length of the blackbody radiation.

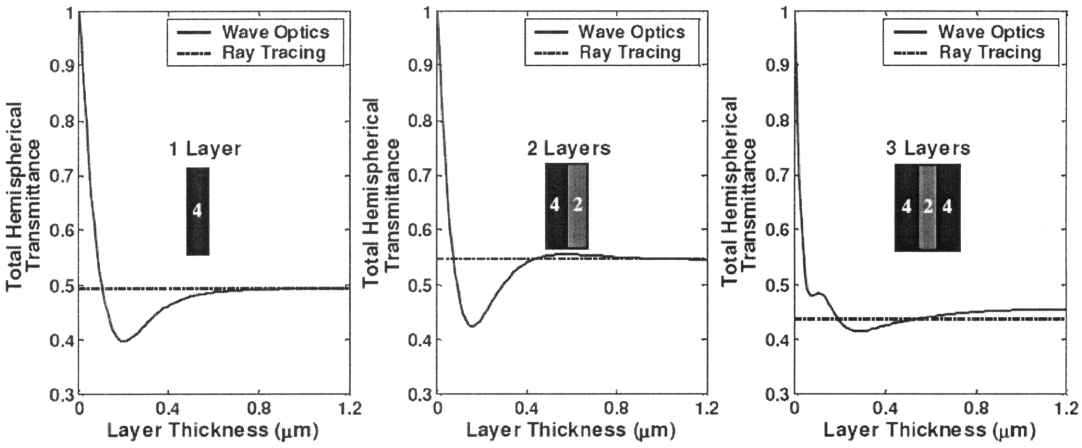

Figure 2-3: The thickness dependence of the total hemispherical transmittance for up to three layers. The refractive index of each layer is given in the illustration. In the thick film region, the transmittance values of all three structures approach constants, which are close to the values predicted by ray tracing method.

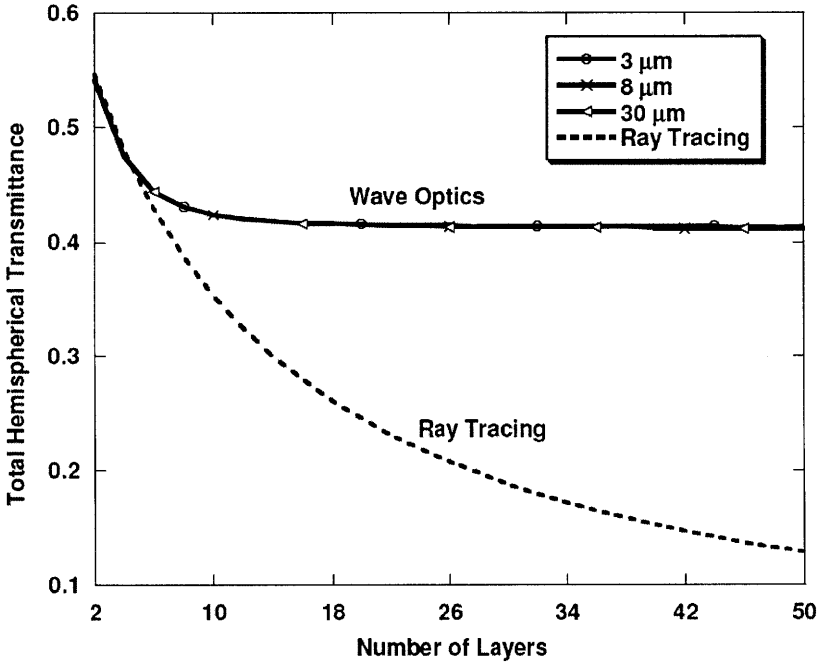

Figure 2-4: The total hemispherical transmittance of three periodic structures as a function of the number of total layers. The individual layer thicknesses of the structures are 3 μm, 8 μm and 30 μm, respectively, which are larger than the coherence length. The transmittances calculated using the wave optics method for different thicknesses overlap and approach a nonzero value, while that calculated using the ray tracing method asymptotically approaches zero.

A frequency analysis can provide more insight into the problem. Figure 2-5(a) shows the frequency dependence of the directional transmittance at normal incidence and Fig. 2-5(b) the unpolarized spectral hemispherical transmittance for a 100-layer periodic structure. The thickness of the individual layers is 8 μm, larger than the coherence length. Figure 2-5(a) clearly shows the stop band behavior. In the transmission bands, the transmittance approaches one, indicating that the waves are extended throughout the whole structure. In the stop band, the transmittance is zero due to the destructive interference effect. This is analogous to the band structure of electrons and phonons in periodic structures, which can also be obtained by applying Bloch periodic boundary conditions to Maxwell's equations [71]. Figure 2-5(b) is simply an average of the band structure along different directions. This shows that waves in periodic structures are

either extended through the whole structure (in the pass bands), or are completely destroyed due to destructive interference (in the stop bands). The average of the extended waves leads to the finite transmittance in Fig. 2-4. The fact that the transmittance does not change above 10-20 layers suggests that these are the numbers of layers needed to form the nearly complete destructive and constructive interference required for the formation of the stop and pass bands. As the layer thickness increases, the pass bands and stop bands become narrower but more bands form. The average of the spectral transmittance gives the same results, which are the thickness- and layer-independent transmittances shown in Fig. 2-4.

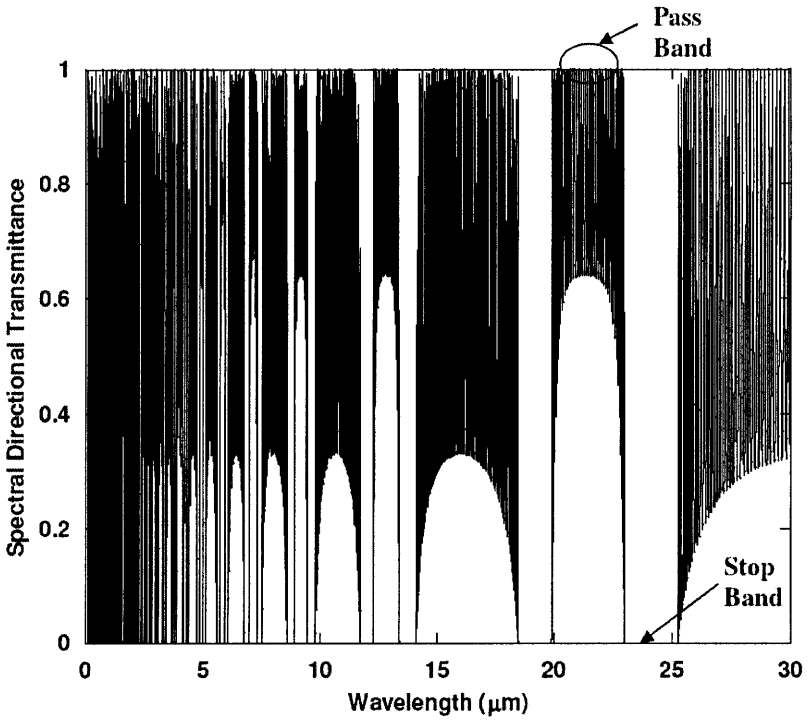

(a)

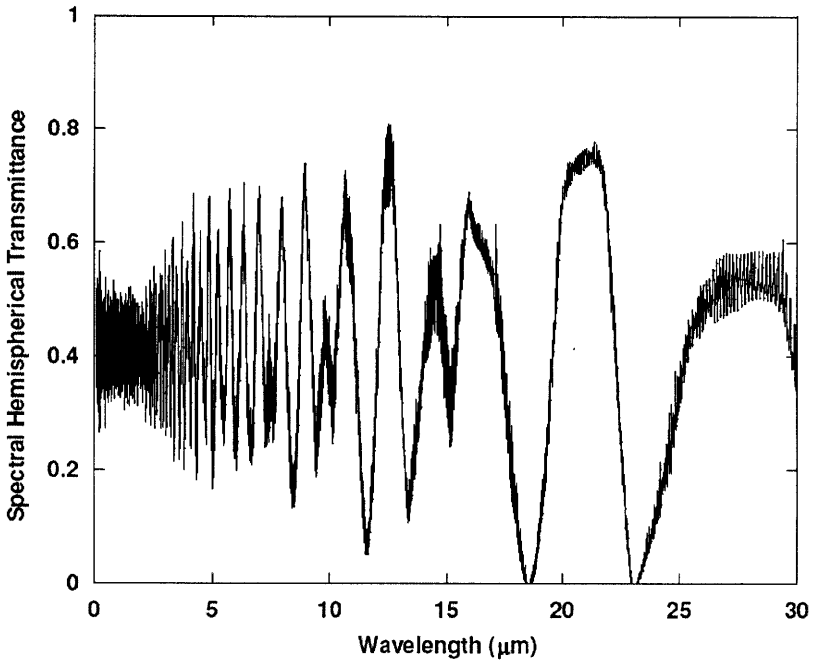

(b)

Figure 2-5: (a) The spectral directional transmittance of a 100-layer periodic structure for normal incident waves. The thickness of individual layers is 8 μm. Stop band and pass band are shown in the figure, (b) The spectral hemispherical transmittance for the same structure.

In comparison, the ray tracing method leads to a transmittance which continuously decays as the number of layers increases. Figure 2-4 shows that for ray tracing, the transmittance decreases inversely with the number of layers. This is because under the ray tracing picture, each layer adds an additional reflection to the radiation transmitted through previous layers.

Although the above results indicate that the coherence length is not a proper criterion for justifying the ray tracing method for multilayer structures, the fact that the transmittance is independent of the individual layer thickness as the layers become thicker than the coherence length still suggests its usefulness. If the layer thickness is smaller than the coherence length, the average values of radiative properties over the

spectrum width of the incoming radiation depend on the layer thickness, as is seen from Fig. 2-3. In the other limit, the average properties are independent of the individual layer thickness, as is clear from Fig. 2-4. However, due to the persistence of the wave effects, i.e., the formation of pass and stop bands for periodic structures, the characteristics of the electromagnetic waves in the structure are very different from those required by the ray tracing method, and the two methods never agree with each other. The existence of wave effects in large systems is not surprising in solids. Extended electron waves in crystals lead to different materials: metals, insulators, and semiconductors.

2.3.2 Structures with randomness

The above discussions are focused on perfectly periodic structures. Real physical structures may have thickness variation, interface roughness, and non-parallel interfaces. The question is then whether these disorders can lead to the agreement between the wave and the ray tracing results. As a first step to investigate the effects of disorder, the variation of individual layer thickness is considered as the only form of disorder in the present structures. The variation is introduced by adding a random distribution onto the layer thickness:

$$d_j = \overline{d} + \delta \cdot \sigma \tag{14}$$

where d_j is the thickness of the j-th layer, $\overline{d}$ is the base thickness of the layers, δ represents a uniform distribution on [0, 1], and σ is the order of randomness which is in length units.

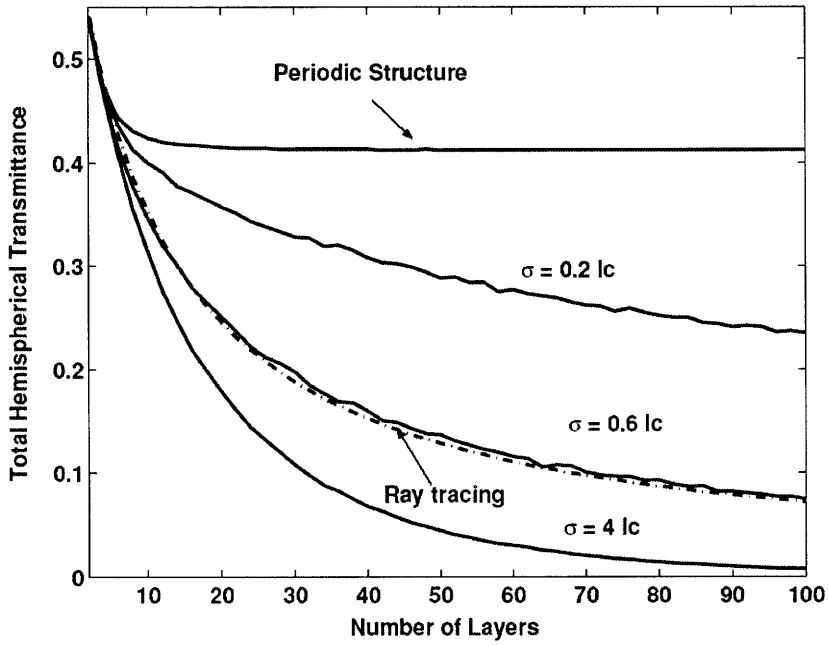
Periodic Structure
σ = 0.2 lc
σ = 0.6 lc
Ray tracing
σ = 4 lc
Total Hemispherical Transmittance
Number of Layers
0
0.1
0.2
0.3
0.4
0.5
10
20
30
40
50
60
70
80
90
100

(a)

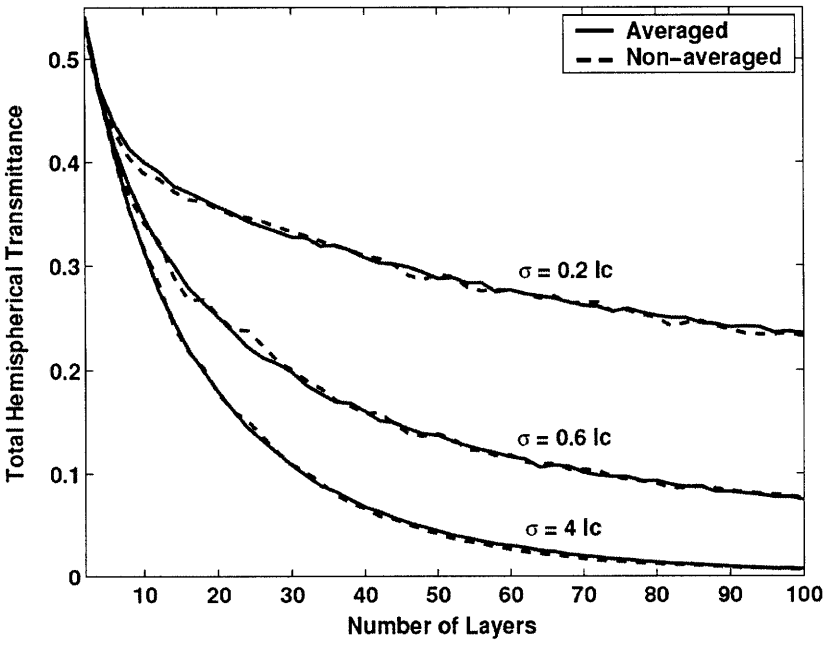
Averaged
Non-averaged
σ = 0.2 lc
σ = 0.6 lc
σ = 4 lc
Total Hemispherical Transmittance
Number of Layers
0
0.1
0.2
0.3
0.4
0.5
10
20
30
40
50
60
70
80
90
100

(b)

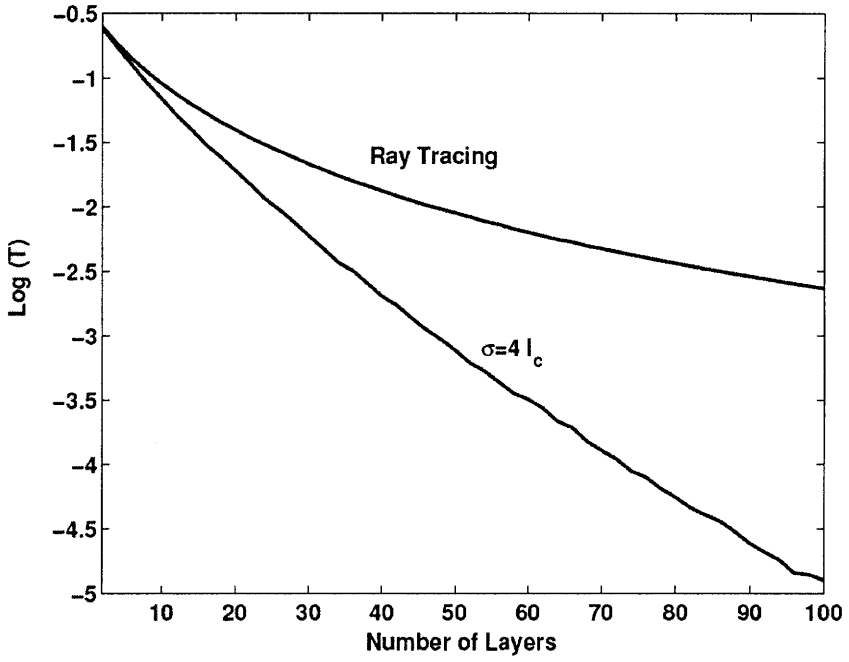

(c)

Figure 2-6: The total hemispherical transmittance as a function of the number of layers, where σ is the order of randomness and l_c is the localization length. The base thickness of individual layers is larger than the coherence length. (b) The averaged and non-averaged transmittance. (c) The y axis is ln(T). In the presence of high order of randomness ($\sigma = 4\ l_c$) and large number of layers, the transmittance decays exponentially.

Figure 2-6(a) shows the dependence of the transmittance on the randomness for structures with individual layer thickness larger than l_c, where l_c is the coherence length. We did calculations based on three different base thickness, 5μm, 8μm and 10μm, respectively. It was found that the transmittance does not depend on the base thickness if the thickness is larger than the coherence length. Also shown in Fig. 2-6(a) is the result obtained using ray tracing method. The transmittances are the ensemble average values over large sets of random numbers. Figure 2-6(b) shows both the non-averaged results and the ensemble average results. Every point in the ensemble average curves represents the result of averaging over 100 configurations. As shown in the figure, the ensemble averaging smoothes the transmittance curve. In general, the fluctuations are not significant even

without averaging, especially in the presence of higher randomness where the localization effects dominate. For all the cases shown in the figure, the thickness of every layer is larger than the blackbody coherence length at 1000K. For small numbers of layers, the transmittance is nearly independent of the randomness and overlap with ray tracing results. However, for structures with more layers, the two methods do not lead to the same results for either periodic or random structures. According to the figure, larger randomness leads to more rapid decay. The transmittance exhibits exponential decay in the regime of higher randomness and large number of layers, which is more rapid than the inverse N (number of layers) decay predicted by the ray tracing method. Figure 2-6(c) is plotted in semi-log scale to show the exponential decay. In the presence of slight or moderate randomness, the transmittance decays at slower rate. It is interesting to notice in the figure that with certain randomness ($\sigma = 0.6l_c$) the wave optics result follows similar decay trend as the ray tracing result. We believe that this is just a coincidence and the two results will eventually diverge as the number of layers increases. More information can be provided through frequency analysis because the decay of intensity is an integral effect of all wavelengths in the blackbody spectrum.

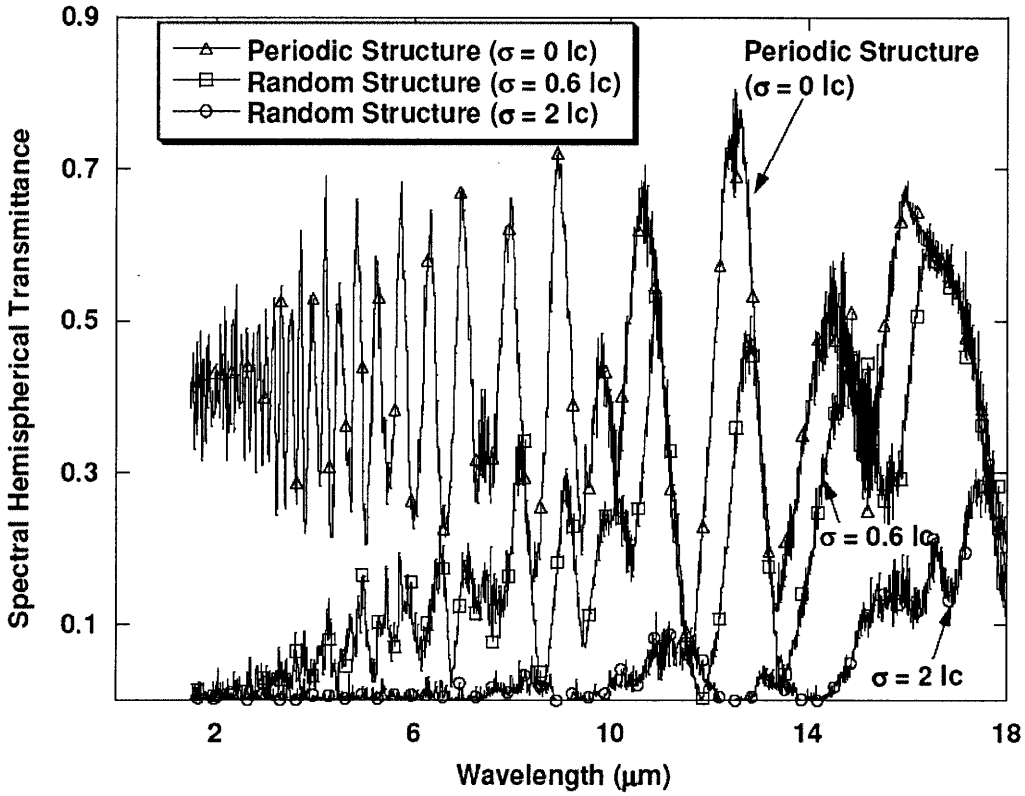

Figure 2-7: The spectral hemispherical transmittances of different random systems, where σ is the order of randomness and l_c is the localization length. High frequency (short wavelength) components are localized relatively more easily.

Figure 2-7 presents the wavelength dependence of transmittance for a 100-layer random structure, of which the base thickness is 8 μm. The figure clearly shows that the transmittance in the 0.5 μm-10 μm range falls virtually to zero, i.e. waves are localized, when the magnitude of randomness is on the order of the coherence length. The localization of EM waves is frequency dependent as shown in Fig. 2-7. The simulation results demonstrate that higher frequency waves are more prone to be localized, which agrees with the previous findings [69]. In contrast, long wavelength components are more difficult to be localized because they are not capable of resolving small amounts of randomness. Consequently, the low randomness cases shown in Fig. 2-7 tend to overlap with the periodic case in the long wavelength regime. With slight or moderate

randomness, a non-negligible fraction of energy is not localized such that the overall transmittance decays at a slower rate than exponential. As a very special case, with moderate randomness ($\sigma = 0.6\ l_c$), the ray tracing method could give similar results as the wave optics as shown in Fig. 2-6(a). As the randomness increases, the lower frequency components are localized. When the randomness is larger than the coherence length, most energy is localized and the average transmittance follows exponential decay.

It should be pointed out that zero transmittance in the stop band is not caused by absorption because the materials are non-absorbing. The exponential decay shown in the figures is caused by the localization of the EM waves in the disordered multilayer structures, which does not incur any energy dissipation in the media. The localization is due to the destructive interference of EM wave packets, which leads to the eventual vanishing of the waves inside the medium and total reflection of the incident waves. The concept of localization differs from the conventional image that the wave propagation in random structures is a series of independent scattering events where the phase is destroyed everywhere in the medium [81]. More detailed analysis regarding field distributions in disordered systems can be found in [82, 83].

2.4 Conclusion

The total hemispherical transmittance of multilayer structures for blackbody incident radiation is numerically studied in both periodic and random one-dimensional systems, using both the wave method and the ray tracing method. It is found that the two methods usually lead to different results even when the individual layer thickness is much larger than the coherence length of the blackbody radiation source. This result, although surprising from the coherence length point of view, can be well explained by localization theory. This study suggests that for multilayer structures with large number of layers, for most cases ray tracing is invalid and wave effects need to be taken into account. It should

be pointed out that the present work does not consider disorder introduced by surface roughness, internal scattering, or non-parallel interfaces, which are essentially three-dimensional systems. Some modes may not be localized in such three-dimensional disordered systems where the diffusion process may dominate instead of localization.

Chapter 3

Near-Field Thermal Radiation between Two Closely Spaced Glass Plates

3.1 Introduction

At a finite temperature, electrons and ions in any matter are under constant thermal agitation, acting as the random current source for thermal emission. The thermally-excited electromagnetic waves have two forms: the propagating modes that can leave the surface of the emitter and radiate freely into the space, and the non-propagating modes (evanescent modes) that do not radiate [20, 84]. The contribution from the propagating modes, or the far-field radiation modes, to the radiative heat flux is well-known and its maximum is governed by Planck's law of blackbody radiation [9]. The non-propagating modes do not propagate and thus do not carry energy in the direction normal to the surface, unless a second surface is brought close to the first to enable photon tunneling, which leads to enhanced radiative heat transfer between the two surfaces.

Theoretical study of the radiative flux between closely-spaced parallel surfaces has been carried out by various researchers [17, 18, 20-22, 84, 85]. Most of theoretical studies are based on the fluctuating electrodynamics approach pioneered by Rytov [17] and Polder and van Hove [18]. These theoretical studies show that, when the distance between two parallel surfaces is small compared to the dominant thermal radiation wavelength, the near radiative heat flux can exceed the far-field upper-limit imposed by

the Planck law of blackbody radiation. Experiments have followed to measure the near field radiative heat flux. Domoto *et al* measured radiative heat transfer between two metallic surfaces at cryogenic temperatures, reporting a value only 1/29 of the upper-limit for gaps between 50 μm and 1 mm [26]. Hargreaves extended the measurements to gaps as small as 1 μm between two chromium surfaces, which gave a radiative heat transfer rate at 50% of the blackbody upper limit [27]. Xu *et al* conducted measurement of radiation heat transfer between two metallic surfaces for reduced gap sizes between 50 nm and 200 nm, but the explanation of their experimental data is hindered by the sensitivity of the experimental technique [28]. More recently, Kittel *et al.* measured near-field radiative transfer between a scanning thermal microscope tip and a flat substrate [29]. The complex geometry of the tip complicates data interpretation.

All previous experiments were done with conducting surfaces, which made gap control possible based on measuring the electrical capacitance or tunneling current. At room temperature (300 K), the peak wavelength for thermal radiation is approximately 10 μm (Wien's displacement law) [2]. Around this wavelength, most metals are highly reflectivity and are not good candidates for the purpose of exceeding the Planck blackbody radiation law [25]. Extremely small gaps are required to obtain high radiative transfer involving metallic surfaces. In this chapter, we report measurements on near-field radiation heat transfer between two glass surfaces, which supports surface phonon polaritons in the infrared region of the electromagnetic spectrum [20]. The resonant wavelength of surface phonon polaritions in glass is well-aligned with the peak wavelength of thermal radiation in the temperature range of interest, leading to higher radiative heat transfer even with moderate gap sizes. Our experimental data demonstrate breakdown of Planck's blackbody radiation law in the near field. Another experiment conducted in the nanoengineering group at MIT by Narayanaswamy explores the same surface-phonon polariton effects by studying the near-field radiative heat transfer between a glass sphere and a glass plate [86]. Narayanaswamy's experiment

demonstrates enhancement of radiative heat transfer by narrowing the gap between the sphere and the plate.

3.2 Direct calculation of the radiative heat flux

To guide the experimental design, we analyze the near-field radiative heat transfer between the two parallel flat glass surfaces using the Green's dyadic [19] and the fluctuation-dissipation theorem [17]. A solution is derived for the radiative transfer between two multilayer systems, which is later simplified to calculate radiative heat flux between the two plates.

3.2.1 Green's function and fluctuation-dissipation theorem

To model the thermal radiative energy transfer between the gap, we apply the vector Helmholtz equation for the electric field in the frequency domain [87]:

$$\nabla \times \nabla \times \vec{E} - k^2 \vec{E} = i\omega\mu \vec{J} \tag{1}$$

where $\vec{E}$ is the electric field vector, $\vec{J}$ is the thermally agitated electric random current. The magnitude of the wave vector is given by $k^2 = \omega^2 \mu\varepsilon$, where ω is the angular frequency, and μ and ε are the magnetic permeability and electric permittivity, respectively. The solution to Eq. (1) can be obtained by the Green function method:

$$\vec{E}(\vec{r}) = i\omega\mu \int_V \overline{\overline{G}}_e(\vec{r},\vec{r}') \cdot \vec{J}(\vec{r}')\, dr'^3 \tag{2}$$

$$\vec{H}(\vec{r}) = \int_V \nabla \times \overline{\overline{G}}_e(\vec{r},\vec{r}') \cdot \vec{J}(\vec{r}')\, dr'^3 \tag{3}$$

where $\overline{\overline{G}}_e$ is the dyadic Green's function of the electric field which is a second order tensor, $\vec{r} = x\hat{x} + y\hat{y} + z\hat{z}$ is the location where the field is evaluated, $\vec{r}' = x'\hat{x} + y'\hat{y} + z'\hat{z}$ is the location in the source region. The magnetic field vector $\vec{H}$ is obtained by substituting Eq. (2) into Faraday's equation. The integration is performed in volume V where the thermal current exists.

The dyadic Green's function for Maxwell's equations is a very useful tool for solving a wide range of problems in electromagnetism. The solution to Maxwell's equations translates to the solution to the dyadic Green's functions with specific geometry. For one-dimensional multilayer structures, the Green's function for the electric field has an analytical solution in the source free region [19] :

$$\overline{\overline{G}}_e^{\sigma}(\vec{r},\vec{r}') = \frac{i}{8\pi^2}\iint \frac{dk_x dk_y}{k_{sz}} \cdot \left\{ \begin{array}{l} \left[A_l^{\sigma}\hat{e}_l^{\sigma}(k_{lz}) e^{i\vec{k}_l^{+}\cdot\vec{r}} + B_l^{\sigma}\hat{e}_l^{\sigma}(-k_{lz}) e^{i\vec{k}_l^{-}\cdot\vec{r}} \right] \hat{e}_s^{\sigma}(-k_{sz}) e^{-i\vec{k}_s^{-}\cdot\vec{r}'} + \\ \left[C_l^{\sigma}\hat{e}_l^{\sigma}(k_{lz}) e^{i\vec{k}_l^{+}\cdot\vec{r}} + D_l^{\sigma}\hat{e}_l^{\sigma}(-k_{lz}) e^{i\vec{k}_l^{-}\cdot\vec{r}} \right] \hat{e}_s^{\sigma}(k_{sz}) e^{-i\vec{k}_s^{-}\cdot\vec{r}'} \end{array} \right\} \quad (4)$$

where the superscript σ represents the polarization (either transverse electric polarized – s polarization, or transverse magnetic polarized – p polarization), and the subscripts l and s denote the l^{th} layer and the source layer (a layer that has an optical constant with a nonzero imaginary part), respectively. The wave vector $\vec{k}^{\pm}$ is given by $\vec{k}^{\pm} = \hat{x}k_x + \hat{y}k_y \pm \hat{z}k_z$. The surface normal $\hat{z}$ and unit vectors $\hat{e}^s$ and $\hat{e}^p$ form an orthogonal system: $\hat{e}^s(\pm k_z) = \dfrac{\vec{k}^{\pm}\times\hat{z}}{\left|\vec{k}^{\pm}\times\hat{z}\right|}$ and $\hat{e}^p(\pm k_z) = \dfrac{\hat{e}^s(\pm k_z)\times\vec{k}^{\pm}}{k}$. A schematic of the multilayer structure is given in Fig. 3-1. The Green's function for the magnetic field is given by

$$\overline{\overline{G}}_h^{\sigma}(\vec{r},\vec{r}') = \nabla\times\overline{\overline{G}}_e^{\sigma}(\vec{r},\vec{r}') \quad (5)$$

where the subscript *h* indicates the magnetic field.

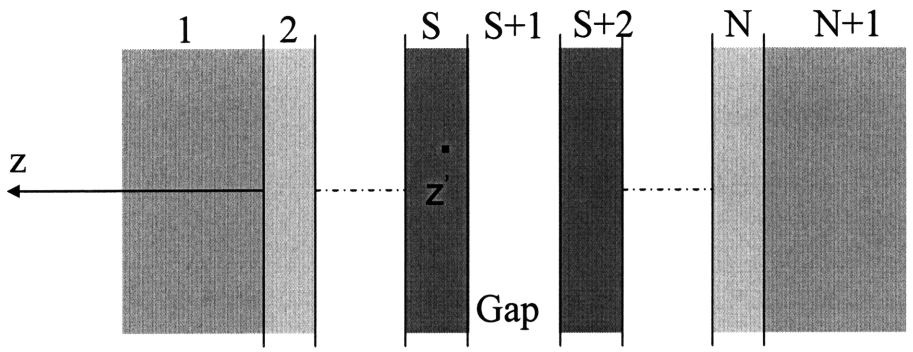

Figure 3-1: A schematic of two multilayer structures. The source layers are S and S+2. A vacuum gap exists between S and S+1. Layers 1 and N+1 are semi-infinite. The interface between layer *l* and *l*+1 is numbered as interface *l*.

Two sources layers, S and S+2 are present in the structure. All the rest of the layers consist of lossless materials. A vacuum gap S+1 exists between the two source layers. Layers 1 and N+1 are both semi-infinite.

In the source region, the Green's dyadic function of the electric field has additional terms:

$$\overline{\overline{G}}_e^{\sigma}(\vec{r},\vec{r}') = \frac{i}{8\pi^2}\iint \frac{dk_x dk_y}{k_{sz}} \cdot \begin{cases} \left\{ \left[A_l^{\sigma}\hat{e}_l^{\sigma}(k_{lz}) e^{i\vec{k}_l^{+}\cdot\vec{r}} + \left(B_l^{\sigma}+1\right)\hat{e}_l^{\sigma}(-k_{lz}) e^{i\vec{k}_l^{-}\cdot\vec{r}} \right] \hat{e}_s^{\sigma}(-k_{sz}) e^{-i\vec{k}_s^{-}\cdot\vec{r}'} + \right. \\ \left. \left[C_l^{\sigma}\hat{e}_l^{\sigma}(k_{lz}) e^{i\vec{k}_l^{+}\cdot\vec{r}} + D_l^{\sigma}\hat{e}_l^{\sigma}(-k_{lz}) e^{i\vec{k}_l^{-}\cdot\vec{r}} \right] \hat{e}_s^{\sigma}(k_{sz}) e^{-i\vec{k}_s^{-}\cdot\vec{r}'} \right\} & (z < z') \\ \left\{ \left[A_l^{\sigma}\hat{e}_l^{\sigma}(k_{lz}) e^{i\vec{k}_l^{+}\cdot\vec{r}} + B_l^{\sigma}\hat{e}_l^{\sigma}(-k_{lz}) e^{i\vec{k}_l^{-}\cdot\vec{r}} \right] \hat{e}_s^{\sigma}(-k_{sz}) e^{-i\vec{k}_s^{-}\cdot\vec{r}'} + \right. \\ \left. \left[\left(C_l^{\sigma}+1\right)\hat{e}_l^{\sigma}(k_{lz}) e^{i\vec{k}_l^{+}\cdot\vec{r}} + D_l^{\sigma}\hat{e}_l^{\sigma}(-k_{lz}) e^{i\vec{k}_l^{-}\cdot\vec{r}} \right] \hat{e}_s^{\sigma}(k_{sz}) e^{-i\vec{k}_s^{-}\cdot\vec{r}'} \right\} & (z > z') \end{cases} \tag{6}$$

The coefficients of *A, B, C* and *D* can be determined by matching the boundary conditions at layer interfaces:

$$\hat{z}\times\overline{\overline{G}}^{\sigma}_{e,l}\Big|_{z=0} = \hat{z}\times\overline{\overline{G}}^{\sigma}_{e,l+1}\Big|_{z=d_l} \tag{7}$$

$$\hat{z}\times\nabla\times\overline{\overline{G}}^{\sigma}_{e,l}\Big|_{z=0} = \hat{z}\times\nabla\times\overline{\overline{G}}^{\sigma}_{e,l+1}\Big|_{z=d_l} \tag{8}$$

where d_l is the thickness of layer l. Repeat the matching of boundary conditions for all the interface and the coefficients can be determined using the transfer matrix method introduced in Chapter 2 [56].

The net thermal radiative flux from layer S is given by the Poynting vector, ensemble averaged over the random fluctuation thermal source:

$$\vec{P}(\vec{r},T) = \frac{1}{2}\mathrm{Re}\left\langle \vec{E}\times\vec{H}^{*}\right\rangle = \frac{1}{2}\mathrm{Re}\left\{ i\omega\mu\sum_{\sigma=s,p}\int_V dr_1'^{3}\int_V dr_2'^{3} \left\langle\left[\overline{\overline{G}}^{\sigma}_{e}\left(\vec{r},\vec{r}_1'\right)\cdot\vec{J}\left(\vec{r}_1'\right)\right]\times\left[\nabla\times\overline{\overline{G}}^{\sigma}_{e}\left(\vec{r},\vec{r}_2'\right)\cdot\vec{J}\left(\vec{r}_2'\right)\right]^{*}\right\rangle\right\} \tag{9}$$

The ensemble average of the random thermal current is determined by the fluctuation-dissipation theorem [17]:

$$\left\langle J_l\left(\vec{r}_1'\right)J_m^{*}\left(\vec{r}_2'\right)\right\rangle = \frac{4\omega}{\pi}\varepsilon_o\varepsilon_s''\Theta(\omega,T)\delta\left(\vec{r}_1'-\vec{r}_2'\right)\delta_{lm} \tag{10}$$

where the subscripts l and m denote the coordinates (x, y or z), ε_o is the vacuum permittivity, ε_s'' is the imaginary part of the dielectric function of the source layer, $\delta\left(\vec{r}_1'-\vec{r}_2'\right)$ is the Dirac delta function, and δ_{lm} is the Kronecker delta. The average energy of the harmonic oscillator at temperature T is given by,

$$\Theta(\omega,T)=\frac{\hbar\omega}{\exp(\hbar\omega/k_bT)-1} \tag{11}$$

where $\hbar$ and k_b are Planck's constant divided by 2π and Boltzmann's constant, respectively. The two source regions are at different temperatures, which results in a nonzero radiative heat flux across the vacuum gap. Since the random currents in the two source layers are uncorrelated, the net radiative heat flux between layer S and S+1 is a simple linear relation:

$$q''=\left[\vec{P}_s(\vec{r},T_s)-\vec{P}_{s+1}(\vec{r},T_{s+1})\right]\cdot\hat{z} \tag{12}$$

3.2.2 Optical constant of amorphous SiO_2: Lorentz model

To calculate the radiative heat flux across the two glass plates, the frequency-dependent optical constant of glass (fused quartz) is taken from ref. [88]. The Lorentz model [54] is used to interpolate the data points between 26.67 μm and 100 μm because no data are available in this range. The Lorentz model of the dielectric function is given by

$$\varepsilon=\varepsilon_\infty+\sum_m\frac{\omega_{p,m}^2}{\omega_{0,m}^2-\omega^2-j\omega\gamma_m} \tag{13}$$

where ε_∞ is the dielectric function at high frequency, ω_p is the plasma frequency, ω_0 is the resonant frequency of the harmonic oscillator, γ is the damping factor, and j is the imaginary unit. A nonlinear least square algorithm is used to find the parameters that fit the available data.

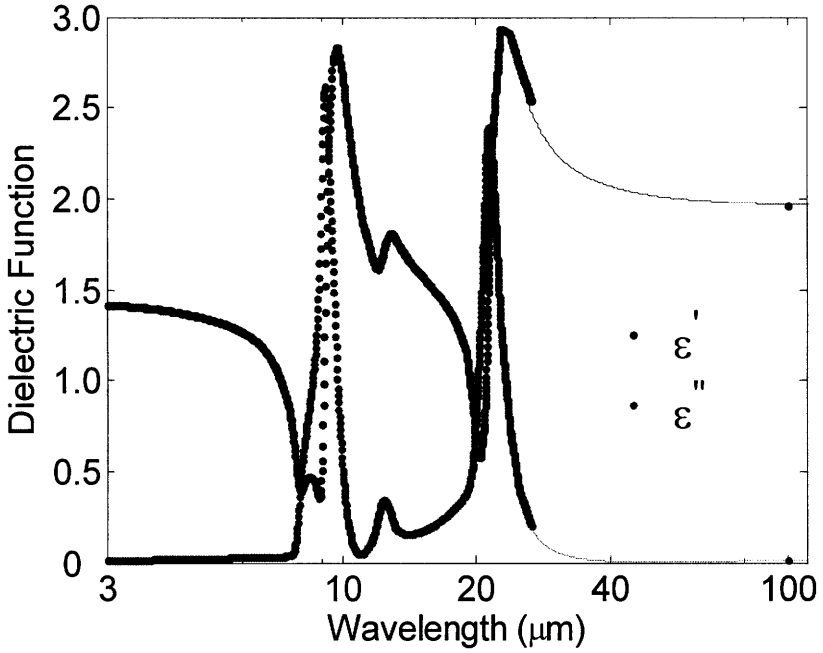

Figure 3-2: The dielectric function of amorphous SiO_2. ε' is the real part and ε'' is the imaginary part. The literature data is plotted in dots. The solid curves are the interpolations between 26.67 μm and 100 μm where no experimental data is available.

3.3.3 Gap-size dependent radiative flux

The radiative heat transfer rate between the two glass plates is a function of the gap size. We define the gap-size dependent heat transfer coefficient as:

$$h_r = q_r'' / (T_h - T_c) \tag{14}$$

where q_r'' is the radiative heat flux calculated using Eq. (12), and T_h and T_c are the temperatures of the hot surface and the cold surface, respectively. The radiative heat transfer coefficient is plotted as a function of the gap size in Fig. 3-3(a) for T_h = 50 °C and T_c = 24 °C. The far-field radiative heat transfer coefficient between two blackbodies is given as a reference in the same figure.

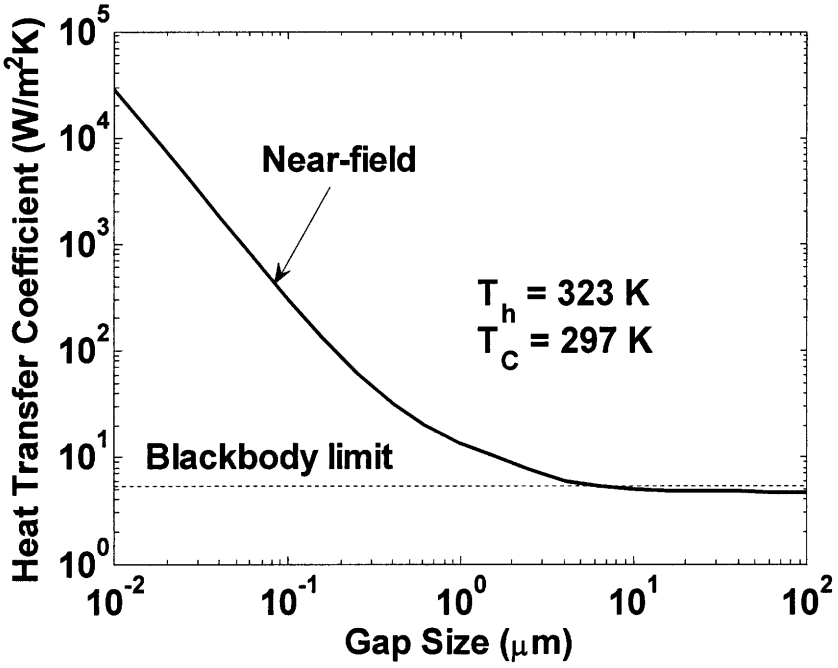

(a)

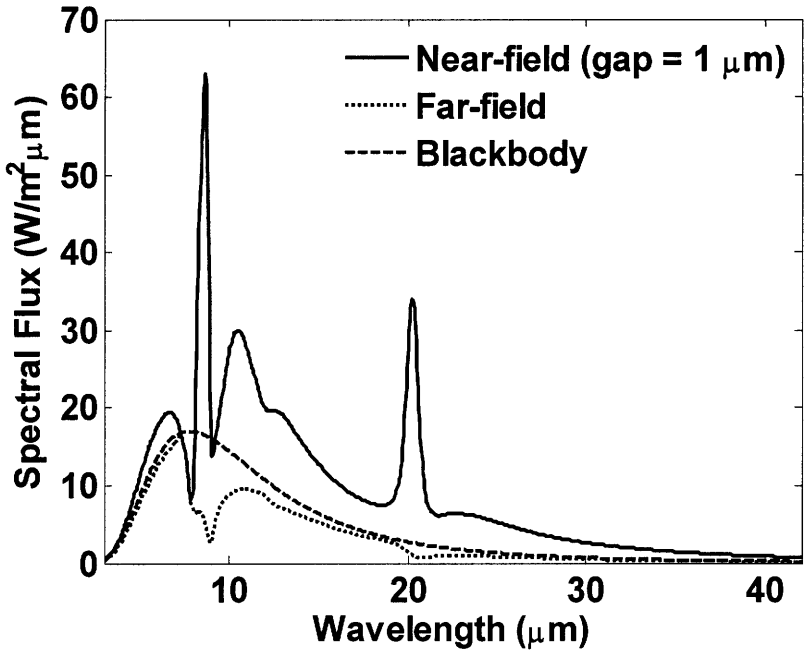

(b)

Figure 3-3: (a) Gap-size dependent heat transfer coefficient. (b) Calculated spectral radiative heat flux between two glass surfaces. The gap is set to be 1 μm. For calculations in both figures, the hot and cold side temperatures are 50 °C and 24 °C, respectively.

As the gap decreases below 5 μm, the heat transfer coefficient starts to exceed the blackbody limit. Note the coefficient is plotted in log scale. As the gap shrinks even more, the coefficient continues to increase, owing to enhanced tunneling of the surface waves. Around 1 μm, the coefficient is more than 50% higher than the blackbody limit, which is readily measurable without the need to shrink the gap further. Figure 3-3(b) shows the wavelength dependent radiative heat flux between the two surfaces, assuming the hot side and cold side temperatures to be 50 °C and 24 °C, respectively, and a gap of 1 μm. The figure clearly reveals two dominant peaks at 8.7 μm and 20.2 μm, which are the resonance wavelengths of surface phonon polaritons in glass [20], indicating the radiative heat transfer across a 1 μm gap is primarily due to the contribution from the surface phonon polaritons.

3.3 Measurement of the near-field flux

3.3.1 Experimental setup

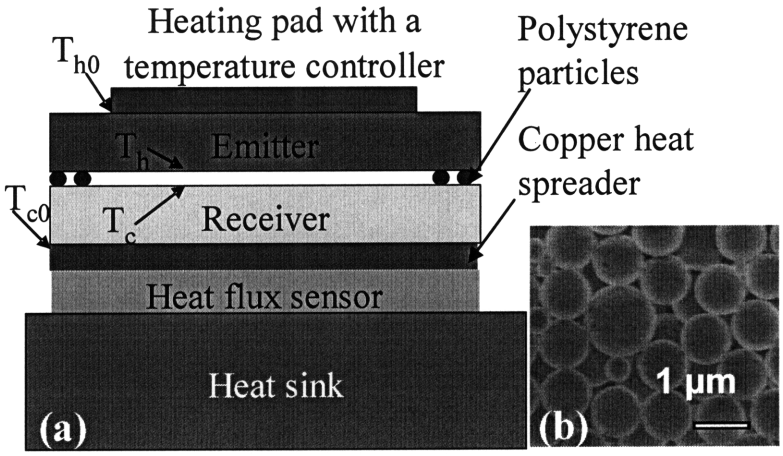

Figure 3-4: (a) A schematic drawing of the experiment setup. (b) Two optical flats and (c) A scanning electron microscope image of polystyrene particles.

Figure 3-4(a) shows the schematic drawing of the experimental setup. Two identical precision glass optical flats (λ/20 accuracy) are used as the emitter (hot side) and the receiver (cold side). The diameter of the glass optical flats is 0.5 inch (1.27 cm) and the thickness is 0.25 inch (0.635 cm). The surfaces of the optical flats have flatness better than 0.05 μm over the entire surface. To maintain a gap between the emitter and the receiver, polystyrene microspheres (Fig. 3-4(b)) are placed between the two surfaces as spacers. Based on the theoretical calculation of the radiative heat flux, we decide to set the gap to be 1 μm and thus choose the nominal diameter of the spheres to be d = 1 μm. Polystyrene is selected because its thermal conductivity is low, with a reported value at 0.18 W/mK [89]. The conduction heat leakage through a polystyrene sphere is estimated as

$$q_c'' = k_{sphere} A \frac{T_h - T_c}{d_{sphere}} = \frac{k_{sphere} \pi d_{sphere}}{4} \left(T_h - T_c\right) \tag{15}$$

where a cross-section area of $\pi d^2_{glass}/4$ is assumed for heat conduction. This is a conservative estimation for the heat conduction since actual heat transfer area can be much smaller due to spherical geometry. We compare heat conduction with that of the blackbody far-field radiative heat transfer:

$$q_r'' = \sigma \frac{\pi d_{glass}^2}{4} \left(T_h^4 - T_c^4\right) \tag{16}$$

The ratio of Eq. (15) to Eq. (16) is

$$\alpha = \frac{q_c''}{q_r''} = \frac{k_{sphere} d_{sphere}}{\sigma d_{glass}^2 \left(T_h^2 + T_c^2\right)\left(T_h + T_c\right)} \tag{17}$$

The hot side temperature is assumed to be 50 °C and the code side temperature is assumed to be 24 °C. Substitute the values into Eq. (17), the heat conducted through a polystyrene sphere is approximately 1/6000 of the far-field radiative heat flux between the emitter and the receiver. Note that in a real measurement situation, the heat conduction leakage is an even smaller fraction of the radiative flux because a contact area of $\pi d^2/4$ between the sphere of diameter d and the glass surface is overestimated. Further more, higher radiative heat flux is also expected in the near-field measurement since with micron sized gap, the heat flux exceeds the blackbody limit. In addition, during the measurement, the hot side temperature varies from 50 °C to 110 °C. All these measurement conditions result in an even smaller conduction to radiation ratio compared to the value predicted by Eq. (17), which ensures good signal to noise ratio.

The spherical particles are diluted in deionized water as liquid suspension. The suspension is not stable because of the size of the particles. Constant stirring is thus needed to avoid precipitation. With the help of a pipette, small droplets of the liquid suspension are dispensed over the surface of the cold side over uniformly spaced locations. A total of around 80 polystyrene particles are deposited between the two optical flats, thus limiting the conduction heat flux to be less than 1.5% of the radiative heat flux according to the previous heat transfer analysis. After the water in the droplets evaporates, the emitter is placed on top of the receiver, with the particles serving as spacers to separate the two objects. We carefully conduct all the operations in a laminar flow workstation to eliminate dust particles in the air. The optical flats have been cleaned with acetone to ensure no other organic remaining left on the surfaces.

As illustrated in Fig. 3-4(a), a heating pad is attached on the top surface of the emitter. The temperature of the heating pad T_{h0} is monitored with a platinum resistance temperature detector (RTD), which feeds the signal to a temperature controller. With the feedback control, the temperature of the heating pad can be set to a value with variations within 1 °C. To accurately measure the steady state radiative heat flux, we need to ensure that the temperature of the optical flats is stabilized. The response time of the optical flat

to the heating is determined by its heat capacitance, an important parameter that determines the time to stabilize the temperature. The heat capacitance of the optical flat is

$$C_h = \rho V c_p \tag{18}$$

where ρ is the density of glass, V is the volume of the optical flat and c_p is the specific heat of glass. The thermal time constant of the optical flat is given by

$$\tau_t = \frac{C_h}{h_r A_s} \tag{19}$$

where h_r is the radiative heat transfer coefficient and A_s is the surface area that radiates heat. For an order of magnitude analysis, we choose $h_r \sim \sigma(T_h^2+T_c^2)(T_h+T_c) = 6.7$ W/mK. Again, the hot side temperature is assumed to be 50 °C and the code side temperature is assumed to be 24 °C. During measurement, this value will be larger due to larger h_r on the bottom surface and larger value of T_h. The side surfaces of the optical flats are wrapped with aluminum foil to minimize radiative heat exchange with the environment. Thus most of the heat radiated from the top and bottom surfaces which have a combined surface area of $\pi d^2_{glass}/2$. The specific heat and density of glass are taken from literature, and the values are 745J/kg·K and 2220kg/m^3, respectively [10]. The time constant calculated using Eq. (19) is 776 s, which suggests that a typical waiting time of 10 to 20 min is required for the heat flux to stabilize. In comparison, the cold side flat plat has a much smaller thermal time constant because it releases heat much faster through conduction into the heat sink, which is less a problem in terms of temperature stabilization.

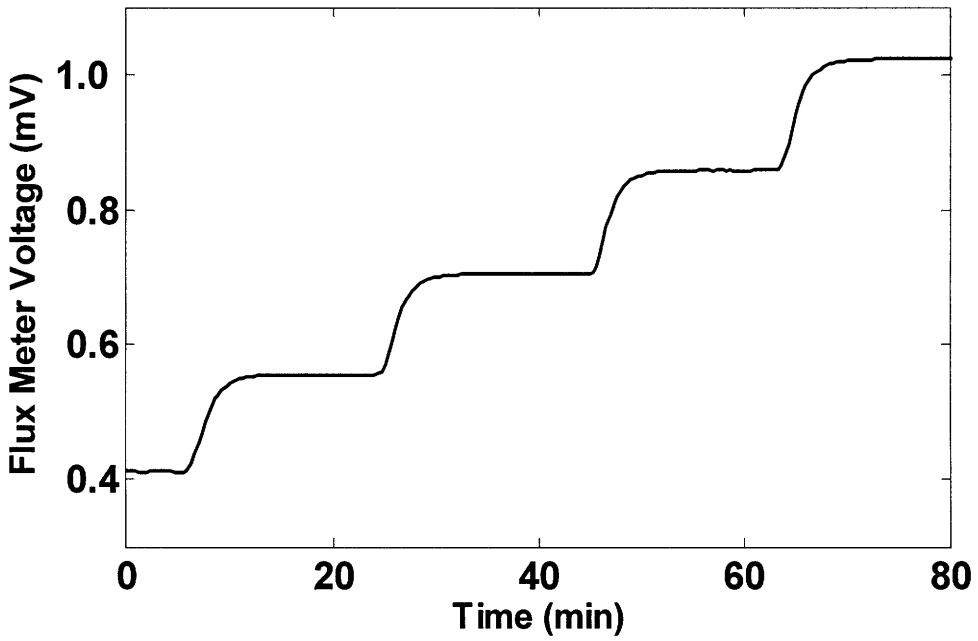

Figure 3-5: The transient flux meter voltage. The emitter temperature is increased 4 times during the measurement. The curve shows the stabilization process with a thermal constant around 7 min.

Figure 3-5 shows the transient flux meter voltage, which is proportional to the radiative heat flux. During the measurement, the emitter temperature is increased 4 times, corresponding to the 4 sudden increase of the heat flux. The heat flux stabilizes over time and the thermal constant is approximately 7 min, close to the estimate given by Eq. (19). To measure the radiative heat flux, a 1 inch by 1 inch heat flux meter is positioned between the receiver and the heat sink. A copper heat spreader (1 inch × 1 inch) is sandwiched between the receiver (0.5 inch in diameter) and the heat flux meter to homogenize temperature over the surface. Thermal grease is applied to the interfaces for good thermal contact. To ensure that the heat flux meter measures only the radiative flux, the heat loss by conduction needs to be minimized by placing the entire testing setup in a vacuum chamber pumped down to 8.5×10^{-3} Pa. The vacuum level limits heat conduction through the rarefied air [90] in the small gap to be less than 0.05% of the radiation.

To test the experimental system, we first measured the far-field radiation. The emitter was clamped to a sample holder for the far-field measurement and the gap between the two surfaces was set to be 2 mm. We next proceeded to the near-field measurement using the particles as the spacers. For both measurements, to obtain the temperature dependent radiative heat flux, we varied the temperature of the heating pad and measured the corresponding heat flux by reading the voltage signal of the flux meter. The temperature of the bottom surface of the receiver T_{c0} was recorded by a K-type thermocouple inserted in between the copper spreader and the flux meter. For each measurement, we made sure that the reading from the heat flux meter stabilized before taking the data, allowing the two optical flats to reach steady state temperatures.

Note that even at the steady state, the temperatures inside the optical flats is not uniform due to a nonzero one-dimensional (1D) heat flux along the cylinder axis direction of the optical flats. From the temperature reading T_{h0} on the heating pad and the heat flux data, we can derive the temperature T_h on the lower surface of the emitter by solving a 1D heat conduction problem. The lower surface temperature is given by $T_h = T_{h0} - q_r'' d_{glass} / k_{glass}$, where q_r'' is the measured flux, and d_{glass} and k_{glass} are the thickness and thermal conductivity of the optical flat. Similarly, the temperature T_c on the upper surface of the receiver is given by $T_c = T_0 + q_r'' d_{glass} / k_{glass}$. The temperatures T_h and T_c are the effective temperatures for thermal emission because the electromagnetic penetration depth in glass is much less than 1 mm and thermal radiation is essentially a surface phenomenon in the wavelengths of interest.

3.3.2 Measurement results

The measured heat flux data is presented in Fig. 3-6, which has been adjusted by taking into account a heat spreading factor of $16/\pi$ between the circular cold side and the square flux meter. The variation of the temperature T_{c0} on the bottom surface of the receiver is

less than 0.5 °C during the experiment and the average value is 23.7 °C. The far-field upper limit of the radiative heat flux is given by $q_b'' = \sigma\left(T_h^4 - T_c^4\right)$ and plotted in the figure as a reference curve, where σ is the Stefan-Boltzmann constant. Note that T_h and T_c are derived based on the 1D heat conduction model described previously. As shown in the figure, as the temperature of the hot surface increases, both the near-field and far-field radiative fluxes increase. While the far-field heat flux stays below the upper limit, the

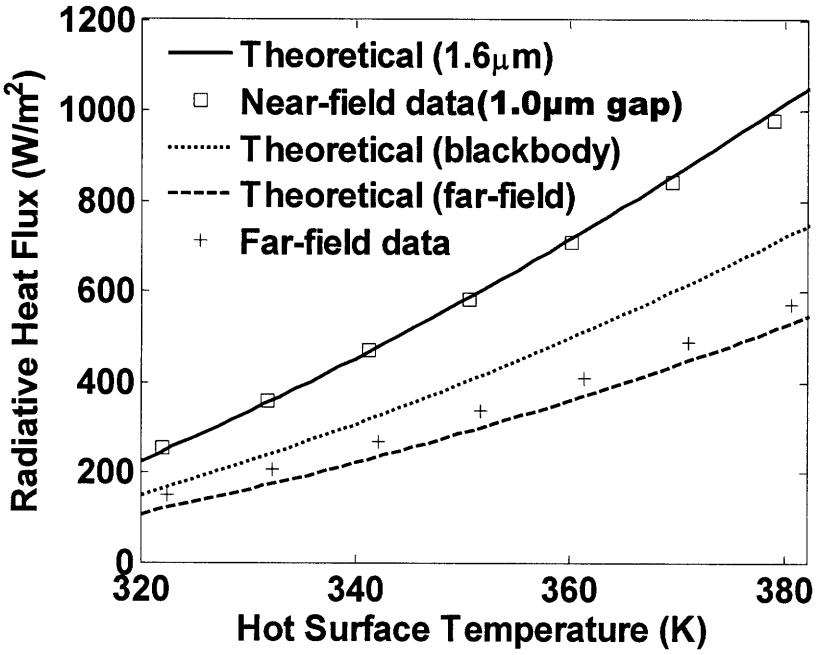

Figure 3-6: Measured radiative heat flux between the two optical flats. The flux between two blackbodies is plotted as a reference and lies between the near-field and far-field curves.

near-field heat flux clearly exceeds the blackbody upper-limit by more than 35% in the entire temperature range. Also shown in Fig. 3-6 is the calculated far-field radiative heat flux. The far-field curve agrees reasonably well with the experimental data, suggesting good measurement accuracy.

Figure 3-7 compares theoretical predictions and experimental data for the temperature dependent heat transfer coefficient in the near-field case. The measured data agrees well with the theoretical prediction for a 1.6 μm gap, instead of the 1 μm gap that

we are supposed to have. One plausible reason for this larger-than-expected gap is likely due to the dispersion in the diameters of the spheres used. The polystyrene particles have a deviation in diameters, as shown in Fig. 3-4(b). The gap is determined by the larger particles. Another possible factor that affects the fitting of experimental data is the accuracy of the optical data we used for the theoretical calculation. We take the optical constant of glass from literature. As we mentioned previously, we had to do interpolation to obtain the optical constants between 26.67 μm and 100 μm. Further more, the optical data were usually measured at room temperature while the measurement is conducted at elevated temperatures. Despite the uncertainty in matching the data with theoretical predictions, the data clearly shows that the radiative heat transfer exceeds the blackbody radiation flux. The heat transfer coefficient increases as the temperature of the hot side rises. An increase of 19% is found for the temperature range. In the same temperature range, the thermal conductivity of polymer typically decreases and that of glass [91] increase at much lower rate, excluding the possibility that the origin of the measured heat flux is conductive in nature.

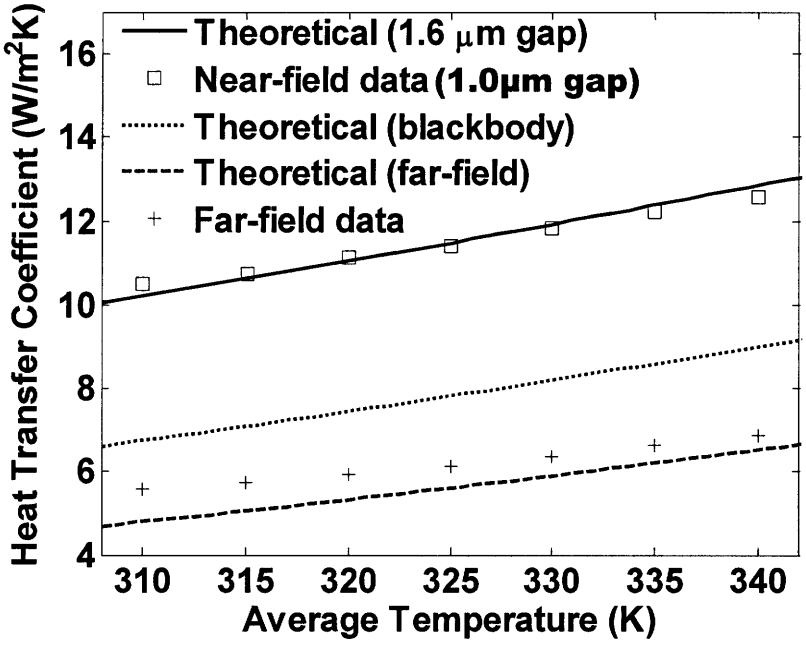

Figure 3-7: Temperature dependent heat transfer coefficient. The temperature is the average of the hot surface and cold surface temperatures.

We also attempted measurement for smaller gaps. Figure 3-8(a) and 3-8(b) show the measured radiative heat flux between the two flat plates separated by 0.2 μm particles. The measured radiative heat flux can be fitted with the calculation results by assuming a gap of 0.65 μm. However, as clearly shown in Fig. 3-8(b), the measured radiative transfer coefficient stays almost constant over the temperature range, as compared to the approximately linear dependence on the temperature given by the theoretical calculation. The constant radiative transfer coefficient is uncharacteristic of near-field radiation. An almost constant heat transfer coefficient is usually an indication of heat conduction. Therefore, the trend of the heat transfer coefficient suggests that the measured flux is dominated by conduction. During the measurement, the smaller 0.2 μm polystyrene particles may cause contact between the two optical flats and lead to conduction heat leakage.

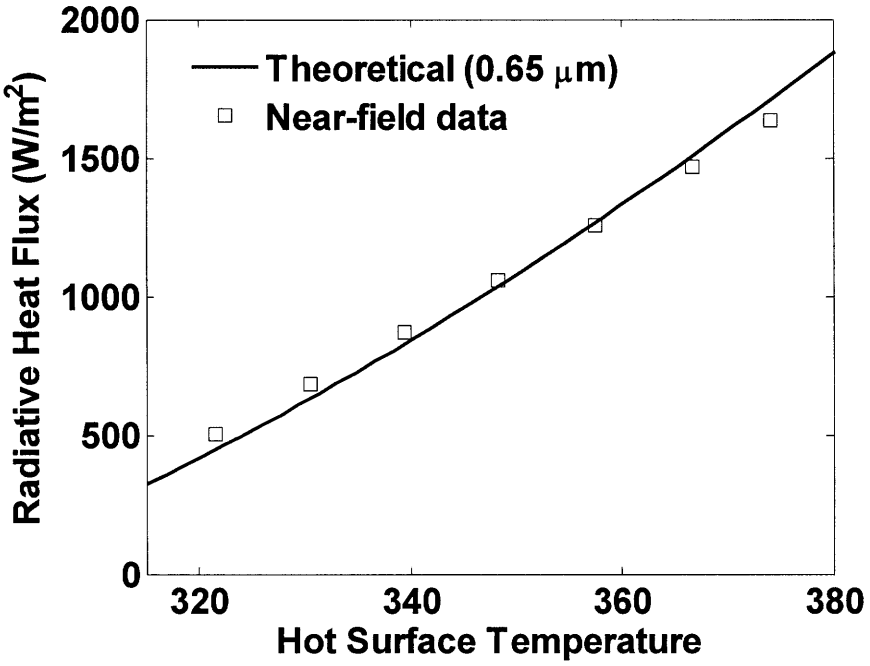

(a)

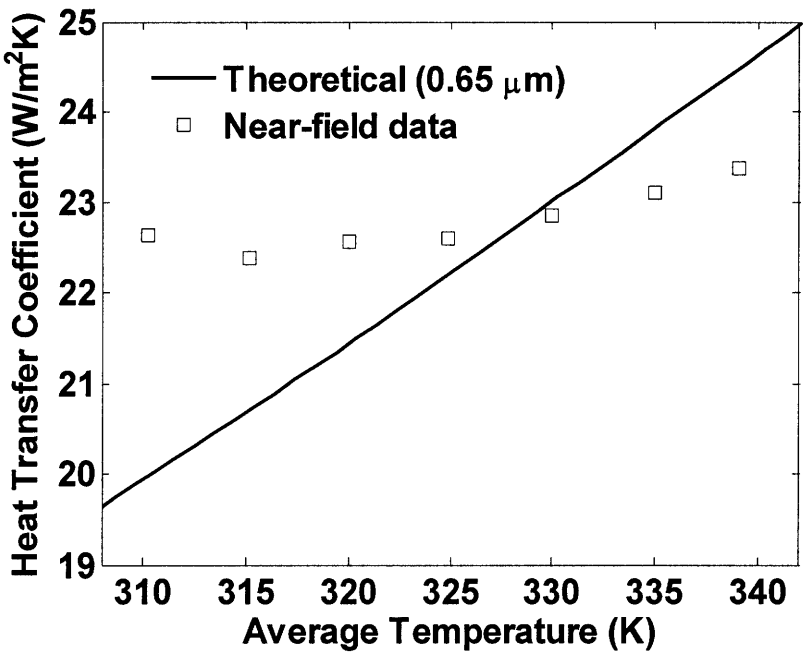

(b)

Figure 3-8: (a) Measured radiative heat flux with a nominal gap size of 0.2 μm. The experimental data agrees with the calculated flux for a gap of 0.65 μm. (b) Temperature dependent heat transfer coefficient. The measured data stays almost constant while the calculation results show a linear dependence.

3.4 Conclusion

In summary, we conducted experimental study on the near-field thermal radiation between two closely spaced glass surfaces. The measured radiative heat flux exceeds the blackbody radiation for more than 35% in the entire temperature range. However, the experimentally measured flux is less than the theoretical prediction. There are a few factors that could lead to the reduced flux. First of all, the optical constant between of glass between 26.67 μm and 100 μm was interpolated from literature data and could be inaccurate. Further more, the optical constants found in literature are usually taken at room temperature while our measured was conducted at elevated temperatures. The most plausible explanation is the possible inclusion of larger particles between the optical flats

which causes the gap to be larger than the nominal diameter of the particles. Nevertheless, our measurement clearly demonstrates that Planck's law is broken in the near-field regime despite the uncertainty in matching the experimental data with the theoretical data.

From theoretical considerations, we attribute the primary contribution to the heat transfer to surface phonon polartions at the interface between glass and vacuum. We also attempted measurement on smaller gaps. However, the measured heat transfer coefficient indicates possible contact between the optical flats.

Chapter 4

Optical Absorption in Nanowire Arrays

4.1 Introduction

Nanowires and nanotubes can serve as electrodes for polymer and electrochemical photovoltaic cells [92, 93], and building blocks in other novel optical devices [94, 95]. Recently photovoltaic cells based on silicon nanowire arrays have been suggested as a promising candidate for solar energy harvesting [96]. Solar cells based on single silicon nanowires haves been fabricated and tested [97, 98]. The advantage of the silicon-nanowire photovoltaic cell lies in its short collection length for excited carriers, resulting in significant improvement in carrier collection efficiency. The optical absorption characteristics of nanowire arrays in the solar spectrum, one of the key factors that determine the efficiency of solar cells, remain unclear. A detailed analysis of the optical absorption will help the design and optimization processes of the silicon nanowire solar cells. In this chapter, we numerically analyze the effects of wire diameter, length and filling ratio on the optical absorption of periodic nanowire arrays, and compare the cases with the results of silicon thin films. We found that, in comparison to thin films, nanowire array based solar cells have an intrinsic antireflection effect that increases absorption in short wavelength range. Although this paper focuses on silicon nanowire arrays, results obtained are also of interests to other photovoltaic devices using nanowires as electrodes.

4.2 Transfer matrix method

4.2.1 Periodic nanowire structure

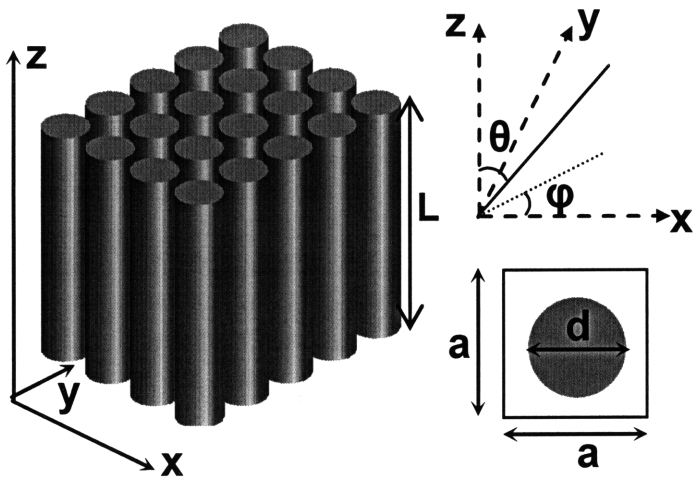

Figure 4-1: Schematic drawing of the periodic silicon nanowire structure. The parameters are the length L, the period a, and the diameter d. In the figure, θ and φ are the zenith and azimuthal angles, respectively.

Figure 4-1 shows the schematics of the periodic nanowire structure under study. The direction of the incoming solar radiation is determined by the zenith (θ) and azimuthal (φ) angles. The parameters of the structure are the period *a* of the square lattice, wire diameter *d* and wire length *L*. We consider two limiting cases for the substrate: air and perfect metal. In our analysis, we consider crystalline silicon nanowires with diameters between 50nm and 80 nm, which are readily fabricated by current nano-fabrication techniques [99, 100]. For wires with such small diameters, we need to take into account the wave effects by solving the full wave vector Maxwell's equations.

4.2.2 Discretization of Maxwell's equations in frequency domain

In this chapter, we solve Maxwell's equations in frequency domain, which is a natural choice because the optical data of silicon is given in frequency domain in literature. The unique contribution in this work is that an improved discretization form has been developed for field propagation when numerically solving Maxwell's equations.

Maxwell's equations in the integral form are given by

$$\oint \vec{E} \cdot d\vec{l} = -\frac{\partial}{\partial t} \oiint \vec{B} \cdot d\vec{S} \tag{1}$$

$$\oint \vec{H} \cdot d\vec{l} = \frac{\partial}{\partial t} \oiint \vec{D} \cdot d\vec{S} \tag{2}$$

Transform Eqs. (1) and (2) into frequency domain to yield

$$\oint \overrightarrow{E_\omega} \cdot d\vec{l} = -j\omega\mu_0\mu \oiint \overrightarrow{H_\omega} \cdot d\vec{S} \tag{3}$$

$$\oint \overrightarrow{H_\omega} \cdot d\vec{l} = j\omega\varepsilon_0\varepsilon \oiint \overrightarrow{E_\omega} \cdot d\vec{S} \tag{4}$$

where j is the imaginary unit, E_ω is the electric field in frequency domain, H_ω is the magnetic field in frequency domain, ω is the radial frequency, l is the integral path, S is the surface enclosed by the path, and ε and μ are the permittivity and permeability, respectively. For convenience, the subscript ω is dropped from now on. All the field quantities are by default in frequency domain. For the geometry shown in Fig. 4-1, there is no known analytical solution to Maxwell's equations. We need to resort to numerical approach. The transfer matrix method (TMM) has been proven to be very effective for dealing with such periodic structures [101, 102]. The TMM is a finite difference frequency domain method, where the fields on one side of a unit cell are related to those

on the end by a transfer matrix. The reflection and transmission matrices of a structure can then be obtained by decomposing the fields into plane wave components.

The discretization of Eqs. (3) and (4) are done at a grid scheme similar to the Yee grid adopted in the finite difference time domain method [103]. Figure 4-2 shows two interlaced cubic lattice, shifted from each other by a vector of $\frac{1}{2}(a\hat{x}+b\hat{y}+\hat{c})$.

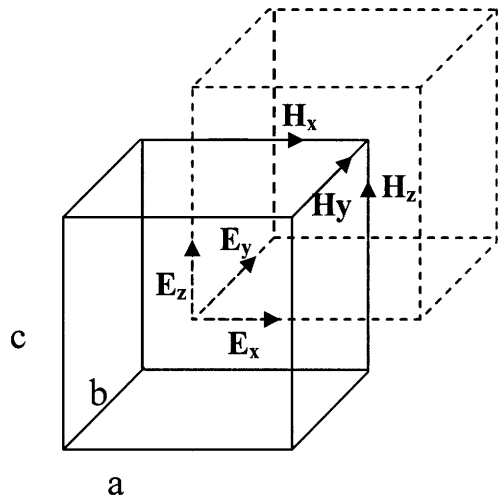

Figure 4-2: The discretization scheme. The two lattices are shifted by a vector of $\frac{1}{2}(a\hat{x}+b\hat{y}+\hat{c})$.

On the lattice shown in the above figure, the integral form of Maxwell's equations can be discretized as

$$H_x\left(\vec{r}-\vec{b}\right)a+H_y\left(\vec{r}\right)b-H_x\left(\vec{r}\right)a-H_y\left(\vec{r}-\vec{a}\right)b=j\omega\varepsilon_0\varepsilon\left(\vec{r}\right)E_z\left(\vec{r}\right)ab \qquad (5)$$

Similarly, we can obtain another 5 separate equations for the components of the electric and magnetic fields:

$$H_y\left(\vec{r}-\vec{c}\right)b+H_z\left(\vec{r}\right)c-H_y\left(\vec{r}\right)b-H_z\left(\vec{r}-\vec{b}\right)c=j\omega\varepsilon_0\varepsilon\left(\vec{r}\right)E_x\left(\vec{r}\right)bc \tag{6}$$

$$H_z\left(\vec{r}-\vec{a}\right)c+H_x\left(\vec{r}\right)a-H_z\left(\vec{r}\right)c-H_x\left(\vec{r}-\vec{c}\right)a=j\omega\varepsilon_0\varepsilon\left(\vec{r}\right)E_y\left(\vec{r}\right)ac \tag{7}$$

$$E_y\left(\vec{r}\right)b+E_z\left(\vec{r}+\vec{b}\right)c-E_y\left(\vec{r}+\vec{c}\right)b-E_z\left(\vec{r}\right)c=-j\omega\mu_0\mu\left(\vec{r}\right)H_x\left(\vec{r}\right)bc \tag{8}$$

$$E_z\left(\vec{r}\right)c+E_x\left(\vec{r}+\vec{c}\right)a-E_z\left(\vec{r}+\vec{a}\right)c-E_x\left(\vec{r}\right)a=-j\omega\mu_0\mu\left(\vec{r}\right)H_y\left(\vec{r}\right)ac \tag{9}$$

$$E_x\left(\vec{r}\right)a+E_y\left(\vec{r}+\vec{a}\right)b-E_x\left(\vec{r}+\vec{b}\right)a-E_y\left(\vec{r}\right)b=-j\omega\mu_0\mu\left(\vec{r}\right)H_z\left(\vec{r}\right)ab \tag{10}$$

Instead of scaling H [101], we take a different approach and scale E. The vacuum impedance of electromagnetic wave is

$$Z_0=\frac{E_0}{H_0}=\frac{1}{\varepsilon_0 c_0} \tag{11}$$

where c_0 is the speed of light in vacuum. We scale the electric field with Z_0:

$$E'\equiv\frac{E}{Z_0} \tag{12}$$

The scaled electric field has the same unit as the magnetic field. Note that we can substitute the z components of the electric and magnetic fields, i.e. Eqs. (5) and (10) into Eqs. (6)-(9) and effectively deal with the x and y components only. After elimination of E_z and H_z, the equations can be reorganized as

$$E_x'\left(\vec{r}+\vec{c}\right)=E_x'\left(\vec{r}\right)+jk_0c\mu\left(\vec{r}\right)H_y\left(\vec{r}\right)$$
$$+\frac{jc}{k_0a\varepsilon\left(\vec{r}\right)}\left[\frac{H_y\left(\vec{r}-\vec{a}\right)-H_y\left(\vec{r}\right)}{a}-\frac{H_x\left(\vec{r}-\vec{b}\right)-H_x\left(\vec{r}\right)}{b}\right] \quad (13)$$
$$-\frac{jc}{k_0a\varepsilon\left(\vec{r}+\vec{a}\right)}\left[\frac{H_y\left(\vec{r}\right)-H_y\left(\vec{r}+\vec{a}\right)}{a}-\frac{H_x\left(\vec{r}+\vec{a}-\vec{b}\right)-H_x\left(\vec{r}+\vec{a}\right)}{b}\right]$$

$$E_y'\left(\vec{r}+\vec{c}\right)=E_y'\left(\vec{r}\right)-jk_0c\mu\left(\vec{r}\right)H_x\left(\vec{r}\right)$$
$$+\frac{jc}{k_0b\varepsilon\left(\vec{r}\right)}\left[\frac{H_y\left(\vec{r}-\vec{a}\right)-H_y\left(\vec{r}\right)}{a}-\frac{H_x\left(\vec{r}-\vec{b}\right)-H_x\left(\vec{r}\right)}{b}\right] \quad (14)$$
$$-\frac{jc}{k_0b\varepsilon\left(\vec{r}+\vec{b}\right)}\left[\frac{H_y\left(\vec{r}-\vec{a}+\vec{b}\right)-H_y\left(\vec{r}+\vec{b}\right)}{a}-\frac{H_x\left(\vec{r}\right)-H_x\left(\vec{r}+\vec{b}\right)}{b}\right]$$

$$H_x\left(\vec{r}+\vec{c}\right)=H_x\left(\vec{r}\right)-jk_0c\varepsilon\left(\vec{r}+\vec{c}\right)E_y'\left(\vec{r}+\vec{c}\right)$$
$$+\frac{jc}{k_0a\mu\left(\vec{r}-\vec{a}+\vec{c}\right)}\left[\frac{E_y'\left(\vec{r}+\vec{c}\right)-E_y'\left(\vec{r}-\vec{a}+\vec{c}\right)}{a}-\frac{E_x'\left(\vec{r}-\vec{a}+\vec{b}+\vec{c}\right)-E_x'\left(\vec{r}-\vec{a}+\vec{c}\right)}{b}\right] \quad (15)$$
$$-\frac{jc}{k_0a\mu\left(\vec{r}+\vec{c}\right)}\left[\frac{E_y'\left(\vec{r}+\vec{a}+\vec{c}\right)-E_y'\left(\vec{r}+\vec{c}\right)}{a}-\frac{E_x'\left(\vec{r}+\vec{b}+\vec{c}\right)-E_x'\left(\vec{r}+\vec{c}\right)}{b}\right]$$

$$H_y\left(\vec{r}+\vec{c}\right)=H_y\left(\vec{r}\right)+jk_0c\varepsilon\left(\vec{r}+\vec{c}\right)E_x'\left(\vec{r}+\vec{c}\right)$$
$$+\frac{jc}{k_0b\mu\left(\vec{r}-\vec{b}+\vec{c}\right)}\left[\frac{E_y'\left(\vec{r}+\vec{a}-\vec{b}+\vec{c}\right)-E_y'\left(\vec{r}-\vec{b}+\vec{c}\right)}{a}-\frac{E_x'\left(\vec{r}+\vec{c}\right)-E_x'\left(\vec{r}-\vec{b}+\vec{c}\right)}{b}\right] \quad (16)$$
$$-\frac{jc}{k_0b\mu\left(\vec{r}+\vec{c}\right)}\left[\frac{E_y'\left(\vec{r}+\vec{a}+\vec{c}\right)-E_y'\left(\vec{r}+\vec{c}\right)}{a}-\frac{E_x'\left(\vec{r}+\vec{b}+\vec{c}\right)-E_x'\left(\vec{r}+\vec{c}\right)}{b}\right]$$

Equations (13)-(16) relate the electromagnetic fields on plane $\vec{r}+\vec{c}$ to those on plane $\vec{r}$. A matrix form of the above equations is expressed as:

$$F\left(\vec{r}+\vec{c}\right)=\overline{\overline{T}}_i F\left(\vec{r}\right) \tag{17}$$

where $\overline{\overline{T}}_i$ is the transfer matrix of slab i that enclosed by planes $\vec{r}+\vec{c}$ and $\vec{r}$, whose elements are defined in Eqs. (13) to (16). The transfer matrix is usually a full matrix. Unless the slab is a homogeneous structure, i.e. a thin film consisting of a single material, and the matrix is diagonal. The electromagnetic field is stored in a column vector,

$$F\left(\vec{r}\right)=\begin{pmatrix} E'_x\left(\vec{r}\right) \\ E'_y\left(\vec{r}\right) \\ H_x\left(\vec{r}\right) \\ H_y\left(\vec{r}\right) \end{pmatrix} \tag{18}$$

The field on plane $\vec{r}+\sum_i \vec{c}_i$ can be calculated by matrix multiplication,

$$F\left(\vec{r}+\sum_i \vec{c}_i\right)=\left(\prod_i \overline{\overline{T}}_i\right)F\left(\vec{r}\right)=\overline{\overline{T}}F\left(\vec{r}\right) \tag{19}$$

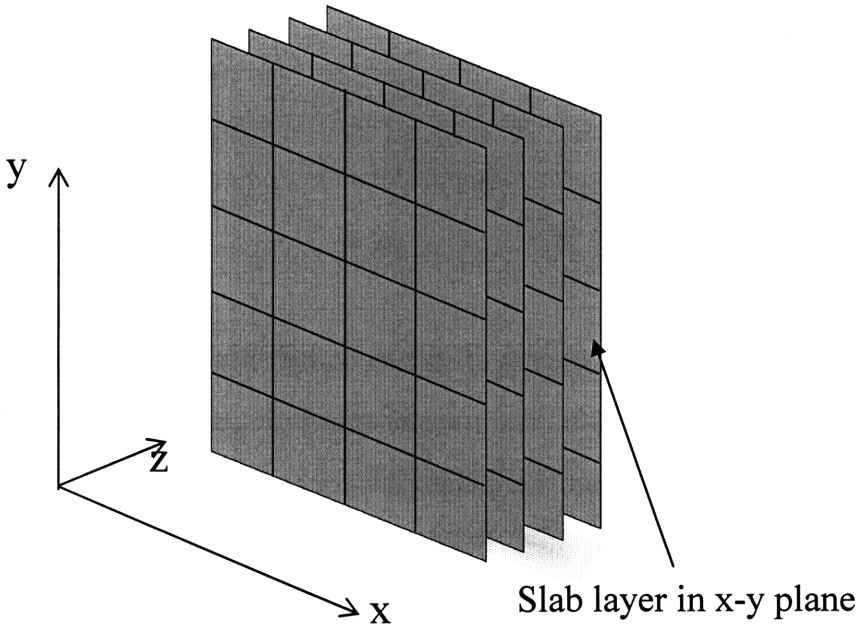

Figure 4-3: The calculation domain is divided into slabs in z direction.

The field on plane $\vec{r}$ is propagated to plane $\vec{r}+\sum_i \vec{c_i}$ layer by layer as shown in Fig. 4-3.

To ensure numerical stability of the field propagation, we choose the value of c in the discretized Maxwell's equations to make the matrix diagonally dominant. We require

$$MAX\left\{\begin{array}{l}\left|k_0 c\mu(\vec{r})\right|,\left|k_0 c\varepsilon(\vec{r})\right|,\left|\frac{c}{k_0 ab\mu(\vec{r})}\right|,\left|\frac{c}{k_0 b^2\mu(\vec{r})}\right|, \\ \left|\frac{c}{k_0 a^2\mu(\vec{r})}\right|,\left|\frac{c}{k_0 ab\varepsilon(\vec{r})}\right|,\left|\frac{c}{k_0 b^2\varepsilon(\vec{r})}\right|,\left|\frac{c}{k_0 a^2\varepsilon(\vec{r})}\right|\end{array}\right\}<1 \qquad (20)$$

The requirement can be met by setting a sufficiently small c value. In comparison, the discretized form adopted in [101] does not have the flexibility. However, cautions need to be taken when performing practical calculations, especially for 3-dimensional structures.

The size of the transfer matrix is $O\left(N^2\right)$ and matrix operation is on the order of $O\left(N^3\right)$, where N is the total number of grid points in a slab surface. A fine grid in z direction can lead to enormous computational load. In practice, a balance between numerical stability and the computation load.

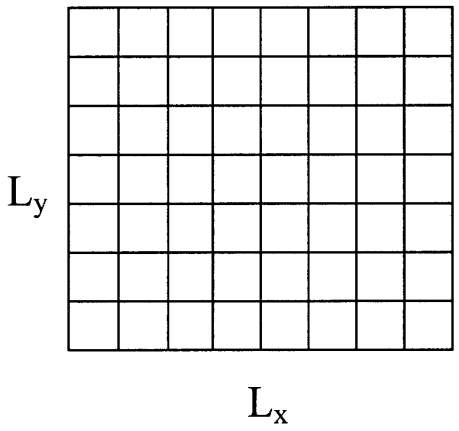

Figure 4-4: Unit cell in the x-y plane. L_x is the length of the unit cell in the x direction and L_y is the length in the y direction. Grid lines are shown in the figure.

For a periodic structure illuminated by a plane wave, Bloch boundary conditions can be applied. For example, if we have a structure that is periodic in the x-y plane (Fig. 4-4), the boundary conditions are given by

$$\begin{pmatrix} E_x'\left(\vec{r}+L_x\hat{x}\right) \\ E_y'\left(\vec{r}+L_x\hat{x}\right) \\ H_x\left(\vec{r}+L_x\hat{x}\right) \\ H_y\left(\vec{r}+L_x\hat{x}\right) \end{pmatrix} = \exp\left(jk_xL_x\right) \begin{pmatrix} E_x'\left(\vec{r}\right) \\ E_y'\left(\vec{r}\right) \\ H_x\left(\vec{r}\right) \\ H_y\left(\vec{r}\right) \end{pmatrix} \tag{21}$$

$$\begin{pmatrix} E_x'\left(\vec{r}+L_y\hat{x}\right) \\ E_y'\left(\vec{r}+L_y\hat{x}\right) \\ H_x\left(\vec{r}+L_y\hat{x}\right) \\ H_y\left(\vec{r}+L_y\hat{x}\right) \end{pmatrix} = \exp\left(jk_yL_y\right) \begin{pmatrix} E_x'\left(\vec{r}\right) \\ E_y'\left(\vec{r}\right) \\ H_x\left(\vec{r}\right) \\ H_y\left(\vec{r}\right) \end{pmatrix} \tag{22}$$

where k_x and k_y are the components of the wave vector of the incident plane wave in the x and y directions, respectively.

In general the structures to be studied are not homogeneous. Therefore for a plane wave incident on such a structure, the reflected waves and transmitted waves contain more than one single wave vector [104]. The transmission and reflection phenomenon then must be described by matrices. Using the transfer matrix method, the reflection and transmission matrices can be calculated by decomposing the field onto plane wave basis. The transmission and reflection coefficients are then calculated by summing up the total normalized flux of the transmitted and reflected waves, respectively. In Pendy's work [101], detailed derivations are given regarding these procedures. Interested readers should refer to [101] for the mathematical derivations. This work essentially follows the same approach to calculate those two matrices and correspondingly the transmission and reflection coefficients.

4.3 Silicon nanowire structures

4.3.1 Effects of wire length on optical absorption

In our calculations, we use a fine grid (4.5nm×4.5nm×4.5nm), which is much less than 1/10 of the shortest wavelength in the whole computation domain, in order to ensure the convergence. By energy balance, the absorptance of the wire structure is given by $A(\omega) = 1-R(\omega)-T(\omega)$, where ω is the frequency of the incident wave, and R, T and A are the

frequency dependent reflectance, transmittance and absorptance of the wire structure. The transmittance and absorptance are obtained using the transfer matrix method described in section 4.2. The frequency range of interest is from 1.1 eV to 4 eV where most of the above-bandgap photons concentrate in silicon-based materials. In this frequency range, the permittivity of silicon shows dispersion. In this paper, we only consider lightly doped silicon [96]. At frequencies above the bandgap, the difference in the optical constants between lightly doped and intrinsic silicon is negligible [105], which gives us the convenience of using the same optical constants for both p and n regions of the core-shell structure in a silicon nanowire solar cell. For the calculations, we take the experimentally measured optical constants of intrinsic silicon from ref. [88].

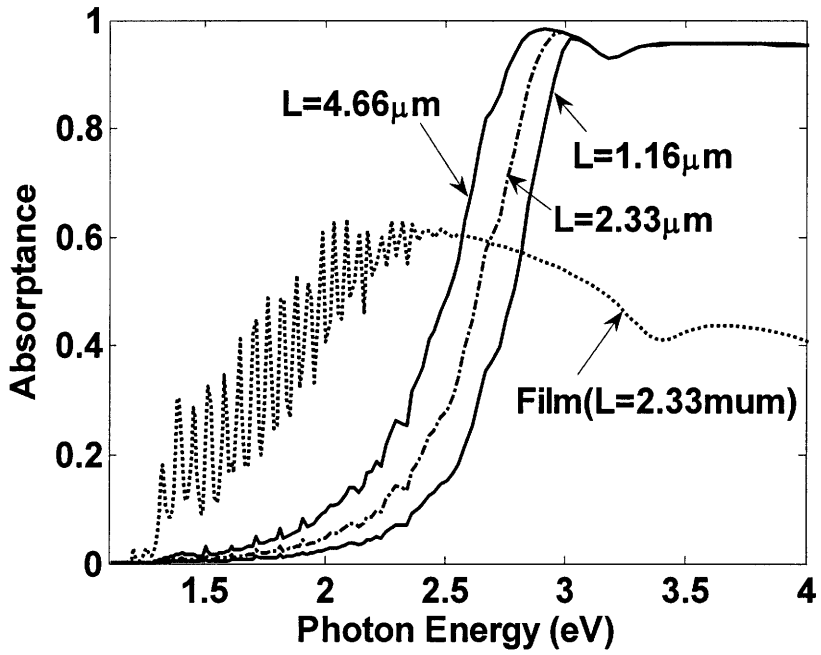

(a)

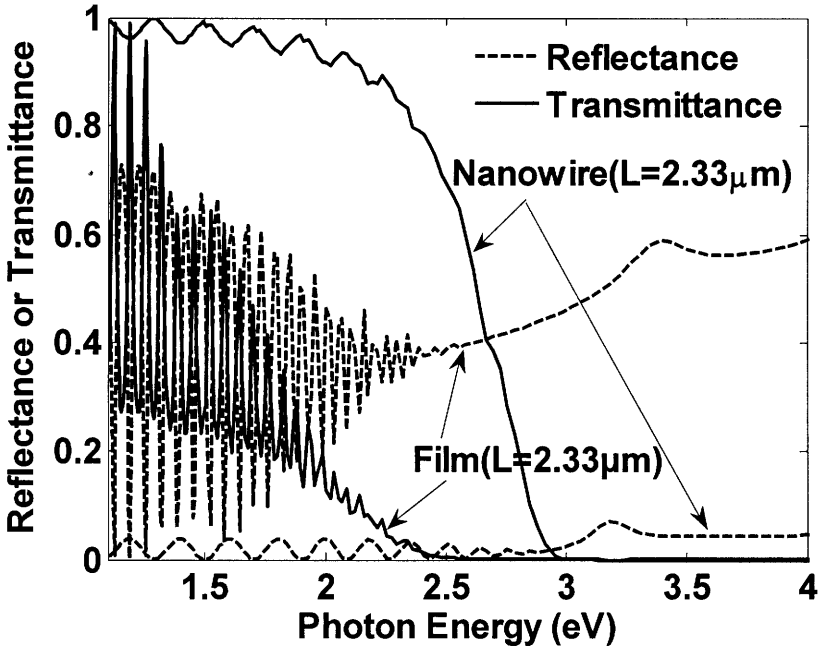

(b)

Figure 4-5: Radiative properties of nanowire structures with various thickness, (a) absorptance of nanowires with L = 1.16μm, 2.33μm and 4.66 μm (d = 50 nm and a = 100 nm). The absorptance of a thin film is included as a reference, and (b) reflectance of nanowires and the thin film.

Figure 4-5(a) shows the optical absorptance of an array of silicon nanowires with a diameter of 50 nm. The incident wave is normal to the x-y plane with the electric field polarized along the x axis. Three wire lengths, 1.16 μm, 2.33 μm and 4.66 μm, are selected to show the thickness-dependent absorption. These lengths are comparable to the film thickness in silicon thin film solar cells [44, 106, 107]. The absorptance of a 2.33 μm silicon thin film is also plotted in the same figure as a reference. As seen in the figure, for photons with energy just above the 1.1 eV bandgap, the optical absorption is very limited for all wire lengths, due to the fact that silicon has an indirect bandgap and the optical absorption needs phonon assistance. As the frequency increases, the absorption of nanowires rises and reaches a plateau region shared by all lengths. The absorptance for

nanowires in the plateau region is higher than that of the optically denser thin film, while in the low energy photon regime the absorption in the film is more efficient.

The total absorption in the nanowire structure is determined by both reflection and transmission. In order to understand the trend of absorption in nanowire arrays, in Fig. 2b we plot the reflectance and transmittance for a nanowire structure (d = 50 nm and a = 100 nm) and a thin film. Both structures have a thickness of 2.33 μm. Note that the period of the cell we consider is smaller than the wavelength range of interest such that only the zeroth-order reflection and transmission exist. It can be seen that the reflectance of nanowires is significantly lower than that of the thin film in the entire spectral range, due to the reduced density of the nanowire structures. For low frequencies, the extinction coefficient of silicon is small and interference effects exist, resulting in the oscillation of reflectance and transmittance. The interference effect is much stronger in the film than in the nanowire array, again due to the decreased density of the nanowire array. In the high frequency regime, the absorption increases and the interference effect diminishes around 3 eV. In Fig. 4-5(b), the transmittances for the nanowire and the thin film are also presented. In the low frequency regime, the figure shows that the transmittance of the nanowire structure is higher than the thin film. The higher transmittance cannot be compensated by the low reflectance, leading to insufficient absorption of low energy photons in the nanowire structure.

It is interesting to note that such small reflection in the entire spectrum can only be achieved in the thin film solar cell by applying special anti-reflection coatings [43, 46, 107]. It is the combined effect of small reflection and zero transmittance in the high frequency regime that causes higher absorption in nanowires than their thin film counterparts. It may appear surprising that in the high frequency regime the transmittance of the nanowires is zero, considering the structure is "porous". In fact, when the diameter of the nanowire is comparable to or smaller than the wavelengths of incident solar light, the geometric-optics definition of incident area does not apply. A nanowire can actually absorb not only the portion of a wave incident directly on it, but also the surrounding

wave. It is well known that a small single particle can have larger absorption cross-section than its geometric cross-section [108]. The total absorption of the incident wave in nanowires is another example of this small size effect in a clustered structure. However, despite the superior optical absorption ability in the high frequency regime, the extinction coefficient of silicon is too small to absorb the long wavelength solar radiation. Increasing the length of nanowires is needed to enhance the absorption, as shown in Fig. 4-5(a), where the absorption in the low frequency regime is improved by using longer nanowires.

4.3.2 Effects of wire diameter on optical absorption

The absorptance of nanowire structures with different filling ratios is shown in Fig. 4-6(a). The incident wave is normal to the x-y plane with the electric field polarized along the x axis. All structures have a fixed period of 100 nm and wire length of 2.33 μm, but the wire diameter varies. As a reference, the absorptance of a silicon thin film (2.33 μm in thickness) is presented in the same figure. For comparison, the absorptance based on the Maxwell-Garnett effective medium approximation[109, 110] is also plotted in the same figure. The effective dielectric function ε solves the following equation:

$$\frac{\varepsilon - \varepsilon_2}{\varepsilon + L\varepsilon_2} = f\frac{\varepsilon_1 - \varepsilon_2}{\varepsilon_1 + L\varepsilon_2} \tag{23}$$

where f is the volumetric filling ratio of the embedded material, L = 1 for two-dimensional system and L = 2 for three-dimensional system, ε_1 and ε_2 are the dielectric functions of the embedded material and the host medium, respectively.

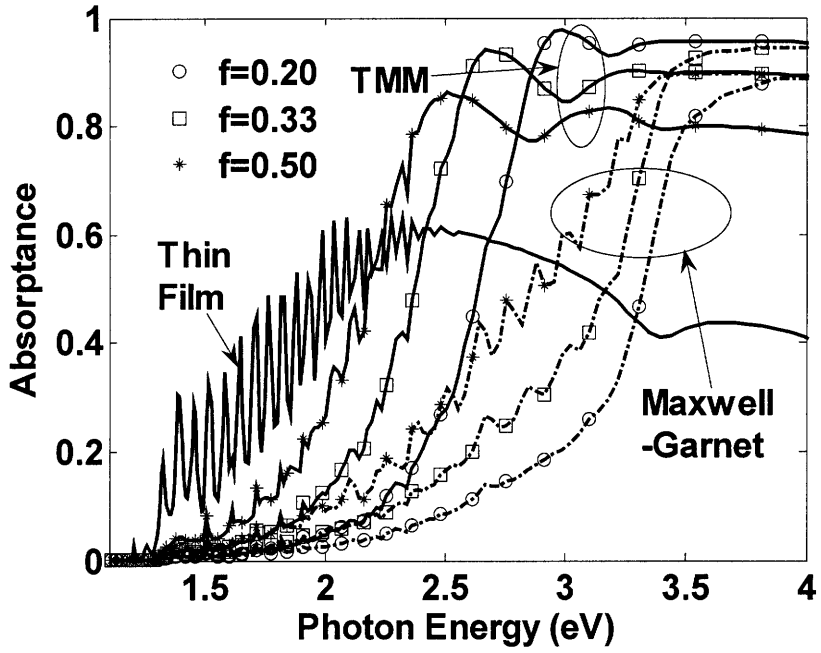
f=0.20
f=0.33
f=0.50
TMM
Thin
Film
Maxwell
-Garnet
Absorptance
Photon Energy (eV)
0
0.2
0.4
0.6
0.8
1
1.5
2
2.5
3
3.5
4

(a)

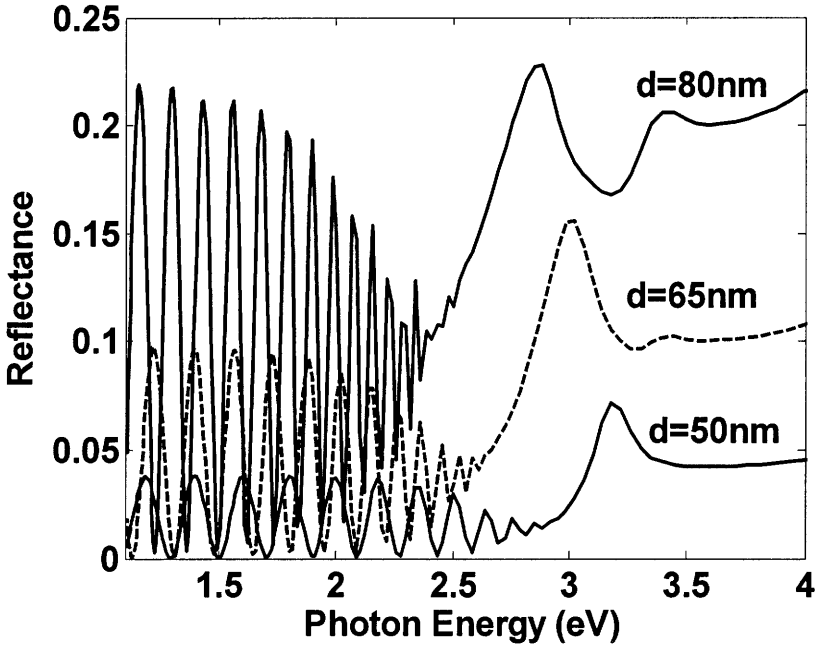
d=80nm
d=65nm
d=50nm
Reflectance
Photon Energy (eV)
0
0.05
0.1
0.15
0.2
0.25
1.5
2
2.5
3
3.5
4

(b)

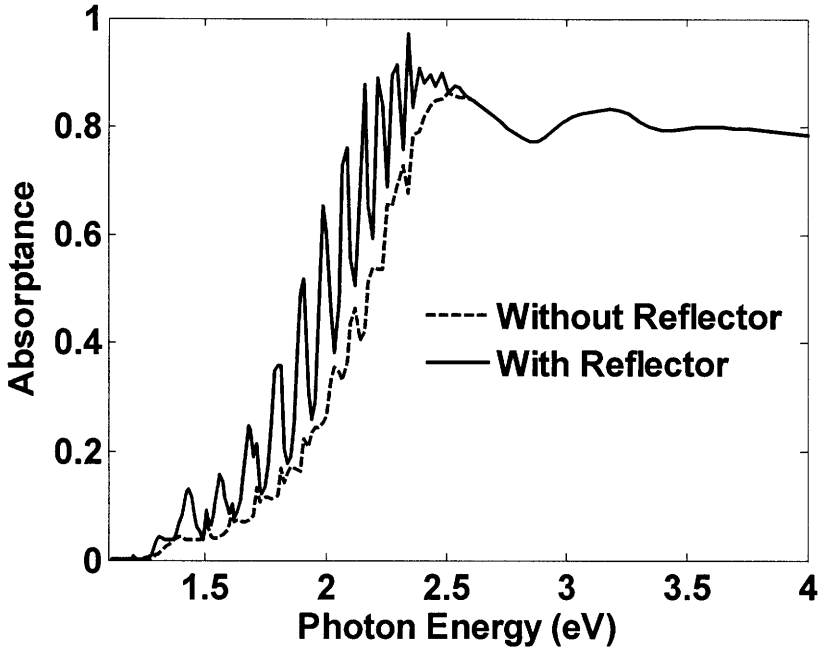

(c)

Figure 4-6: Radiative properties of silicon nanowire structures with various filling ratios, (a) absorptance obtained by TMM and Maxwell-Garnet approximation, (b) reflectance of nanowires with diameter of 50 nm, 65 nm and 80nm, and (c) absorptance of nanowires with and without a back reflector (d = 80nm).

Maxwell-Garnett approximation generally follows the trend given by the TMM results but does not agree very well with the exact numerical solutions. This discrepancy is expected because Maxwell-Garnett theory is based on the assumption that the dielectric inclusion is dilute, while in closely packed nanowire structures the electromagnetic interaction between nanowires cannot be neglected. Figure 4-6(b) shows the reflectance of the nanowire structures, where smaller filling ratios yield less reflection consistently. However, as seen in the figure, larger filling ratios give higher absorption in the low frequency regime for the same wire length; while in the high frequency regime nanowires with smaller filling ratios absorb more light. In order to evaluate the overall absorption performance of the nanowire structures in the solar spectrum, we calculated the ultimate efficiency [32] using the Air Mass 1.5 direct normal and circumsolar spectrum [34]:

$$\eta = \frac{\int_{\nu_g}^{\infty} \frac{I_\nu \nu_g}{\nu} d\nu}{\int_{\nu_g}^{\infty} I_\nu d\nu} \quad (1)$$

where ν is the photon frequency, I_ν the spectral solar intensity, and ν_g is the freqency corresponding to the silicon bandgap. Equation (1) assumes each photon with energy greater than the bandgap produces only one electron-hole pair with energy equal to $h\nu_g$, with the excessive energy converted to heat. The absorption efficiencies are 5.80%, 9.47%, 12.50% and 15.50% for the 50 nm, 65 nm, 80 nm nanowires and the thin film respectively. The calculations show that by changing filling ratios, a nanowire structure can have overall absorption efficiency close to its thin film counterpart. Furthermore, the long wavelength absorption in nanowire structures can be improved to some extent by employing light trapping to increase the optical path [45, 109]. As a proof of concept, we show in Fig. 4-6(c) that by putting a perfect reflecting mirror (100% reflectivity) on the backside of the 80 nm nanowire structure, the overall absorptance efficiency is enhanced from 12.50% to 16.09%, due to the enhancement in the long wavelength (low frequency) regime.

We have considered normal incidence ($\theta = 0^o$) with the electric field polarized along the x axis ($\varphi = 0^o$) heretofore. Figure 4-7 shows the absorptance of a nanowire structure (no back reflector) with a = 100 nm, d = 80 nm and L = 2.33 μm for nonzero θ and φ angles. As shown in the figure, the difference between TE polarized light with (θ, φ) = (0^o, 0^o), (0^o, 20^o), and (0^o, 40^o) are negligible, suggesting that for the wavelengths of interest the nanowire structure is almost isotropic in the x-y plane. When the incidence is oblique ((θ, φ) = (30^o, 0^o)), TE polarization has lower absorption than TM polarization since the latter has an electric field component along the wire axis which facilitates the absorption.

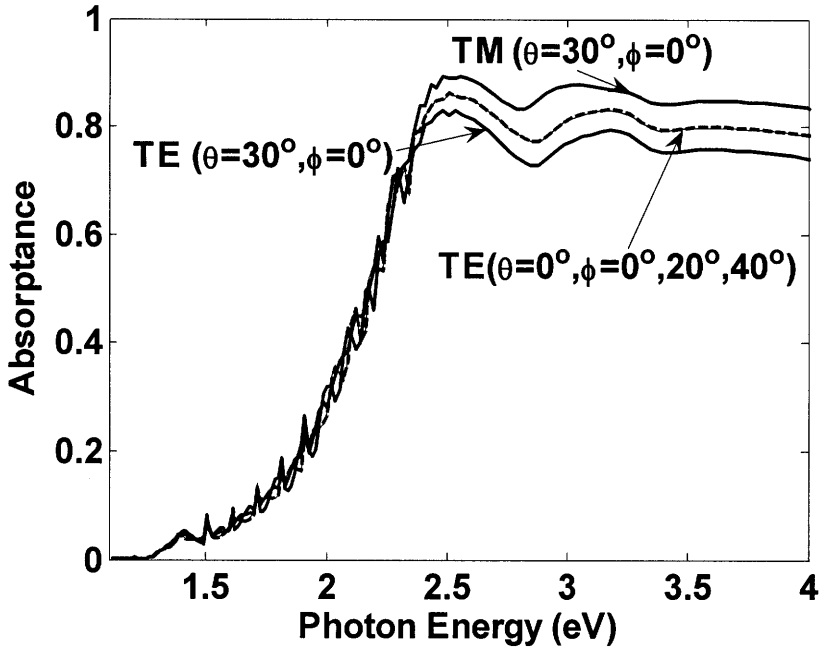

Figure 4-7: Angular dependence of absorptance for a silicon nanowire structure with d = 80 nm, a = 100 nm and L = 2.33 μm. The absorptance curves of $\varphi = 0^{\circ}$, 20° and 40° are overlapped.

4.4 Optical absorption in InSb nanowire

Similar calculation is performed on InSb nanowires. Indium antimonide is a narrow bandgap semiconductor material, which is widely used in infrared detectors and TPV cells. Figure 4-8 shows the optical absorption in InSb nanowire structures. The light is incident in the normal direction. As shown in the figure, similar optical properties are found as those in silicon nanowire structures. Generally, optical absorption is improved in high energy regime with the wire structures. Higher filling ratio also lead to more absorption in low energy regime but less absorption in high energy regime. Longer wires tend to result in better overall absorption. Compared to silicon, Indium antimonide has a direct bandgap, leading to improved near-bandgap optical absorption as shown in the figure.

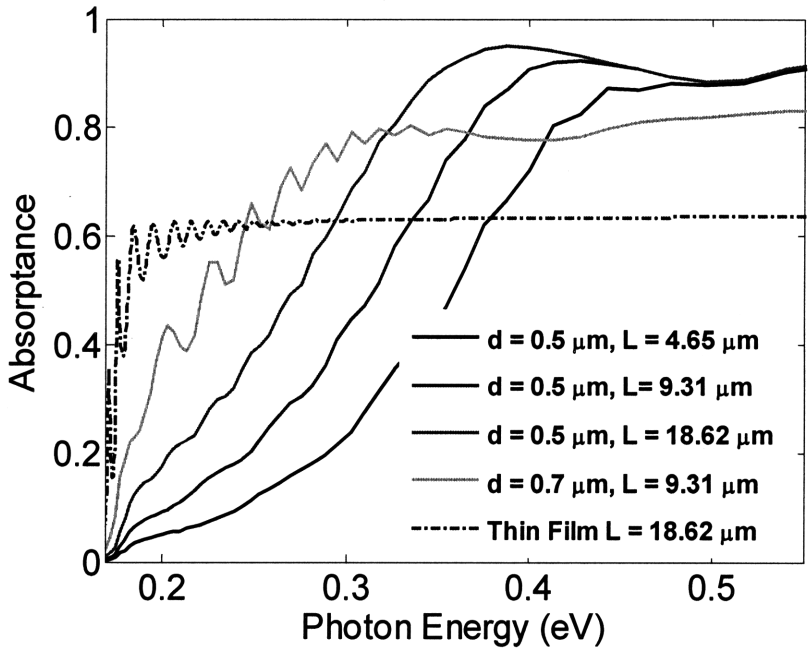

Figure 4-8: Absorptance for InSb nanowire structures with a = 800 nm and different diameters and lengths. The light is incident in the normal direction.

4.5 Conclusion and discussion

In summary, we have studied the optical absorption in periodic nanowire structures for photovoltaic applications. Our calculation shows that the electromagnetic interaction between nanowires cannot be neglected which invalidates the Maxwell-Garnett approach. Compared to thin films, the nanowire structures have the advantage of small reflection in a wide spectrum range, which can be achieved without specially designed antireflection coatings. The small reflection from the nanowire structures improves the optical absorption significantly in the high frequency regime, whereas in the low frequency regime the improvement cannot be achieved due to the small extinction coefficient of silicon. The less ideal absorption in the low frequency regime can be overcome by applying light trapping techniques or using longer wires. Similar conclusion can be drawn for InSb nanowire structures.

Chapter 5

Surface-Plasmon Enhanced Near-Bandgap Light Absorption in Silicon Photovoltaics

5.1 Introduction

One key challenge for silicon-based solar cells is the weak absorption of long-wavelength photons near the bandgap (1.1eV) due to the indirect bandgap of silicon [45, 48]. A large fraction of the AM 1.5 solar spectrum falls into a regime (0.7 μm – 1.1 μm) where silicon does not absorb light well [34]. The capture of these long-wavelength photons imposes a particular problem to the thin-film silicon solar cells. For this reason, thin-film silicon solar cells often incorporate some forms of light trapping mechanisms.

As the optical absorption rate in a lossy medium depends on the optical path length and the local electric field intensity, two different light trapping strategies have been developed. The most widely used strategy for light trapping is applying complex textures on the back or the front surfaces of the cells [107]. The surface textures diffuse the incoming light and enhance the absorption by increasing the optical path length of the photons. It was not until recently that another light trapping strategy – increasing the local field intensity via surface-plasmons using metal nanoparticles – started to receive attentions [49, 50, 110, 111]. Plasmons are collective oscillations of the conduction band

electrons excited by incident electromagnetic waves [112]. Surface plasmons are bounded to the interface when the dielectric constants of the two sides satisfy certain conditions, depending on the geometry [113]. These localized surface modes are supported in noble metals such as gold and silver. It has long been observed that surface plasmons can lead to significant electric field enhancement near the surface and thus increase the rate of any processes that depend on the field intensity. One well-known example is the surface-plasmon enhanced Raman scattering, where the Raman signals, proportional to the fourth-power of the electric field, can be increased many orders of magnitude using metallic nanoparticles such as silver [114]. Similar mechanisms can be applied to photovoltaic cells for light trapping. Instead of using surface textures, noble metal particles are either placed on the surface as in the case of silicon [49, 50] or embedded in the active regions as in the case of polymer-based solar cells [110] and dye-sensitized solar cells [111] as localized photon absorption centers. Experimental results show considerable increase of photo currents, especially in the long wavelength regime [49, 50, 110].

Despite the reported enhancement, to our best knowledge, detailed analyses of the surface-plasmon enhanced optical absorption are lacking for photovoltaic applications. Past research efforts rely on either simple dipole models, or numerical simulations. Catchpole *et al* used a dipole scattering model which does not apply to large particles [115]. Derkacs *et al* performed finite-element electromagnetic simulations for a single gold particle at a fixed wavelength [50]. Rand *et al* analyzed the field enhancement using two-dimensional finite-element simulations [110]. In this paper, we take an analytical approach and study the absorption enhancement by silver nanoparticles embedded in silicon, using an extended Mie scattering theory for a sphere embedded in absorbing media[54, 116]. The extended Mie scattering theory takes into account the near field components without making any far field approximations [117], which ensures the localized surface modes can be represented in the model. A single particle analysis is performed as it reveals fundamental mechanisms of the absorption enhancement,

although in real applications, multiple metal nanoparticles are deployed instead of a single particle. In photovoltaic applications the metal articles are usually randomly distributed and the primary enhancement mechanism is the localized surface modes which are less affected by the incoherent scattered light from the randomly spaced neighbors. Therefore, the results obtained from the parametric study of a single particle can serve as the first-order input parameters for the design of more complex structures involving multiple particles. In our calculations, we choose silver nanoparticles as the photon absorption centers because the plasma frequency of silver is the lowest among noble metals [118], which is ideal for solar photovoltaic applications. Our calculation shows that with the presence of a silver nanoparticle, the net absorption enhancement in silicon can be up to 50 times in the long wavelength regime. The dependence of absorption enhancement on the particle sizes shows a non-monotonic trend. Maximum enhancement is found for particles with intermediate sizes. Larger particles lead to lower enhancement, due to the retardation effect of the electromagnetic waves. Particles with radii smaller than the optimized radius give smaller enhancement, which is due to the size effects caused by boundary scattering of electrons. In addition to the extended Mie theory, we present simplified models for absorption analysis based on dipole models, which is found to be good approximations for particles with small radii. Our analysis also suggests that the absorption by the silver nanoparticle itself is significant, which should be addressed in the future.

5.2 Extended Mie scattering theory

Figure 1 shows a schematic illustration of the present analysis. The gray sphere represents a silver particle with a radius of a. Region 1 is inside the silver sphere and region 2 is in the host absorbing medium, i.e., silicon. The angle θ is the zenith angle and Φ is the azimuth angle. An imaginary sphere with a radius of R is also drawn as we will

analyze the absorption in silicon within this radius. A plane wave is propagating in the positive z direction.

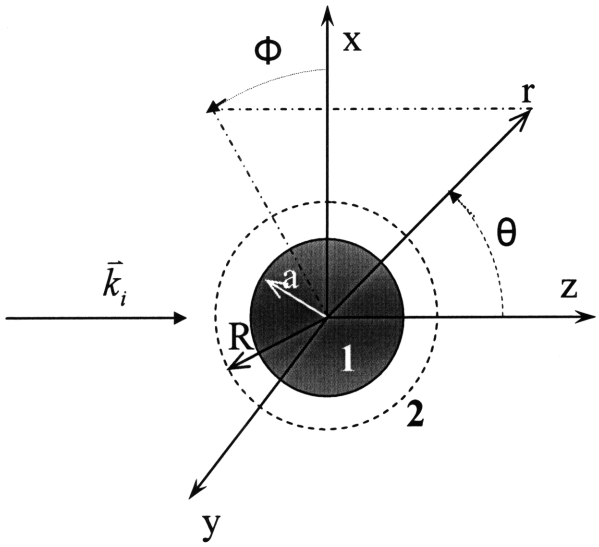

Figure 5-1: Schematic drawing of a silver particle (region 1) embedded in silicon (region 2). The gray sphere is the silver particle, which is enclosed by an imaginary spherical shell.

5.2.1 Mie scattering formulism

Without the loss of generality, we choose the electric field of the plane wave to be polarized in the x direction. The electric and magnetic fields of the incident plane wave are given by

$$\vec{E}_i = E_0 e^{jk_2 r\cos\theta}\hat{e}_x \tag{1}$$

$$\vec{H}_i = \frac{k_2}{\omega\mu_2} E_0 e^{jk_2 r\cos\theta}\hat{e}_y \tag{2}$$

where E_o is the amplitude of the electric field at z = 0, k_2 the wave vector of the incident plane wave, r the radial coordinate, ω the angular frequency, μ_2 the permeability, j the imaginary unit, $\hat{e}_x$ the unit vector in the x direction, and $\hat{e}_y$ the unit vector in the y direction. The wave vector is given by $k_2 = \frac{2N_2\pi}{\lambda}$, where N_2 is the optical constant of silicon and λ is the wavelength in vacuum. Since neither silver nor silicon is magnetic material, we have $\mu_1 = \mu_2 = \mu_0$, where subscripts 1, 2 and 0 denote regions 1, 2 and vacuum. Following procedures in ref. [54], the scattered field can be expanded into vector spherical harmonics

$$\vec{E}_s = \sum_{n=1}^{\infty} E_n \left(j a_n \vec{N}_{e1n}^{(3)} - b_n \vec{M}_{o1n}^{(3)} \right) \tag{3}$$

$$\vec{H}_s = \frac{k_2}{\omega\mu_0} \sum_{n=1}^{\infty} E_n \left(j b_n \vec{N}_{o1n}^{(3)} + a_n \vec{M}_{e1n}^{(3)} \right) \tag{4}$$

where $\vec{M}$ and $\vec{N}$ are vector spherical harmonics, $E_n = j^n E_0 (2n+1)/n(n+1)$, a_n and b_n are the expansion coefficients, and the subscripts e and o denote even and odd. The definitions of the vector spherical harmonics and the derivations of the expansion coefficients are not given here since ref. [54] contains detailed information. Note that the scattered field and the expansion coefficients derived in ref. [54] can be directly applied to the absorbing host media by treating the optical constant of the host media as complex number. We can now define the field enhancement by

$$\eta(\vec{r}) = \frac{|E_2(\vec{r})|}{|E_i(\vec{r})|} = \frac{|E_i(\vec{r}) + E_s(\vec{r})|}{|E_i(\vec{r})|} \tag{5}$$

where $r > a$.

5.2.2 Absorption in the spherical-shell region

The rate of energy absorption in a sphere with radius R is obtained by integrating the Poynting vector over the surface of the sphere [116]:

$$W_{abs}(R)=\frac{\pi|E_0|^2}{\mu_0\omega|k_2|^2}\mathrm{Re}\left\{\begin{array}{l}k_2^*\sum_{n=1}^{\infty}(2n+1)\cdot\\ \left[\begin{array}{l}j\psi_n^*\psi_n'-j\psi_n\psi_n'^*+jb_n\psi_n'^*\xi_n+jb_n^*\psi_n\xi_n'^*\\ +j|a_n|^2\xi_n'\xi_n-j|b_n|^2\xi_n\xi_n'^*-ja_n\psi_n^*\xi_n'-ja_n^*\psi_n'\xi_n^*\end{array}\right]\end{array}\right\} \quad (6)$$

where ψ_n and ξ_n are the Riccati-Bessel functions, and ψ_n' and ξ_n' are their derivatives. The symbol Re means the real component. The superscript * denotes the complex conjugate. Note that the absorption rate given in Eq. (6) differs from the standard Mie scattering theory [54] in terms of additional cross terms, due to the fact that the host medium is absorbing. For non-absorbing host media, the cross terms vanish and Eq. (6) goes back to the standard form. By energy balance, the absorption rate in the silicon spherical shell ($a < r < R$) is then given by

$$\Delta W_{abs}=W_{abs}(R)-W_{abs}(a) \quad (7)$$

Note that the absorption by the silver sphere is excluded because the photon energy absorbed in the sphere converts to heat and does not generate electricity.

To obtain the absorption enhancement, the absorption inside homogeneous silicon host medium (without the presence of a silver particle) needs to be calculated. In homogeneous medium, the scattering field is zero and the total field is identical to the

incident field. The absorption inside of a spherical region with radius r is obtained by integrating the Poyting vector over the sphere surface

$$W_{abs,Si} = \int_0^{2\pi}\int_0^{\pi}\frac{1}{2}\mathrm{Re}\left(\vec{E}_i \times \vec{H}_i^*\right)\cdot\left(-\hat{r}\right)r^2\sin\theta\cos\theta d\theta d\Phi$$
$$= \frac{\pi\,\mathrm{Re}\left(k_2\right)\left|E_0\right|^2 r^2}{\mu_0\omega}\left[\frac{\cosh\left(2k_2^{"}r\right)}{k_2^{"}r} - \frac{\sinh\left(2k_2^{"}r\right)}{2\left(k_2^{"}r\right)^2}\right] \quad (8)$$

where $k_2^{"}$ is the imaginary part of the incident wave vector. The absorption enhancement factor is defined as the ratio of Eq. (7) and Eq. (8)

$$\gamma\left(R,a\right) = \frac{\Delta W_{abs}\left(R,a\right)}{W_{abs,Si}\left(R\right)} \quad (9)$$

5.3 Scattering from silver particles

5.3.1 Optical constant of silver particle and the size effect

The optical constants are important input parameters for computing the electromagnetic fields. For the calculation of the enhancement factor, we take the experimentally measured optical constants of silicon from ref. [88]. At room temperature, the mean free path of electrons in bulk silver is around 40 nm [112]. Since in this work the diameter of the silver particles of interest is on the same order or smaller than the mean free path of the electrons, the collision of the electrons with the particle surface becomes important as an additional relaxation process [119]. The dielectric function of small silver particles should thus be modified to take account for the free electron boundary scattering, which is expressed as [120]

$$\varepsilon(\omega) = \varepsilon_{bulk}(\omega) + \frac{\omega_p^2}{\omega^2 + j\Gamma_{bulk}\omega} - \frac{\omega_p^2}{\omega^2 + j\Gamma\omega} \tag{10}$$

where Γ_{bulk} is the damping constant of bulk silver, Γ is the modified damping constant, ε_{bulk} is bulk dielectric function of silver from ref. [88], and ω_p is the plasma frequency. For silver, ω_p = 14.0×10^{15} rad/s [118]. The last two terms in Eq. (10) represent the modification to the free electron part in the dielectric function. The second term cancels the free electron contribution in the bulk medium, while the last term includes electron collisions in bulk materials as well as with the surface, by modifying the damping constant,

$$\Gamma = \Gamma_{bulk} + A\upsilon_F / a \tag{11}$$

where A = 1 and $1/\Gamma_{bulk}$ = 31×10^{-15} s [118, 120], and υ_F = 1.39×10^6 m/s is the Fermi velocity of electrons in silver [112]. Eq. (10) ensures that experimental data on the dielectric constant, which includes other optical transitions, can be used directly.

5.3.2 Simulation results

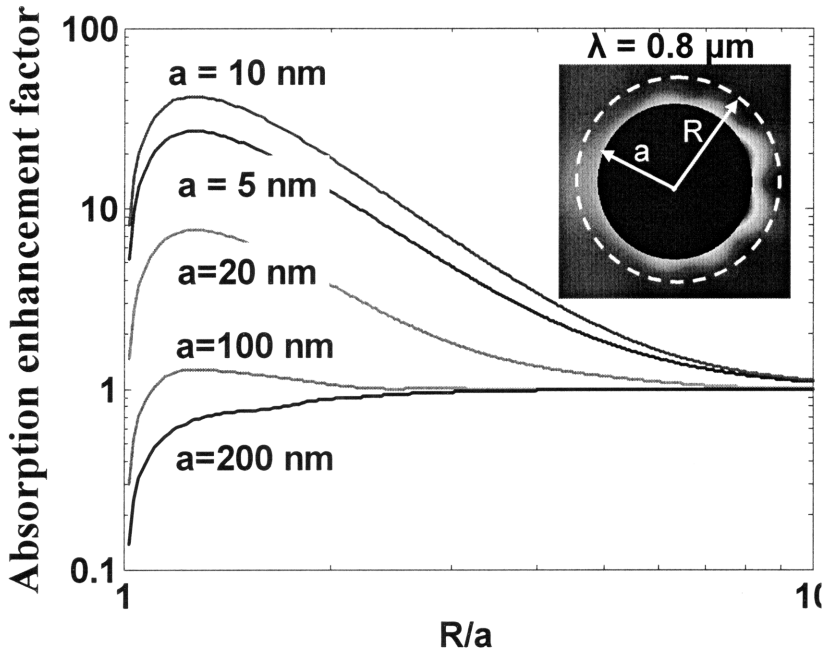

Figure 5-2: The absorption enhancement factors of silver particles with different sizes. The wavelength of the incident wave is 0.8 μm. The radius of the particle is a and the outer shell has a radius of R as shown in the insert. Note R is normalized to a.

The electric field of surface plasmons is known to concentrate only near the surface and decays rapidly when moving away from the surface, which naturally raises the question regarding the net absorption enhancement. To quantify the effects of field concentration on the absorption, the enhancement factors as defined in Eq. (9) are plotted in Fig. 5-2 in log scale for silver particles with different radii. The wavelength of the incident plane wave is set at 0.8 μm, which is the plasmon resonance wavelength of small silver particles embedded in silicon, as we will show later. Note the radius R of the outer shell is normalized to the radius of the sphere. At $R = a$, the enhancement factors for all particles are zero (not shown in the figure due to the log scale) because the imaginary

silicon spherical shell has zero thickness. When R increases to a large value, the near field effect diminishes and the enhancement factors for all cases approach 1. In the intermediate range of R, the enhancement factors reach maximum for all particles except the 200 nm one, which increases monotonically with R and never exceeds 1. As shown in the figure, smaller particles lead to larger enhancement. However, the dependence of the enhancement factor on the particle radius does not follow a monotonic trend. The 10 nm particle gives the maximum enhancement while the larger 20 nm and smaller 5 nm particles yield less enhancement. The peaks for the 5 nm and 10 nm particles are both at $R = 1.26\ a$, which suggests that the absorption enhancement is concentrated in a spherical shell with a thickness of 0.26 a.

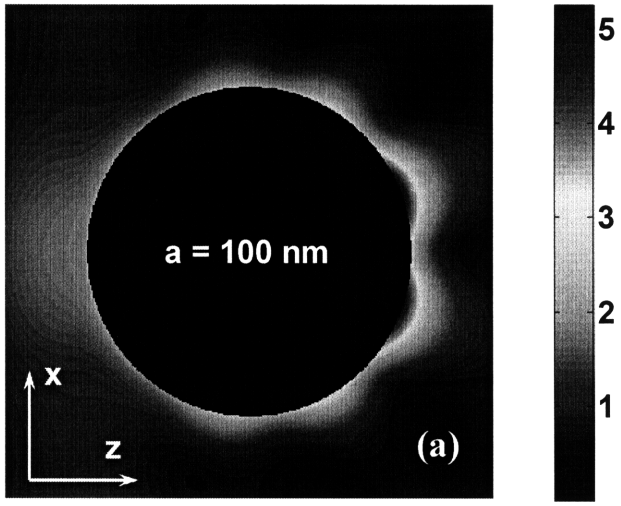

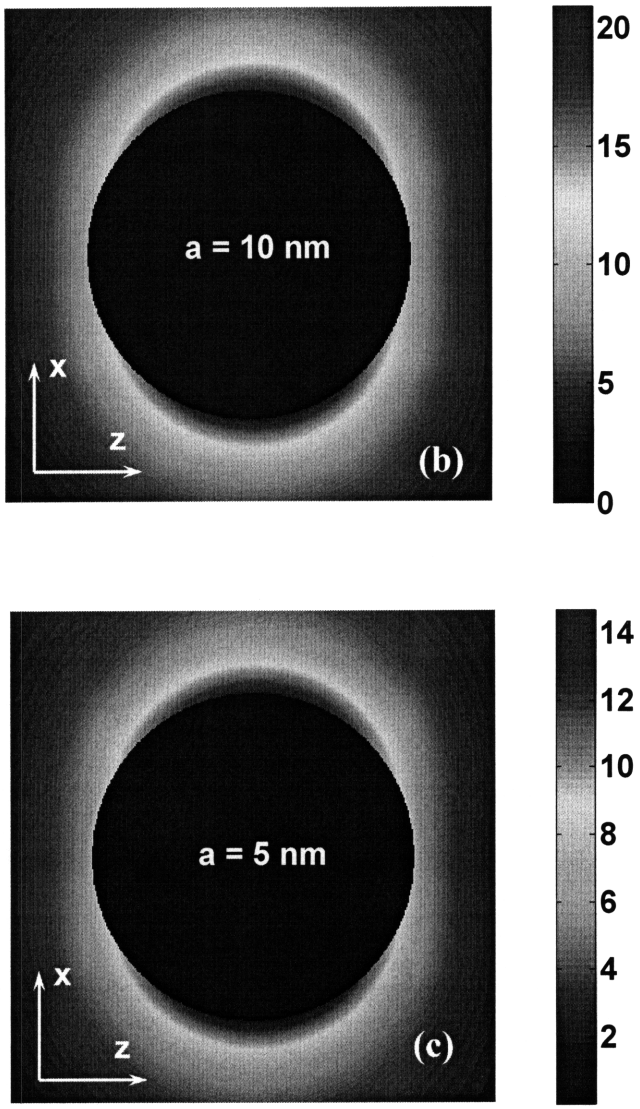

Figure 5-3: The field distributions outside the silver particles at the y = 0 plane. The field distributions are normalized to the incident plane wave as defined in Equation 5. (a) 100 nm particle (b) 10 nm particle (c) 5 nm particle.

At the wavelength of 0.8 μm, the distribution of the normalized field, or field enhancement (given by Eq. (5)), outside the 100 nm, 10 nm and 5 nm (radius) particles at the y = 0 plane is shown in Figs. 5-3 (a-c). Note 0.8 μm is the wavelength in vacuum and it is around 0.22 μm in silicon. The field pattern around the 100 nm particle clearly shows

the retardation effects of the electric field, which is anticipated because the wavelength is smaller than the particle diameter such that the interference of the scattered light is strong. As shown in the figure, the field enhancement for the 100 nm particle is rather limited and scatters around the particle surface, which is mainly due to the interference effects. Compared to the 100 nm particle, the fields around the 10 nm and 5 nm particles show a typical pattern of a dipole field and have much higher enhancement factor. The electric field is concentrated around the top and bottom of the particles where the vector of the electric field of the incident wave has the maximum component along the surface normal.

5.3.3 Dipole approximation for small particles

An interesting observation from Figs. 5-3 (b) and 5-3(c) is that the fields around the small particles (with radii of 5 nm and 10 nm) share similar distribution patterns that differ only in magnitude. Since for the 5 nm and 10 nm particles, the wavelength is more than 10 times larger than the particle diameters, the dipole model is considered to be a reasonable approximation. The field of an oscillating dipole is given by [121]

$$\vec{E} = \frac{e^{jk_2 r}}{4\pi\varepsilon_2\varepsilon_0}\left\{\frac{k_2^2\left(\hat{e}_r \times \vec{p}\right)\times\hat{e}_r}{r} + \left[3\hat{e}_r\left(\hat{e}_r\cdot\vec{p}\right)-\vec{p}\right]\left(\frac{1}{r^3}-\frac{jk_2}{r^2}\right)\right\} \tag{12}$$

where ε_0 is the permittivity of vacuum, ε_2 is the relative permittivity of silicon, and $\hat{e}_r$ is unit vector in the r direction. The dipole moment of the particle is expressed as

$$\vec{p} = p\hat{e}_x = 4\pi\varepsilon_0\varepsilon_2 E_0 a^3 \frac{\varepsilon_1-\varepsilon_2}{\varepsilon_1+2\varepsilon_2}\hat{e}_x \tag{13}$$

where ε_1 is the relative permittivity of the silver particle. Since $\lambda >> a$, the field near the particle surface is dominated by the near field terms and Eq. (12) can be simplified as

$$\vec{E} = \frac{1}{4\pi\varepsilon_2\varepsilon_0 r^3}\left[3\hat{e}_r\left(\hat{e}_r \cdot \vec{p}\right) - \vec{p}\right] \tag{14}$$

Substituting Eq. (13) into Eq. (14) leads to

$$|E| = \left|E_0 \frac{\varepsilon_1 - \varepsilon_2}{(\varepsilon_1 + 2\varepsilon_2)}\right| \sqrt{3\sin^2\theta\cos^2\Phi + 1}\left(\frac{a}{r}\right)^3 \tag{15}$$

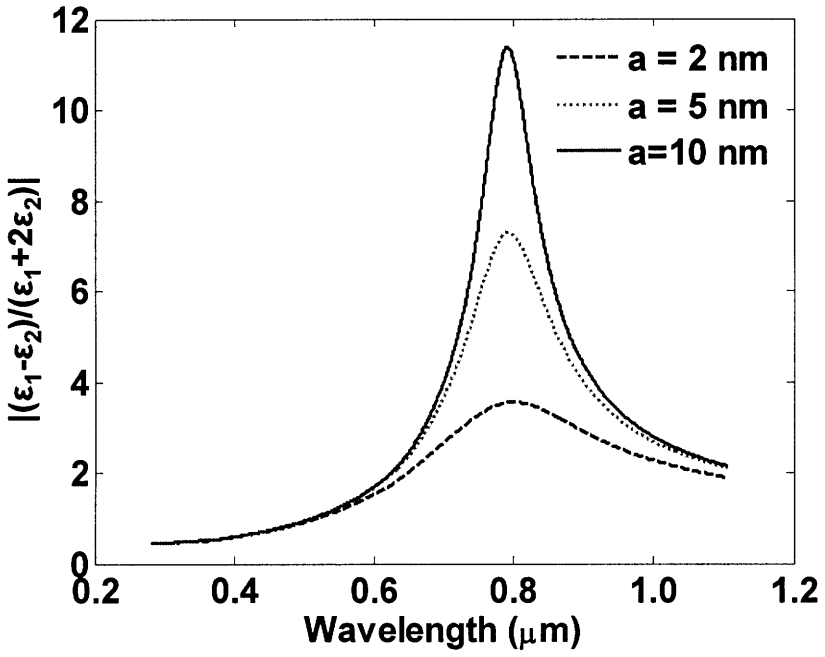

Figure 5-4: The magnitude of $|(\varepsilon_1-\varepsilon_2)/(\varepsilon_1+2\varepsilon_2)|$. The peaks for all three particles are centered at around 0.8 μm.

It is obvious that the distribution profile of the electric field only depends on $\sqrt{\left(4\sin^2\theta+\cos^2\theta\right)\cos^2\Phi+\sin^2\Phi}\left(a/r\right)^3$, which explains the similarity between Fig. 3(b) and Fig. 3(c). The magnitude of the electric field is given by $|E_0(\varepsilon_1-\varepsilon_2)/(\varepsilon_1+2\varepsilon_2)|$, which depends on the radius of the particle, since ε_2 is a function of a due to the electron scattering at the particle surface. Figure 5-4 shows $|(\varepsilon_1-\varepsilon_2)/(\varepsilon_1+2\varepsilon_2)|$ for selective particles with small radii where the dipole approximation is expected to hold with acceptable accuracy. All the curves show peaks around 0.8 μm, which is the resonance plasmon wavelength when the denominator $(\varepsilon_1+2\varepsilon_2)$ approaches zero.

Furthermore, using the dipole approximation, the absorption in the silicon shell (Eq. (7)) has a closed analytical form

$$\begin{aligned}\Delta W_{abs}\left(R,a\right) &= \int_0^{2\pi}\int_0^{\pi}\int_a^R \frac{1}{2}\varepsilon_2^{"}\left|E^2\right|r^2\sin\theta dr d\theta d\Phi \\ &= \pi\varepsilon_2^{"}\left|E_0\frac{\varepsilon_1-\varepsilon_2}{\left(\varepsilon_1+2\varepsilon_2\right)}\right|^2 a^6\left(\frac{1}{a^3}-\frac{1}{R^3}\right)\end{aligned} \tag{16}$$

where $\varepsilon_2^{"}$ is the imaginary part of the dielectric function of silicon. Taylor expansion of Eq. (8) yields

$$W_{abs,Si}\left(R\right)=\frac{4\pi\,\mathrm{Re}\left(k_2\right)k_2^{"}\left|E_0\right|^2R^3}{3\mu_0\omega}+O\left(\left(k_2^{"}R\right)^3\right) \tag{17}$$

The absorption enhancement ratio is then given by

$$\gamma\left(R,a\right)=\frac{3\mu_0\omega\varepsilon_2^{"}\left|\dfrac{\varepsilon_1-\varepsilon_2}{\left(\varepsilon_1+2\varepsilon_2\right)}\right|^2}{4\,\mathrm{Re}\left(k_2\right)k_2^{"}R^3}\left[\left(\frac{a}{R}\right)^3-\left(\frac{a}{R}\right)^6\right] \tag{18}$$

which reaches maximum when $\frac{R}{a} = \sqrt[3]{2}$, i.e. R = 1.26 a, as confirmed in Fig. 5-2 for the 5 nm and 10 nm cases. As for the larger particles, retardation effects push the maximums to smaller R values.

5.3.4 Absorption enhancement in the solar spectrum

We have studied the field enhancement at a fixed wavelength heretofore. Figure 5-5 shows the wavelength dependent absorption enhancement with R = 1.26 a. As seen from the figure, the absorption is enhanced up to 50 times with the presence of the 10 nm silver particle. Decrease of the radius from 10 nm to 5 nm and 2 nm leads to dramatic reduction in absorption. A similar trend is seen when increasing the radius of the particles, where the larger 20 nm, 40 nm and 100 nm particles give less absorption. Nevertheless, the enhancement for all particles is most significant in the wavelength regime between 0.7 μm and 1.1 μm, where the silicon does not absorb light adequately. As shown in the figure, the smaller 2 nm, 5 nm and 10 nm particles have the maximum absorption at around 0.8 μm with slight shifting of the peaks, while the larger 20 nm, 40 nm and 100 nm particles have multiple absorption peaks shifted to longer wavelengths.

For the small particles, the slight shifting of the absorption peaks from the plasmon wavelength comes from the combined effects of weak retardation and additional wavelength dependent $\varepsilon_2'' / \mathrm{Re}(k_2) k_2''$ term in Eq. (18); for the larger particles, the shifting of the absorption peak is due to the retardation effect, which causes a more pronounced variation from the resonance wavelength of 0.8 μm. The results suggest that a wide spectrum range can be covered by carefully selecting and mixing particles with different radii.

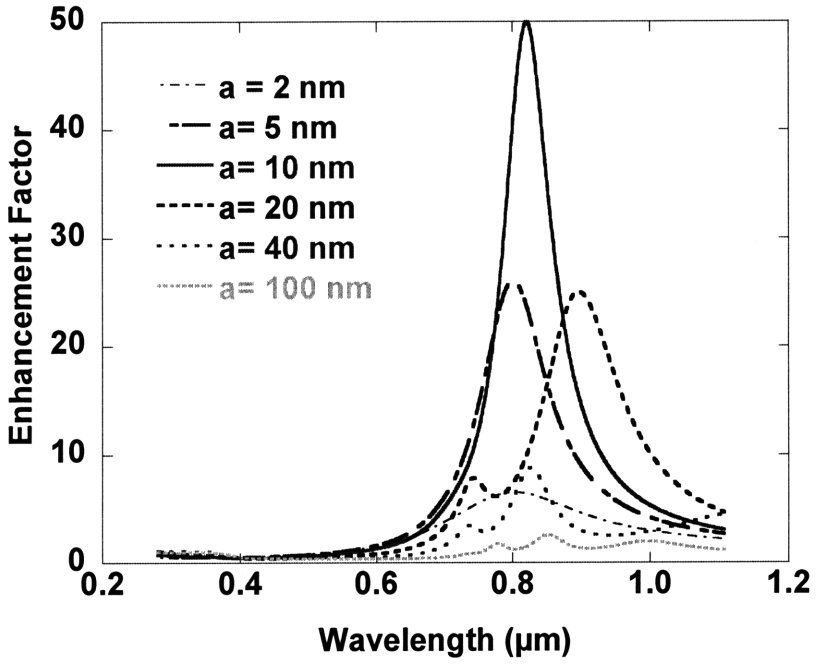

Figure 5-5: The wavelength dependent enhancement factors for particles with different radii. For all cases, R is chosen to be 1.26 a. The enhancement factor induced by a 10 nm particle is 50 at the resonance wavelength.

As revealed in our analysis, the absorption enhancement is caused by the field magnification due to the surface plasmons. However, the surface waves extend to both sides of the interface. Therefore, the unwanted absorption inside the silver particles is inevitably increased along with the absorption enhancement in silicon. Figure 5-6 shows the wasted absorption in a 10 nm particle and the absorption in the outside shell ($R = 1.26a$). The absorption is normalized to $W_{abs,Si}$(1.26a). For wavelengths larger than 0.5 μm, the silver particle absorbs significantly more light than silicon, especially in the long wavelength range, which presents a problem for the overall optical absorption efficiency. One possible solution is to use the core-shell structure [122] which has a very thin layer of metal that the corresponding absorption loss may be alleviated.

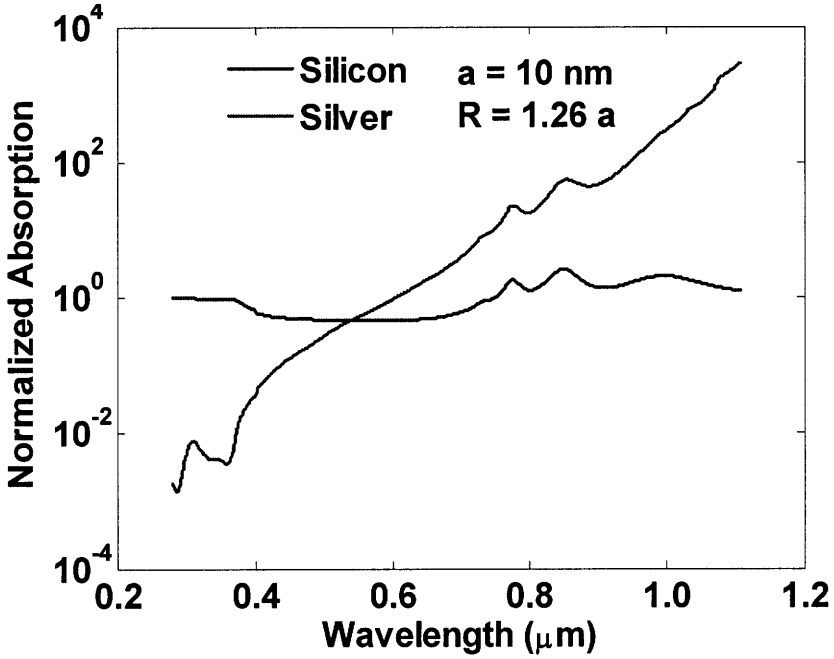

Figure 5-6: The absorption in a 10 nm silver particle. The absorption loss is significant in the long-wavelength regime.

5.4 Conclusion

In summary, we have studied the surface-plasmon enhanced absorption in silicon medium. Both extended Mie theory and dipole approximation have been used for the calculations. The field concentration effects of the surface plasmon are examined. The enhancement is found to be mostly confined in a spherical shell surrounding the particle and the optimal thickness of the shell is 0.26 a. The spectral analysis shows that the long-wavelength optical absorption in silicon can be enhanced significantly by embedded silver nanoparticles. Enhancement up to 50 times is obtained with a 10 nm silver particle while smaller and larger particles yield less enhancement.

The calculation reveals that the energy loss inside the silver particles may present a problem for efficient energy utilization, which could be potentially addressed by using novel nanostructures. We want to point out that our calculation is based on local field

enhancement induced by a single particle. Particle-particle interaction can potentially lead to even higher enhancement. Anisotropic scattering from particles may also give additional enhancement by randomizing the incident solar light.

Chapter 6

Selective Absorber Surface for Solar Thermal Applications

6.1 Introduction

Solar thermal is a technology that utilizes solar irradiance by directly converting the energy in photons into heat. The solar generated thermal energy can be used in numerous applications. Examples include solar thermal electricity generation [51, 123], solar water splitting for hydrogen production [124], or solar water heating for residential or commercial use. Unlike solar photovoltaic energy conversion where photons with energies below the bandgaps of the photovoltaic cells are usually wasted, in solar thermal applications the entire solar spectrum can be used for heat generation, which essentially eliminates the need for spectrum matching as in the case of solar photovoltaics.

A critical component that exists in all the solar thermal energy conversion systems is the solar absorber surface. The electromagnetic energy in the photons is absorbed by the solar absorber where the generated heat is carried away to working medium. For maximum system efficiency, a solar absorber should have good spectral selectivity. An ideal solar absorber surface should have absorptivity equal to one in the solar spectrum to maximize absorption of the solar energy, and have emissivity of zero in the long wavelength regime to minimize radiative heat loss. Note that "long wavelength regime" is a loose definition. The cutoff wavelength depends on the temperature of the absorbers

in specific applications. For example, for a low-temperature application where the absorber has a temperature of 100 °C, 95% of the blackbody radiation energy lies above the wavelength of 5 μm. Therefore, the long wavelength regime for temperature of 100 °C starts at 5 μm. Similarly, for an absorber at a higher temperature (300 °C), the cutoff wavelength is 3.3 μm.

Such selective absorber surfaces are not known to exist in nature. Combinations of different materials are often employed to engineer spectrally selective absorber surfaces. One of the earliest methods of fabricating highly efficient selective surfaces is to evaporate multilayer optical coatings on highly reflective substrates [75]. A typical configuration consists of thin metal layers stacked between dielectric layers. The spectral selectivity arises from wave interferences. The physics of multilayer absorber is well understood and a transfer matrix method [56] can be applied to optimize the optical properties of the multilayer structure. However, precise control of individual layer thickness is required to meet the conditions for wave interferences, which often involves costly processes such as electron-beam or sputtering deposition, leading to limited cost-insensitive applications such as space program. The most widely-used solar selective absorbers are based on metal-dielectric composites, which are fine metal particles embedded in dielectrics, also known as cermets. The available cermet-based selective absorbers range from high-end products manufactured with expensive technologies such as sputtering, chemical vapor deposition or physical vapor deposition [125-129], to low-end products produced by electroplating or pigmentation of metals [126, 130-132]. Effective medium theories such as Maxwell Garnett formalism [133] and Bruggeman model [134] are often employed to approximate the optical constants of the cerments, which are used as parameters in the transfer matrix method to calculate the optical properties of cermets [131, 135]. However, the validity of these effective medium theories becomes questionable when the filling factors are not small and the embedded particles are nonspherical. Modifications are available but they are highly dependent on the specific shapes of the particles [120, 136], which practically limits the applications of

these models. Further more, effective medium theory only provides averaged optical properties of the cermets. Analysis of local electromagnetic fields is not possible with the average optical constants, which hinders better understanding of the optical absorption process in the cermets.

6.2 Metallic structure as selective absorbers

In this chapter, the study is focused on selective absorber surfaces that are based on metallic structures. Conductive metals such as gold, silver, copper, nickel and aluminum contain a large population of free electrons. The electrons in metals interact strongly with oscillating electromagnetic field with frequencies ranging from ultraviolet to far-infrared. Despite the strong interaction between the electrons in the metal and the electromagnetic field, most metals have high reflectivity in the visible as well as the infrared regime, because the large optical constants of metals do not match well with the optical constant of the surrounding medium, e.g. air or vacuum. Although electromagnetic waves can be completely absorbed in metals in a very short distance, a large portion of the energy is reflected back.

Figure 6-1 shows the spectral directional absorptivity of flat metallic surfaces at normal incidence. Note that the emissivity equals the spectral directional absorptivity according to Kirchoff's law. Before examining Fig. 6-1, a few important numbers can be drawn from Fig. 1-2: 44% of the solar irradiance lies within 0.4 ~ 0.7 μm and 49% of the energy is in 0.7 ~ 1.8 μm, while 5% locates in the spectrum below 0.4 μm and 2% above 1.8 μm. Figure 6-1 reveals that gold, copper, aluminum and silver have low absorptivity in the near infrared, typically less than 0.1. Silver and aluminum have consistently low absorptivity in both the visible and near-infrared spectra. Gold and copper have moderately large absorptivity in the visible and show good spectral selectivity. Nickel shows reasonably high absorptivity in both visible and near-infrared. However, it has

relatively high absorptivity, i,e. emissivity in the long wavelength regime and does not have a desirable spectral selectivity.

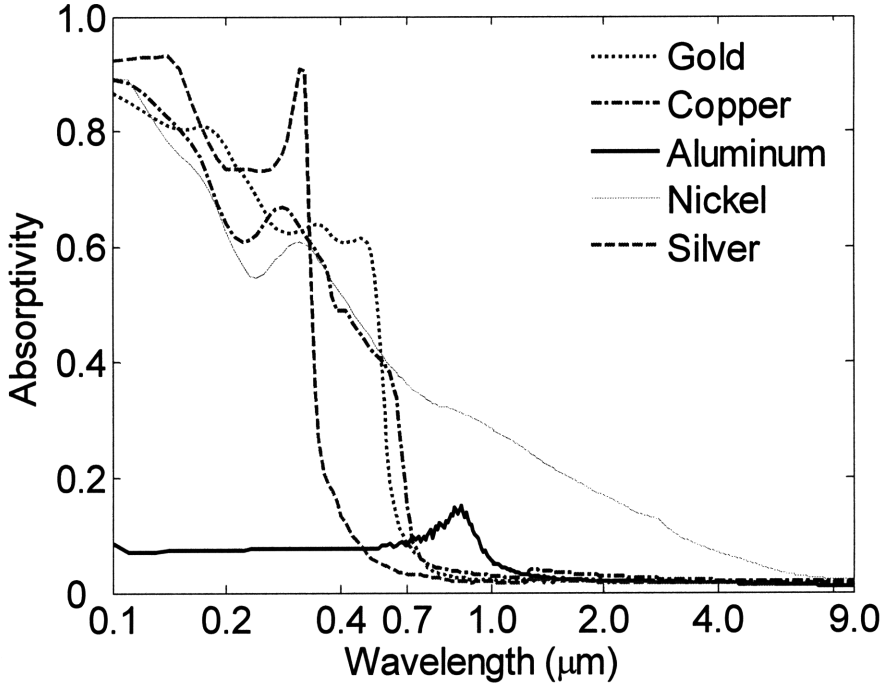

Figure 6-1: Spectral directional absorptivity of gold, copper, aluminum, nickel and silver flat surfaces at normal incidence. The axis of wavelength is given in log scale.

Although metals cannot adequately absorb solar irradiance, most of them do show potentials in the long wavelength regime where low emissivity is desired. Past work on selective absorbers proposes graded-index structures, where at the top of the surface structure the refractive index is 1 and the index gradually increases to the value of the substrate, to minimize mismatch and reduce reflection in the short wavelength regime [137, 138]. However, in cermet-based coatings, the proposed index profile is difficult to achieve due to the large optical constants of the surrounding dielectric materials. Early attempts resulted in less ideal spectral selectivity [125, 139]. In addition, the graded index imposes even greater challenge on the fabrication process. In practice, a bi-sublayer

cermet absorber structure is used [140], which nevertheless still requires complex manufacturing process.

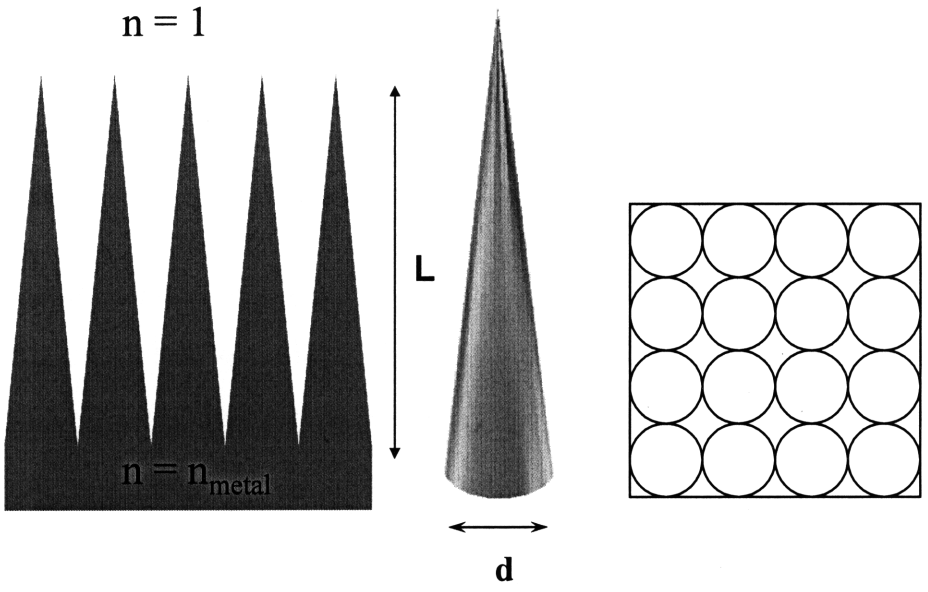

Figure 6-2: A periodic subwavelength structure. The unit cell is a metallic cone structure that has a base diameter of d and a length of L. The structure is periodic in the horizontal plane and has a square lattice as shown in the top view.

In this work, a periodic subwavelength structure is proposed to reduce reflection in the short wavelength regime. Figure 6-2 shows the structure. The structure consists of subwavelength cones as the unit cells. Each cone has a bottom diameter of d and a length of L. The structure is periodic in the horizontal plane and has a square lattice. On the top of structure, the volume fraction of metal is zero and the effective refractive index is identical to the surrounding medium. The volume fraction of metal increases along the length direction and reaches maximum at the bottom. The cone shape of the unit cell effectively creates a continuous structure that has a graded index. It should be emphasized that this approach is different from the well-known technique to increase absorption by roughening material surfaces. Roughened surfaces have features with sizes

larger than the wavelength. Multiple scattering of electromagnetic waves is the main mechanism for increased absorption in roughened surfaces, where the enhancement is usually rather limited.

6.3 Finite-difference time-domain method

To model the optical properties of the proposed cone structure, we use the finite-difference time-domain method, which originated from Yee's seminal work in 1960s [103]. The FDTD method gives direct time-domain solutions of Maxwell's differential equations on spatial grids called Yee cells. The spatial derivatives in the time-dependent Maxwell's equations are discretized by second-order central-difference. A leapfrog algorithm is used to discretize the temporal derivatives and iterates the electromagnetic fields at the Yee cells. The discretized form of Maxwell's equations is explicit in time and space, which greatly reduces the complexity in computation. Since its introduction, the FDTD method has been successfully applied in a wide range of applications. The principles and implementations of the FDTD method can be found in [55]. For FDTD simulations conducted in this work, we use a freely available software package with subpixel smoothing for increased accuracy [141]. The Scheme scripting language is employed to implement the subroutines contained in the software package.

One of the major advantages of FDTD is that the response of a structure to a wide range of frequencies can be obtained with a single run by applying a broad band pulse as the source. The pulse propagates and finally leaves the calculation domain, where the electromagnetic fields decay over time. If frequency domain results are desired, the time-dependent electromagnetic fields are recorded and Fourier-transformed to give the frequency domain counterparts. Recall that in FDTD Maxwell's equations are solved in the time domain and thus time-dependent optical properties are required as input parameters. However, experimentally measured optical properties are usually presented

in frequency domain. For dispersive materials whose permittivity and permeability are frequency dependent, a Fourier-transform back to time domain is needed in FDTD to convert the frequency domain parameters into time domain properties.

In general, it is a daunting task to accomplish the Fourier transform since available optical data of any material is usually scarce and covers only a fraction of the entire spectrum, while for accurate transform a much broader spectrum and more data points are required. Fortunately, for isotropic materials whose dielectric functions can be described by Drude or Lorentz models, analytical form of the Fourier transform is known, which can be directly implemented in FDTD algorithm [141]. In metals, conduction band electrons are free to oscillate in response to frequencies in the infrared regime. The dielectric function of metals follows the Drude model:

$$\varepsilon = \varepsilon_{\infty} - \frac{\omega_p^2}{\omega^2 + j\omega\gamma} \tag{1}$$

where ε_{∞} is the dielectric function at high frequency, ω is the radial frequency of the electromagnetic field, ω_p is the plasma frequency, γ is the damping factor, and j is the imaginary unit. Equation (1) is usually sufficient to model the optical properties of metals in the infrared regime. For the visible and near infrared regime, the effect of bound electrons has to be considered for accurate modeling. Lorentz oscillators are added to Eq. (1) to model the full spectrum [142]:

$$\varepsilon = \varepsilon_{\infty} - \frac{\omega_{p,e}^2}{\omega^2 + j\omega\gamma_e} + \sum_i \frac{\omega_{p,i}^2}{\omega_{0,i}^2 - \omega^2 - j\omega\gamma_i} \tag{2}$$

where $\omega_{0,i}$ is the resonant frequency of the i th harmonic oscillator, and the subscript e is appended to free-electron parameters.

Three metals, aluminum, copper and nickel, are considered in this work because they are relatively inexpensive compared to other materials. The optical constants of these three materials are taken from [88]. A nonlinear least-square fitting is used to fit the experimentally measured optical constants to Eq. (2). In practice, the Drude model plus four Lorentz oscillators can yield satisfactory fit for the optical constants of the three metals in the spectrum from 0.2 μm to 10 μm. The dielectric function at high frequency is chosen as the vacuum permittivity of 1 for the fitting. The other fitting parameters are presented in Table 6-1. Note that these values should be only interpreted as numerical fitting parameters, which may differ from well-known values. However, the combination of these parameters can accurately represent the experimental data of the optical constants.

Table 6.1: Fitting parameters for aluminum

ω_0 (rad/s)	ω_p (rad/s)	γ (rad/s)
	1.646×10^{16}	7.141×10^{13}
2.461×10^{14}	1.084×10^{16}	5.059×10^{14}
2.346×10^{15}	5.089×10^{15}	4.740×10^{14}
2.747×10^{15}	9.273×10^{15}	2.053×10^{15}
5.276×10^{15}	3.942×10^{15}	5.138×10^{15}

Table 6.2: Fitting parameters for copper

ω_0 (rad/s)	ω_p (rad/s)	γ (rad/s)
	1.248×10^{16}	4.558×10^{13}
4.421×10^{14}	4.064×10^{15}	5.743×10^{14}
4.492×10^{15}	5.306×10^{15}	1.604×10^{15}
8.052×10^{15}	1.399×10^{16}	4.881×10^{15}
1.699×10^{16}	1.314×10^{16}	6.540×10^{15}

Table 6.3: Fitting parameters for copper

ω_0 (rad/s)	ω_p (rad/s)	γ (rad/s)
	7.494×10^{15}	7.292×10^{13}
2.644×10^{14}	7.649×10^{15}	6.853×10^{15}
8.842×10^{14}	8.887×10^{15}	2.027×10^{15}
2.426×10^{15}	7.875×10^{15}	3.309×10^{15}
9.251×10^{15}	2.065×10^{16}	9.559×10^{15}

6.4 Simulation results and discussion

The computation domain is shown in Fig. 6-3. The unit cell is a right circular cone. The height of the cone is L and the base diameter is d. The substrate is underneath the cone structure. The cones are placed in the horizontal plane on a $d \times d$ square lattice. A plane source is positioned above the apex of the cone. The reflected flux is calculated in the plane placed between the apex and the source. Note the calculation results do not depend on the exact locations of the two planes, as long as the source is separated from the structure by a sufficient distance to avoid tunneling of the electromagnetic energy.

Since metals have very small penetration depths, no electromagnetic waves will penetrate through a substrate with moderate thickness. In all calculations conducted in this work, the substrate is assumed to be at least a few microns in thickness so that the substrate effectively behaves as a semi-infinite medium. Therefore a perfectly matched boundary is place underneath the base of the cone. On the side-walls, periodic boundary conditions are applied. To ensure numerical and geometry convergence, the Yee cell in the FDTD calculation is 2.5 nm × 2.5 nm× 2.5 nm, which is far less than 1/10 of the shortest wavelength.

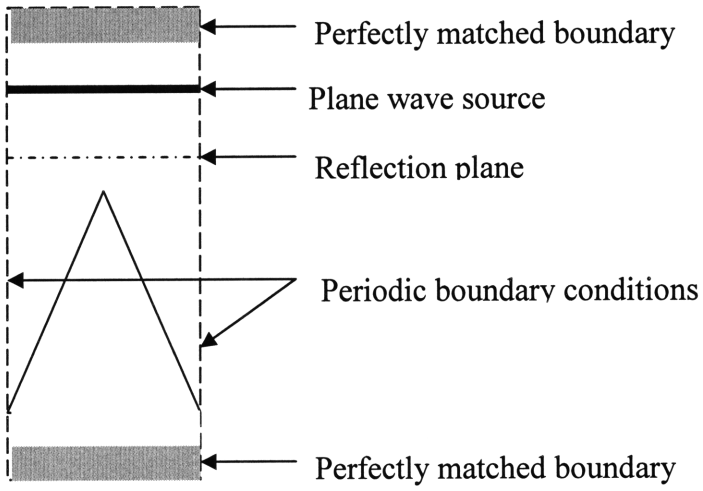

Figure 6-3: Computation domain. Two perfectly matched boundary are placed on the two ends of the domain. On the side-walls, periodic boundary conditions are applied.

6.4.1 Aluminum structures

Figure 6-4 shows the directional spectral absorptance of three aluminum structures at normal incidence. All the structures have the same lattice spacing of 0.1 μm. The figure demonstrates the effect of cone length on the absorptance. The absorptance of flat aluminum surface is presented in the same figure as a reference.

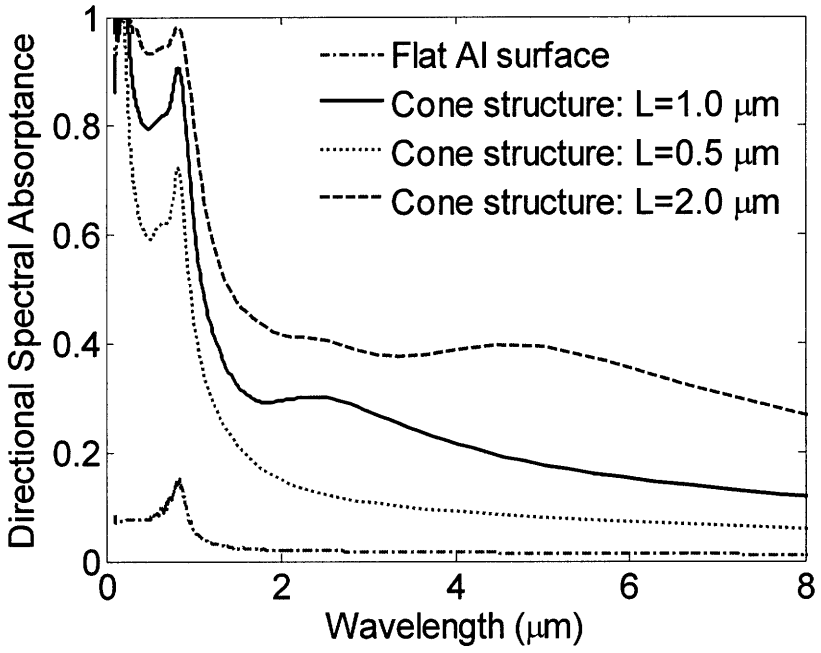

Figure 6-4: The directional spectral absorptance of three aluminum structures at normal incidence. The lattice spacing of all three structures is 0.1 μm. The absorptance of a flat aluminum surface is given as a reference.

The figure clearly shows that the cone structure significantly increases the absorptance of aluminum in the entire spectrum. Effectively, the absorptance of flat aluminum surface is magnified by the cone nanostructures. The absorptance in the visible and near infrared regime is more than 0.95 for the 2 μm cone structure. The absorptance

decreases as the cone becomes shorter. Shorter structures lead to less absorption because the larger length- -to-diameter ratio of theses structures gives more rapid change of the metal volume fraction along the wave propagation direction, which increases the mismatch of the optical index. As seen in the figure, the absorptance in the long-wavelength regime is also enhanced by the cone structure. Longer structures consistently yield more absorption in the entire spectrum.

Figure 6-5 gives the dependence of the absorptance on the base diameter. By decreasing the base diameter of the cone from 0.2 μm to 0.1 μm, the absorptance is enhanced moderately.

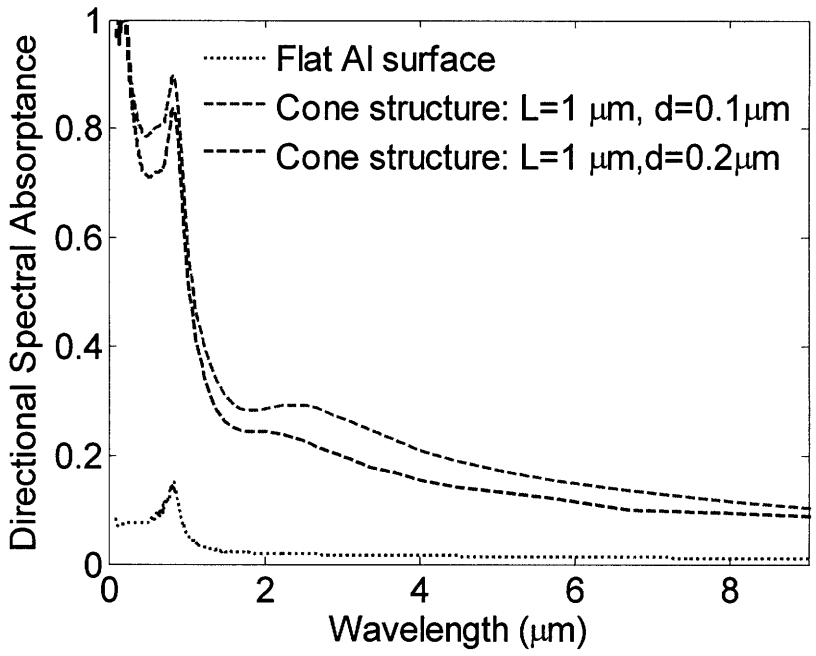

Figure 6-5: The directional spectral absorptance of two aluminum structures at normal incidence. The length of both structures is 1 μm. The absorptance of a flat aluminum surface is given as a reference.

6.4.2 Nickel structures

The results presented in section 6.4.1 show that aluminum cone structures yield reasonably good selectivity. However, the absorptance in the infrared regime is less desirable. The lack of selectivity of the bulk aluminum material, as shown in Fig, 6-1, is to blame for the less than ideal selectivity. To increase absorption of the visible and near-infrared light, cone structures with large aspect ratio have to be used, which inevitably increase absorption in the infrared.

Compared to aluminum, flat nickel surface has higher absorptivity in the short-wavelength regime and reasonably low absorptivity in the long-wavelength regime, which may lead to better spectral selectivity. Figure 6-6 shows the directional spectral absorptance of three nickel structures at normal incidence. Again, the absorptance of the flat nickel surface is presented as a reference.

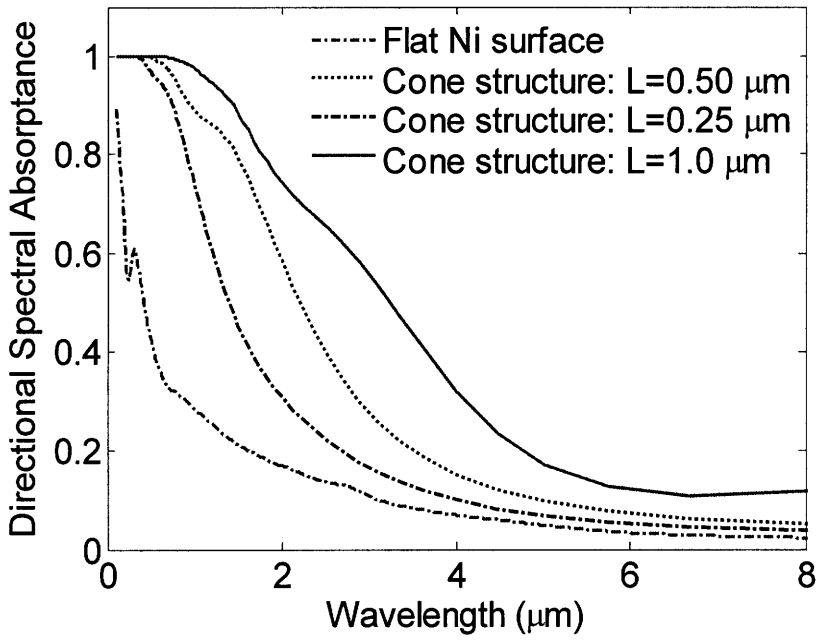

Figure 6-6: The directional spectral absorptance of three nickel structures at normal incidence. The lattice spacing of all three structures is 0.1 μm. The absorptance of a flat nickel surface is given as a reference.

The figure reveals that nickel structures have better spectral selectivity than those made of aluminum. The short-wavelength absorptance is close to 1. Similar trend of the length dependence is also observed in nickel structures. Longer structures lead to more absorption in the entire spectrum. Shorter structures tend to yield better spectral selectivity.

Figure 6-7 shows the absorptance of a different structure: instead of cones, the structure has a unit cell made of nickel rod. As shown in the figure, the rod structure increases absorption similar to the case presented in chapter 4, where silicon nanowire structures dramatically reduce reflection. The absorptance of the rod structure shows enhanced selectivity compared to the flat surface. However, compared to the cone structures, the chosen rod structure has less absorption in the visible, owing to the fact that it lacks a graded profile to minimize reflection.

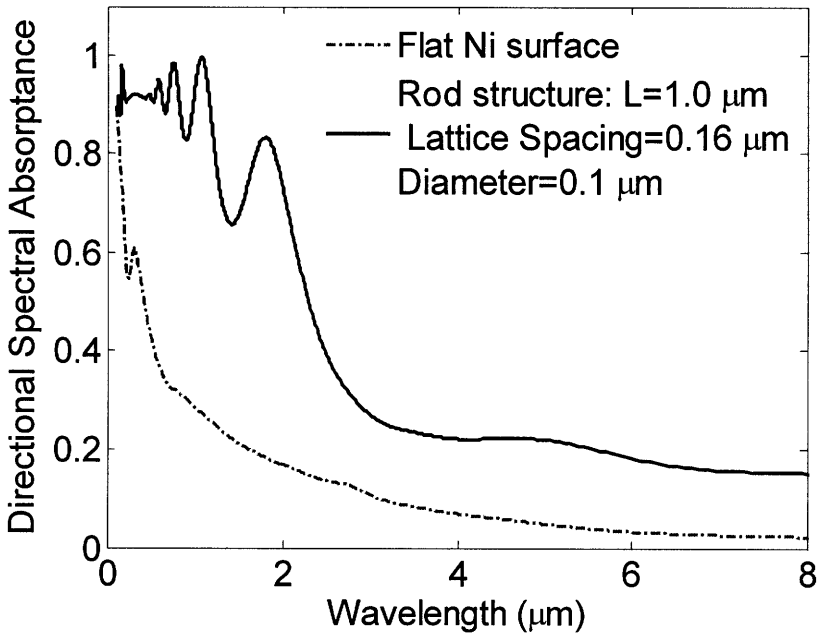

Figure 6-7: The directional spectral absorptance of a nickel rod structures at normal incidence. The lattice spacing 0.16 μm and the diameter of the rod is 0.1 μm. The rod has a length of 1.0 μm.

6.4.3 Copper structures

Among aluminum, nickel and copper, copper has the best selectivity as shown in Fig. 6-1. Figure 6-8 shows the structure-modified absorptance of copper. Again, the directional spectral absorptance of three representative copper structures is plotted in the figure, with the flat copper surface as a reference. Both the cone structures have the same lattice spacing of 0.1 μm. The lengths of the cones are 0.5 μm and 1 μm. Longer cones lead to higher absorption in the entire spectrum, similar to the aluminum and nickel structures. The figure clearly demonstrates that the copper cone structures have the very good selectivity. The absorptance is close to 1 in the short-wavelength regime and sharply decreases to less 0.1 at longer wavelengths. However, the absorptance decreases sharply at around 1 μm, leading to insufficient absorption of the near-infrared radiation. A combination of another material that is capable of absorbing the near-infrared spectrum may solve the problem.

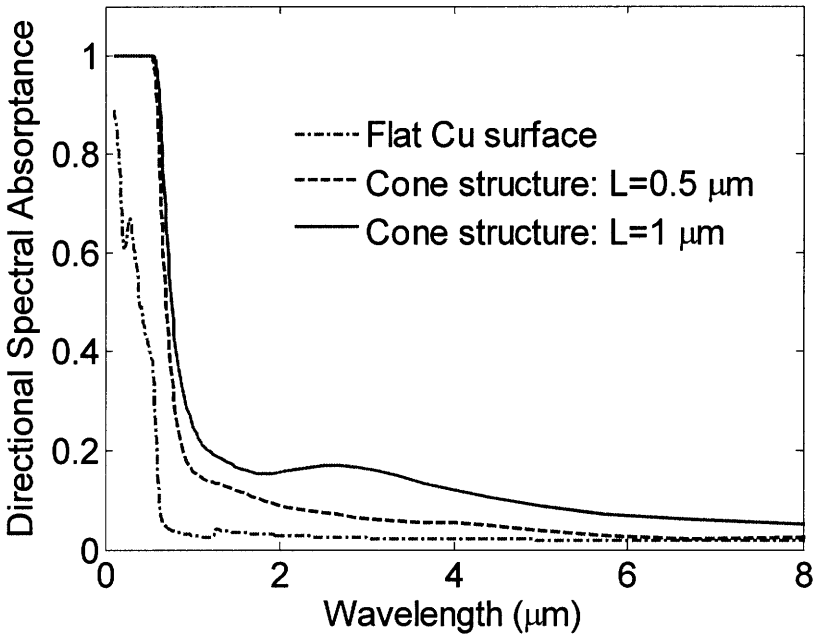

Figure 6-8: The directional spectral absorptance of copper structures at normal incidence. The lattice spacing of both cone structures is 0.1 μm. The absorptance of a flat copper surface is given as a reference.

6.5 Preliminary experimental results

The FDTD simulation shows that metallic cone structures have potentials as solar selective absorbers. Fabrication of these nanostructures has been attempted in our lab. The host material is aluminum, which can be anodized to create submicron periodic pores in aluminum oxide. Anodization is a standard industrial process. It is inexpensive and capable of mass production. The same process is also widely applied in nano/micro fabrications to make metal nanowires [143, 144]. Interested readers should refer to [143, 144] for a more detailed description of the anodization procedures and conditions. Figure 6-9 is a brief illustration of the anodization procedures implemented in this work.

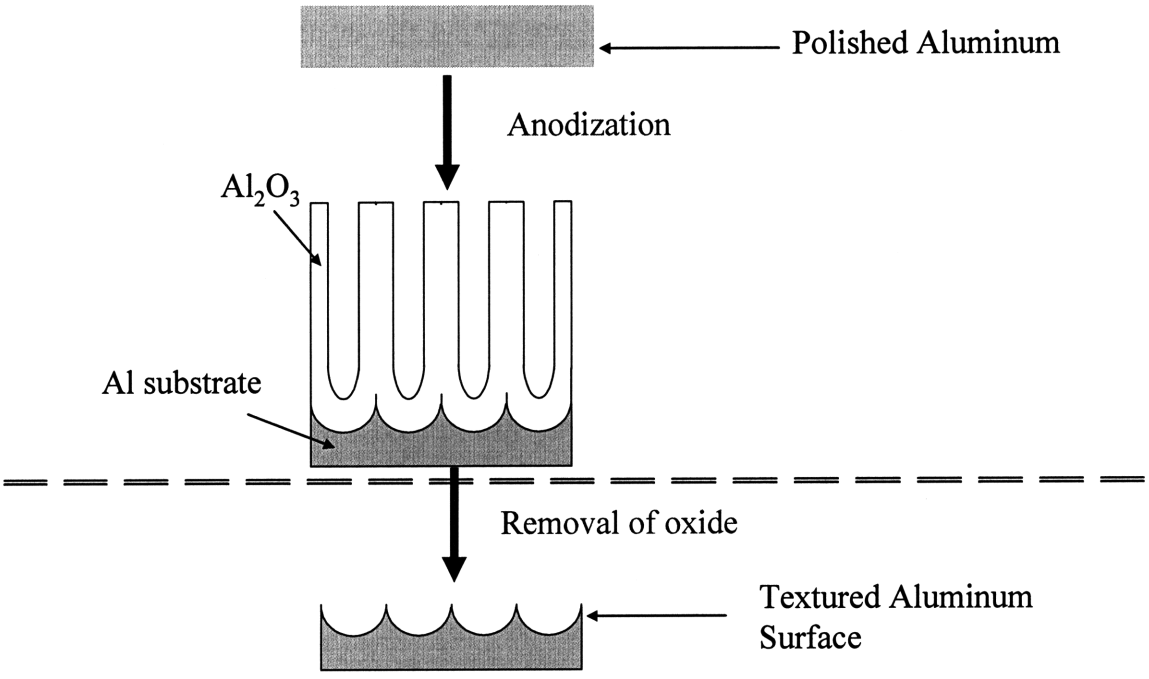

Figure 6-9: The illustration of anodization procedures.

Pure aluminum is first machine polished to obtain a dull mirror finish. The polished aluminum film was annealed at 350°C for 1 hour to relieve the stress in the film before the electrochemical polishing process. The electrolyte solution contains 95 vol% H_3PO_4 (85 wt%, Alfa AESAR), 5 vol% H_2SO_4 (98 vol %, Alfa AESAR) and 20g/l CrO_3 (Alfa AESAR). The electrochemical polishing process is conducted at 85 ± 2 °C and the voltage is 20 V. The process is usually accomplished within 1 minute and produces a shining-mirror-like surface.

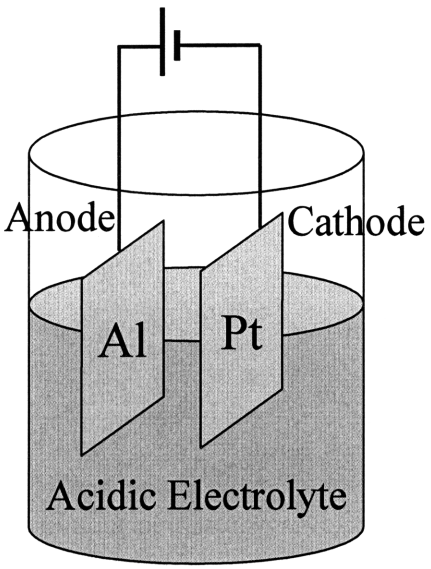

Figure 6-10: Schematic of the anodization apparatus.

The polished aluminum is dipped in a solution of 3.5 vol% H3PO4 (85%, Alfa AESAR) with 45 g/l CrO3 (Alfa AESAR) for about 50 min to remove oxide layer. The aluminum film is then anodized in an acidic electrolyte solution. The set-up of the anodization apparatus is illustrated in Fig. 6-10. The aluminum film is placed in an acidic electrolyte solution as the anode and a platinum film of comparable size is place as cathode. Different acidic solutions are used to create anodic aluminum with different porosities. In this work, both 4 wt% oxalic acid and 2 mol/l H_3PO_4 acid are used.

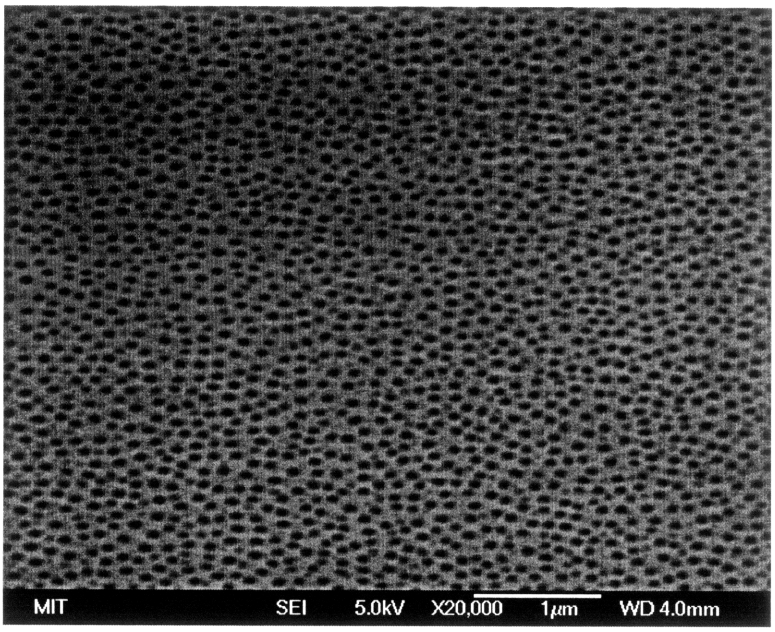

(a)

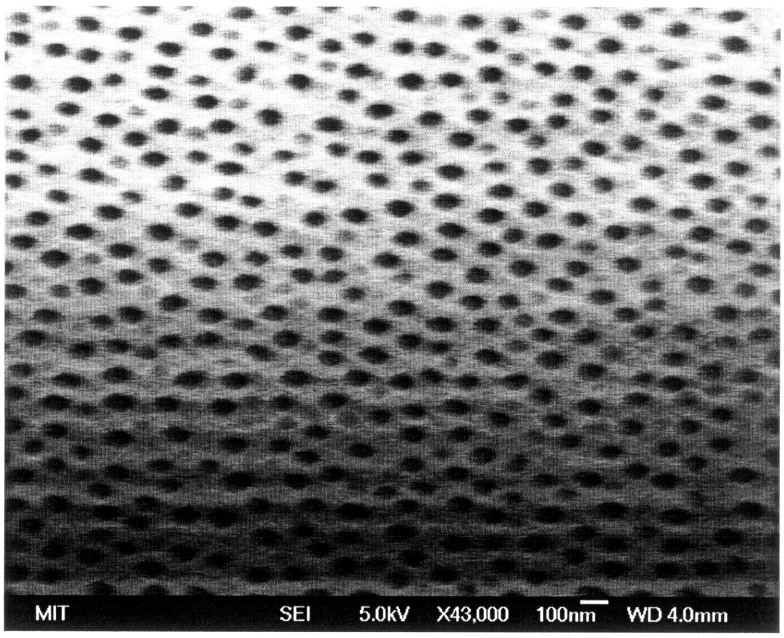

(b)

Figure 6-11: SEM images of the alumina surface. (a) 20,000 magnification. (b) 43,000 magnification.

Figure 6-11(a) and (b) are the scanning electron microscope (SEM) image of the aluminum film after anodization in 4 wt oxalic acid. The voltage is 45V and the anodization took 2 hours. The pore size is around 100 nm as shown in the figure.

The oxide layer can then be removed by dipping into a solution (3.5 wt% H_3PO_4 with 45 g/l CrO_3). The aluminum structure left on the surface has a small top and a large base, which resembles the cone structure. However, the textured aluminum surface is still very reflective, suggesting poor absorption in the visible regime. Longer structures are required to achieve desired spectral selectivity, which may be grown on top of these small aluminum features by electroplating of copper or nickel. Such attempts are to be continued in the nanoengineering group at MIT.

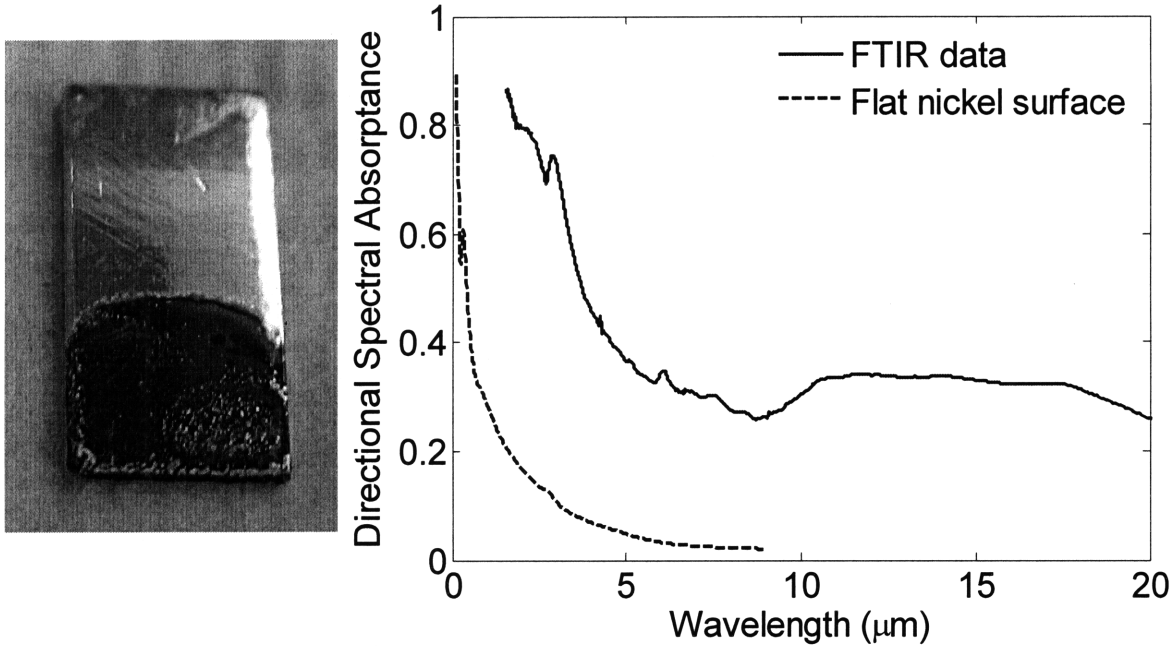

Figure 6-12: (a) A photo of the surface after pigmentation. The dark region contains is nickel-pigmented. (b) The directional spectral absorptance measured by FTIR.

As a proof of concept, the porous anodic aluminum layer is pigmented with nickel by electroplating inside alumina template a process well documented in [126, 131, 145, 146]. The electrolyte solution contains 20 g/l $NiSO_4$, 20 g/l $MgSO_4$, 20 g/l $(NH_4)_2SO_4$ and 20 g/l H_3BO_3. The electroplating is conducted for 15 min with a voltage of 15V at room temperature. Nickel nanowires are formed in the pores [131, 145]. The resulting structure has lower optical density than bulk nickel and increases light absorption. Figure 6-12 (a) is the photo of the aluminum film after the pigmentation. The portion that has been pigmented with nickel has a dark appearance, suggesting high absorptance in the visible. Figure 6-12 (b) is the Fourier transform infrared spectroscopy (FTIR) measurement of the surface, where the reflectance is measured at the normal direction and has been converted to absorptance. The absorptance is close to 0.9 at 1 μm and drops to 0.35 at 6 μm. In comparison to the calculated absorptance of a flat nickel surface, the optical absorption in the visible and near-infrared regime increases significantly, whereas the absorptance in the long-wavelength regime is too high. Nevertheless, the pigmented surface shows reasonably good selectivity as compared to the flat nickel surface. Improvement of the selectivity is well within reach by carefully controlling the depth and porosity of the pores, which is worth more attention for further investigation.

6.6 Summary of findings

This chapter presents numerical and experimental studies on optical absorption in periodic metal structures. The unit cell of these structures consists of submicron metallic cones or rods which serve to minimize reflection and enhance absorption. To study the interaction of light with these metallic photonic structures, the FDTD method is used to calculate the absorptance of different structures. The effects of structure length and lattice spacing have been studied for aluminum, nickel and copper. The numerical simulation shows that these metallic structures drastically change the optical properties of bulk metal.

Good spectrum selectivity is found for all three metals, where absorptance is high in the solar spectrum and emittance is low in infrared. Preliminary experimental studies are carried out to fabricate these metallic photonic structures. As a proof of concept, anodic aluminum surface is pigmented with nickel to form nickel nanowires in the pores. The resulting structure shows reasonably good spectral selectivity.

Further study of the selective absorber surfaces is worth attention. More systematic calculations can be conducted to identify optimized structures for specific applications. Binary or multi-component systems that contain more than one specie of metal can also be explored to combine the desirable optical properties of different metals. The theoretical investigation can be followed by experimental study, on both porous anodic aluminum and textured aluminum. The focus should be on identifying anodization and electroplating conditions to fabricate the structures optimized in numerical simulations.

Chapter 7

Summary and Outlook

7.1 Summary

Photons are the energy carriers in solar irradiance and thermal radiation. This dissertation addresses the issue of photon management for photovoltaics, thermophotovoltaic (TPV) and solar thermal applications. The first half of the work is focused on thermal emission and photon transport in thermophotovoltaic systems and the second half is devoted to optical absorption in solar spectrum. The common theoretical background employed throughout this work is the electromagnetic theory. All the phenomena that have been studied in this work have length scale either comparable or smaller than the wavelength of interest, where interference, diffraction and near-field effects of electromagnetic waves become important.

Chapter 2 and 3 are focused on thermophotovoltaic systems. Chapter 2 studies photon transport in multilayer structures. Two methods, the wave optics and the ray tracing method, are discussed. Wave interference effects are fully taken into consideration by using wave optics. In comparison, the ray tracing method, which treats photons as particles and neglects phase information of electromagnetic waves, is also employed to study transport of blackbody radiation through multilayer structures. The study shows that for multilayer systems containing a small number of layers (up to four) both methods are valid when the layer thickness is larger than the coherence length of the blackbody irradiance spectrum. The finding confirms existing theory for single layered system. The unique contribution of this work is that it reveals that these two methods

generally lead to different results structures containing a large number of layers, regardless of the layer thickness. The results imply that for one-dimensional multilayer thin film structures with perfectly aligned interfaces, there may not be an incoherence regime in which the ray tracing method can be applied. The effect of localization on photon transport is also studied by randomly varying the layer thickness. For random structures, the two methods also lead to different results usually. The general conclusion is that wave optics should always be used for studying photon transport through multilayer systems containing a large number of layers. The contents in chapter can also be applied in solar PV applications where multilayer structures are used as spectral filters.

The work then shifts to thermal emission in chapter 3, where the near-field effects and radiative transport between two parallel glass plates are studied. Direct calculation of the near-field radiative heat flux is performed by using dyadic Green's function and the fluctuation-dissipation theorem. The calculations indentify the conditions with which the near-field effects become pronounced. It is found that the radiative heat flux is dominated by the contribution from surface phonon polaritions when the gap between the plates is around 1 μm. The theory has been tested experimentally by measuring the radiative heat flux between two glass optical flats. The measured radiative heat flux exceeds the blackbody radiation for more than 35% in the entire temperature range, and agrees reasonably well with the calculation results.

Photons absorptions in solar spectrum are discussed in the rest of the dissertation for solar power applications. Chapter 4 and chapter 5 address photon absorption in silicon structures. Optical absorption in silicon nanowires are studied in chapter 4 by solving Maxwell's equations using a 3-dimensional transfer matrix method. A new discretization algorithm is developed in the same chapter for better numerical stability. The study identifies a unique optical property found only in nanowire structures: very low optical reflectance over a broad spectrum. The low optical reflectance has great potential for solar PV applications and eliminates the need of specially designed anti-reflection coatings. The study reveals that the nanowire structures do have disadvantages: photon

absorption in long-wavelength regime is inadequate. Longer wires are generally required to compensate low absorption in the near-bandgap photons. Chapter 5 follows to address near-bandgap absorption in silicon. Instead of increasing the optical path of photons for more absorption, this chapter studies local field enhanced absorption induced by surface plasmons. An extended Mie scattering formulism is used to calculate the optical absorption around spherical silver particles that are embedded in silicon. With the diameters of particles ranging from nanometers to sub-microns, the effects of scattering of electrons on boundaries are considered and correspondingly the optical constant of silver is modified to reflect the effects. It is found that local field enhancement by surface plasmon can lead to 50 times more absorption near the bandgap of silicon. An analytical model is developed to study the concentration effects of the surface plasmon field. It is shown that the net absorption gain reaches maximum when the spherical shell surrounding the particle has an outer diameter of 1.26 times of the particle diameter. In the end, one possible problem of utilizing surface plasmon for absorption enhancement is also pointed out: in certain spectral range the absorption loss in the metal particle may exceed the absorption in silicon, which needs to be addressed with novel design such as core-shell structures.

Chapter 4 and 5 are dealing with direct photo-to-electro energy conversion. Any photons with energies below the bandgaps of the photovoltaic cells cannot be used to generate electricity. The matching of solar spectrum with solar cells imposes great technical challenges, which is partially discussed in chapter 1. There is a different approach: selective absorber for solar thermal power generation. Instead of utilizing a portion of the solar spectrum, solar thermal technique uses the whole solar spectrum to heat up a heat engine to generate electricity. Chapter 6 presents numerical and experimental studies on optical absorption in periodic metal cone structures. The unit cell of these structures consists of metal cones which is submicron in sizes. To study the interaction of light with these metallic photonic structures, the finite-difference time-domain method is used to calculate the absorptance of different nano-structures. The

numerical simulation shows that these metallic structures drastically change the optical properties of bulk metal. Spectrum selectivity is found for these structures, where absorptance is high in the solar spectrum and emittance is low in infrared. Preliminary experimental studies are carried out to fabricate these metallic photonic structures. Anodization process is used to create submicron pores in aluminum. The anodic aluminum serves two purposes: (1) a template for pigmentation of nickel and copper. (2) the textured aluminum structure after removing the oxide can be used as a seeding site to plate copper. Process (1) has been attempted and lead to reasonably good spectral selectivity.

7.2 Possible extension of the work

This dissertation only discusses a few topics related to photon transport and absorption for alternative energy applications. There are far more issues that can be addressed within the framework established in this work. A few examples are listed as follow.

In this work, the localization effects on photon transport through dielectric multilayer structures are studied. It can be extended to the case where the multilayer structures consist of lossy materials. The localization of photons can lead to enhanced absorption in particular spectral range and depressed absorption in others. The multilayer structure thus can be exploited as thermal emitter that has capability of spectral control. The combined effect of localization and near-field radiation is another topic that may have both theoretical and practical values. Additional studies on near-field radiation can be explored with the experimental setup described in chapter 3, particularly for surface wave with longer wavelengths. For example, the effects of long wavelength surface plasmons on radiative heat transfer can be tested with doped silicon, whose plasmon frequency can be tuned by the dopant concentration. Radiative heat transfer between photonic structures, instead of planar structures, can also be studied. The algorithm for

direct calculation of thermal emission from 2-dimensional and 3-dimensional photonic structures is also yet to be developed.

Chapters 4 to 6 present three different nanostructures for solar power applications. Many more structures can be studied with the transfer matrix method and the Mie scattering method. Optical absorption in dye-sensitized solar cells (DSCs) is an interesting topic awaiting for exploration. In DSCs, a monolayer of dye molecules is coated on high bandgap materials such as TiO_2 or SnO. Light absorption in dye-sensitized nanowires can be simulated with the transfer matrix method. The Mie scattering approach can be extended for multi-scatter systems to study photon transport through dye-sensitized particles. Note that the dielectric function of the monolayer is different from the bulk, the modeling of which is itself an important task to accomplish, too.

Further investigation of the selective absorber surfaces is worth attention. In chapter 6, a limited number of simulations were performed for single-component systems that contain only single metal specie. The simulation results presented in the chapter show that the absorption in the long wavelength regime needs to be suppressed for optimization purpose. More systematic calculations can be conducted to identify optimized structures for specific applications. Binary or multi-component systems that contain more than one specie of metal can also be explored to combine the desirable optical properties of different metals. The theoretical investigation can be followed by experimental study, on both porous anodic aluminum and textured aluminum. The focus should be on identifying anodization and electroplating conditions to fabricate the structures optimized in numerical simulations.

Bibliography

[1] Coutts, T. J., 1999, "A Review of Progress in Thermophotovoltaic Generation of Electricity," Renewable & Sustainable Energy Reviews, **3**, pp. 77-184.

[2] Modest, M. F., 2003, *Radiative Heat Transfer*, Academic Press.

[3] Green, M. A., 2001, "Third Generation Photovoltaics: Ultra-High Conversion Efficiency at Low Cost," Progress in Photovoltaics Research and Applications, **9**, pp. 123-135.

[4] Green, M. A., 2004, "Recent Developments in Photovoltaics," Solar Energy, **76**, pp. 3-8.

[5] Planck, M., 1901, "On the Law of Distribution of Energy in the Normal Spectrum," Annalen der Physik, **4**, pp. 553 ff.

[6] Chen, G., and Tien, C. L., 1992, "Partial Coherence Theory of Thin Film Radiative Properties," Journal of Heat Transfer, **114**, pp. 636-643.

[7] Richter, K., Chen, C., and Tien, C. L., 1993, "Partial Coherence Theory of Multilayer Thin-Film Optical Properties," Proceedings of SPIE, **284**, pp. 1897-1903.

[8] Mehta, C. L., 1963, "Coherence-Time and Effective Bandwidth of Blackbody Radiation," Il Nuovo Cimento, **28**, pp. 401-408.

[9] Planck, M., 1988, *The Theory of Heat Radiation*, American Institute of Physics.

[10] Incropera, F. P., and Dewitt, D. P., 1996, *Fundamentals of Heat and Mass Transfer*, Hemisphere Publishing.

[11] Lienhard Iv, J. H., and Lienhard V, J. H., 2003, *A Heat Transfer Textbook*, Phlogiston Press.

[12] Couture, L., 2000, *Statistical Thermodynamics and Properties of Matter*, CRC.

[13] Agarwal, G. S., 1975, "Quantum Electrodynamics in the Presence of Dielectrics and Conductors. I. Electromagnetic-Field Response Functions and Black-Body Fluctuations in Finite Geometries," Physical Review A, **11**, pp. 230-242.

[14] Joulain, K., Carminati, R., Mulet, J. P., and Greffet, J. J., 2003, "Definition and Measurement of the Local Density of Electromagnetic States Close to an Interface," Physical Review B, **68**, pp. 245405.

[15] Joulain, K., Mulet, J. P., Marquier, F., Carminati, R., and Greffet, J. J., 2005, "Surface Electromagnetic Waves Thermally Excited: Radiative Heat Transfer, Coherence Properties and Casimir Forces Revisited in the Near Field," Surface Science Reports, **57**, pp. 59-112.

[16] Rytov, S. M., 1959, "Theory of Electric Fluctuations and Thermal Radiation," Technical Report No. Technical Report No. AFCRC-TR-59-162, Air Force Cambridge Research Center, Bedford, MA.

[17] Rytov, S. M., Tatarskii, V. I., and Kravtsov, Y., 1987, *Principles of Statistical Radiophysics*, Springer-Verlag, Berlin.

[18] Polder, D., and Van Hove, M., 1971, "Theory of Radiative Heat Transfer between Closely Spaced Bodies," Physical Review B, **4**, pp. 3303-3314.

[19] Tsang, L., Kong, J. A., Ding, K. H., and Ao, C. O., 2001, *Scattering of Electromagnetic Waves*, Wiley.

[20] Mulet, J. P., Joulain, K., Carminati, R., and Greffet, J. J., 2002, "Enhanced Radiative Heat Transfer at Nanometric Distances," Microscale Thermophysical Engineering, **6**, pp. 209-222.

[21] Narayanaswamy, A., and Chen, G., 2003, "Surface Modes for Near Field Thermophotovoltaics," Applied Physics Letters, **82**, pp. 3544.

[22] Fu, C. J., and Zhang, Z. M., 2006, "Nanoscale Radiation Heat Transfer for Silicon at Different Doping Levels," International Journal of Heat and Mass Transfer, **49**, pp. 1703-1718.

[23] Narayanaswamy, A., and Chen, G., 2005, "Thermal Radiation in 1d Photonic Crystals," Journal of Quantitative Spectroscopy and Radiative Transfer, **93**, pp. 175-183.

[24] Narayanaswamy, A., and Chen, G., 2004, "Thermal Emission Control with One-Dimensional Metallodielectric Photonic Crystals," Physical Review B, **70**, pp. 125101.

[25] Chapuis, P. O., Volz, S., Henkel, C., Joulain, K., and Greffet, J. J., 2008, "Effects of Spatial Dispersion in Near-Field Radiative Heat Transfer between Two Parallel Metallic Surfaces," Physical Review B, **77**, pp. 35431.

[26] Domoto, G. A., Boehm, R. F., and Tien, C. L., 1970, "Experimental Investigation of Radiative Transfer between Metallic Surfaces at Cryogenic Temperatures," J. Heat Transfer, **92**, pp. 412–417.

[27] Hargreaves, C. M., 1973, "Radiative Transfer between Closely Spaced Bodies," Philips Research Report, Supplement, **5**, pp. 1-18.

[28] Xu, J. B., Läuger, K., Möller, R., Dransfeld, K., and Wilson, I. H., 1994, "Heat Transfer between Two Metallic Surfaces at Small Distances," Journal of Applied Physics, **76**, pp. 7209-7216.

[29] Kittel, A., Müller-Hirsch, W., Parisi, J., Biehs, S. A., Reddig, D., and Holthaus, M., 2005, "Near-Field Heat Transfer in a Scanning Thermal Microscope," Physical Review Letters, **95**, pp. 224301.

[30] Laroche, M., Carminati, R., and Greffet, J. J., 2006, "Near-Field Thermophotovoltaic Energy Conversion," Journal of Applied Physics, **100**, pp. 063704.

[31] Dimatteo, R. S., Greiff, P., Finberg, S. L., Young-Waithe, K. A., Choy, H. K. H., Masaki, M. M., and Fonstad, C. G., 2001, "Enhanced Photogeneration of Carriers in a Semiconductor Via Coupling across a Nonisothermal Nanoscale Vacuum Gap," Applied Physics Letters, **79**, pp. 1894.

[32] Shockley, W., and Queisser, H. J., 1961, "Detailed Balance Limit of Efficiency of P-N Junction Solar Cells," Journal of Applied Physics, **32**, pp. 510-519.

[33] Thekaekara, M. P., 1973, "Solar Energy Outside the Earth's Atmosphere," Solar Energy, **14**, pp. 109-127.

[34] Air Mass 1.5 Spectra, American Society for Testing and Materials, http://rredc.nreal.gov/solar/spectra/am1.5/

[35] Bird, R. E., and Hulstrom, R. L., 1982, *Terrestrial Solar Spectral Data Sets*, SERI/TR-642-1149, Solar Energy Research Institute, Golden, CO.

[36] Gueymard, C. A., 2004, "The Sun's Total and Spectral Irradiance for Solar Energy Applications and Solar Radiation Models," Solar Energy, **76**, pp. 423-453.

[37] Riordan, C., and Hulstrom, R., 1990, "What Is an Air Mass 1.5 Spectrum?," Photovoltaic Specialists Conference, 1990., Conference Record of the Twenty First IEEE, eds., Kissimmee, FL, USA, pp. 1085-1088.

[38] Gueymard, C. A., 2001, "Parameterized Transmittance Model for Direct Beam and Circumsolar Spectral Irradiance," Solar Energy, **71**, pp. 325-346.

[39] Smil, V., 2008, *Energy in Nature and Society: General Energetics of Complex Systems*, the MIT Press, Cambridge, MA.

[40] Green, M. A., 2007, "Thin-Film Solar Cells: Review of Materials, Technologies and Commercial Status," Journal of Materials Science: Materials in Electronics, **18**, pp. 15-19.

[41] Brabec, C. J., Sariciftci, N. S., and Hummelen, J. C., 2001, "Plastic Solar Cells," Advanced Functional Materials, **11**, pp. 15-26.

[42] Fahrenbruch, A. L., and Bube, R. H., 1983, *Fundamentals of Solar Cells*, Academic Press, New York.

[43] Koynov, S., Brandt, M. S., and Stutzmann, M., 2006, "Black Nonreflecting Silicon Surfaces for Solar Cells," Applied Physics Letters, **88**, pp. 203107.

[44] Yamamoto, K., 1999, "Very Thin Film Crystalline Silicon Solar Cells on Glass Substratefabricated at Low Temperature," Electron Devices, IEEE Transactions on, **46**, pp. 2041-2047.

[45] Green, M. A., 1999, "Two New Efficient Crystalline Silicon Light-Trapping Textures," Progress in photovoltaics, **7**, pp. 317-320.

[46] Rowlands, S. F., Livingstone, J., and Lund, C. P., 2004, "Optical Modelling of Thin Film Solar Cells with Textured Interfaces Using the Effective Medium Approximation," Solar Energy, **76**, pp. 301-307.

[47] Cotter, J. E., 1998, "Optical Intensity of Light in Layers of Silicon with Rear Diffuse Reflectors," Journal of Applied Physics, **84**, pp. 618.

[48] Zhao, J., Wang, A., and Green, M. A., 1999, "24. 5% Efficiency Silicon Pert Cells on Mcz Substrates and 24. 7% Efficiency Perl Cells on Fz Substrates," Progress in photovoltaics, **7**, pp. 471-474.

[49] Pillai, S., Catchpole, K. R., Trupke, T., and Green, M. A., 2007, "Surface Plasmon Enhanced Silicon Solar Cells," Journal of Applied Physics, **101**, pp. 093105.

[50] Derkacs, D., Lim, S. H., Matheu, P., Mar, W., and Yu, E. T., 2006, "Improved Performance of Amorphous Silicon Solar Cells Via Scattering from Surface Plasmon Polaritons in Nearby Metallic Nanoparticles," Applied Physics Letters, **89**, pp. 093103.

[51] Goswami, D. Y., 1998, "Solar Thermal Power Technology: Present Status and Ideas for the Future," Energy Sources, Part A: Recovery, Utilization, and Environmental Effects, **20**, pp. 137-145.

[52] Mills, D., 2004, "Advances in Solar Thermal Electricity Technology," Solar Energy, **76**, pp. 19-31.

[53] Kennedy, C. E., 2002, "Review of Mid-to High-Temperature Solar Selective Absorber Materials," Technical Report No. NREL/TP-520-31267, National Renewable Energy Laboratory, Golden, CO.

[54] Bohren, C. F., and Huffman, D. R., 1983, *Absorption and Scattering of Light by Small Particles*, Wiley, New York.

[55] Taflove, A., and Hagness, S. C., 1995, *Computational Electrodynamics: The Finite-Difference Time-Domain Method*, Artech House, Boston.

[56] Born, M., and Wolf, E., 1980, *Principles of Optics*, Pergamon Press, New York.

[57] Zhang, Z. M., 1994, "Optical Properties of Layered Structures for Partially Coherent Radiation," Proc. of the 10 thInternational Heat Transfer Conference, G. F. Hewitt, eds., Brighton, UK, 2, pp. 177-182.

[58] Wong, P. Y., Hess, C. K., and Miaoulis, I. N., 1992, "Thermal Radiation Modeling in Multilayer Thin Film Structures," International Journal of Heat and Mass Transfer, **35**, pp. 3313-3321.

[59] Mehta, C. L., and Wolf, E., 1964, "Coherence Properties of Blackbody Radiation. I. Correlation Tensors of the Classic Field," Physical Review, **134**, pp. A1143-A1149.

[60] Mehta, C. L., and Wolf, E., 1964, "Coherence Properties of Blackbody Radiation. Ii. Correlation Tensors of the Quantized Field," Physical Review, **134**, pp. A1149-A1153.

[61] Mehta, C. L., and Wolf, E., 1964, "Coherence Properties of Blackbody Radiation. Iii. Cross-Spectral Tensors," Physical Review, **161**, pp. 1328-1334.

[62] Kano, Y., and Wolf, E., 1962, "Temporal Coherence of Black Body Radiation," Proceedings of the Physical Society, **80**, pp. 1273-1276.

[63] Chen, G., 1999, "Phonon Wave Heat Conduction in Thin Films and Superlattices," Journal of Heat Transfer, **121**, pp. 945-951.

[64] Anderson, P. W., 1958, "Absence of Diffusion in Certain Random Lattices," Physical Review, **109**, pp. 1492-1505.

[65] Kotulski, Z., 1993, "Wave Propagation in Randomly Stratified Media and Anderson Localization," Proc. of Euromech Colloquim: Chaos and Noise in Dynamical Systems, T. Kapitaniak, et al., eds., Spala, Poland, 308, pp. 138-146.

[66] John, S., 1990, "The Localization of Waves in Disordered Media," *in Scattering and Localization of Classical Waves in Random Media*, P. Sheng, ed., World Scientific, New Jersey.

[67] Albada, M. P., Mark, M. P., and Lagendijk, A., 1990, "Experiments on Weak Localization of Light and Their Interpretation," *in Scattering and Localization of Classical Waves in Random Media*, P. Sheng, ed., World Scientific, New Jersey.

[68] Sheng, P., 1995, *Introduction to Wave Scattering, Localization, and Mesoscopic Phenomena*, Academic, New York.

[69] Sheng, P., White, B., Zhang, Z. Q., and Papanicolaou, G., 1986, "Minimum Wave-Localization Length in a One-Dimensional Random Medium," Physical Review B, **34**, pp. 4757-4761.

[70] Gredeskul, S. A., and Freilikher, V. D., 1990, "Localization and Wave Propagation in Randomly Layered Media," Physics-Uspekhi, **33**, pp. 134-146.

[71] Figotin, A., and Klein, A., 1998, "Localization of Light in Lossless Inhomogeneous Dielectrics," Journal of the Optical Society of America A, **15**, pp. 1423-1435.

[72] Chubb, D. L., and Lowe, R. A., 1993, "Thin-Film Selective Emitter," Journal of Applied Physics, **74**, pp. 5687-5698.

[73] Sakoda, K., Sasada, M., Fukushima, T., Yamanaka, A., Kawai, N., and Inoue, K., 1999, "Detailed Analysis of Transmission Spectra and Bragg-Reflection Spectra of a Two-Dimensional Photonic Crystal with a Lattice Constant of 1.15 μM," Journal of the Optical Society of America B, **16**, pp. 361-365.

[74] Fleming, J. G., Lin, S. Y., El-Kady, I., Biswas, R., and Ho, K. M., 2002, "All-Metallic Three-Dimensional Photonic Crystals with a Large Infrared Bandgap," Nature, **417**, pp. 52-55.

[75] Schmidt, R. N., and Park, K. C., 1965, "High-Temperature Space-Stable Selective Solar Absorber Coatings," Applied Optics, **4**, pp. 917.

[76] Siegel, R., and Howell, J. R., 1992, *Thermal Radiation Heat Transfer*, Hemisphere, Washington.

[77] Ziegler, K., 2003, "Localization of Electromagnetic Waves in Random Media," Journal of Quantitative Spectroscopy and Radiative Transfer, **79**, pp. 1189-1198.

[78] Sigalas, M. M., Soukoulis, C. M., Chan, C. T., and Turner, D., 1996, "Localization of Electromagnetic Waves in Two-Dimensional Disordered Systems," Physical Review B, **53**, pp. 8340-8348.

[79] Evans, G. A., and Webster, J. R., 1999, "A Comparison of Some Methods for the Evaluation of Highly Oscillatory Integrals," Journal of Computational and Applied Mathematics, **112**, pp. 55-69.

[80] Hoffman, J. D., 1992, *Numerical Methods for Scientists and Engineers*, McGraw-Hill, New York.

[81] Escande, D. F., and Souillard, B., 1984, "Localization of Waves in a Fluctuating Plasma," Physical Review Letters, **52**, pp. 1296-1299.

[82] García-Martín, A., Sáenz, J. J., and Nieto-Vesperinas, M., 2000, "Spatial Field Distributions in the Transition from Ballistic to Diffusive Transport in Randomly Corrugated Waveguides," Physical Review Letters, **84**, pp. 3578-3581.

[83] Froufe-Pérez, L. S., García-Mochales, P., Serena, P. A., Mello, P. A., and Sáenz, J. J., 2002, "Conductance Distributions in Quasi-One-Dimensional Disordered Wires," Physical Review Letters, **89**, pp. 246403.

[84] Pendry, J. B., 1999, "Radiative Exchange of Heat between Nanostructures," Journal of Physics: Condensed Matter, **11**, pp. 6621-6633.

[85] Cravalho, E. G., Tien, C. L., and Caren, R. P., 1967, "Effect of Small Spacings on Radiative Transfer between Two Dielectrics," J. Heat Transfer, **89**, pp. 351-358.

[86] Narayanaswamy, A., 2007, "Investigation of Nanoscale Thermal Radiation: Theory and Experiments," Ph.D. thesis, Massachusetts Institute of Technology, Cambridge, MA.

[87] Kong, J. A., 2000, *Electromagnetic Wave Theory*, EMW, Cambridge.

[88] Palik, E. D., 1985, *Handbook of Optical Constants of Solids*, Academic Press.

[89] Pezzotti, G., Kamada, I., and Miki, S., 2000, "Thermal Conductivity of Aln/Polystyrene Interpenetrating Networks," Journal of the European Ceramic Society, **20**, pp. 1197-1203.

[90] Springer, G. S., 1971, "Heat Transfer in Rarefied Gases," *in Advances in Heat Transfer*, T. F. Irvine, et al., ed., Academic, New York.

[91] Touloukian, Y. S., Liley, P. E., and Saxena, S. C., 1970, *Thermophysical Properties of Matter*, IFI/Plenum Press, New York.

[92] Huynh, W. U., Dittmer, J. J., and Alivisatos, A. P., 2002,

[93] Law, M., Greene, L. E., Johnson, J. C., Saykally, R., and Yang, P., 2005, "Nanowire Dye-Sensitized Solar Cells," Nature Materials, **4**, pp. 455-459.

[94] Wang, Y., Kempa, K., Kimball, B., Carlson, J. B., Benham, G., Li, W. Z., Kempa, T., Rybczynski, J., Herczynski, A., and Ren, Z. F., 2004, "Receiving and Transmitting Light-Like Radio Waves: Antenna Effect in Arrays of Aligned Carbon Nanotubes," Applied Physics Letters, **85**, pp. 2607.

[95] Rybczynski, J., Kempa, K., Wang, Y., Ren, Z. F., Carlson, J. B., Kimball, B. R., and Benham, G., 2006, "Visible Light Diffraction Studies on Periodically Aligned Arrays of Carbon Nanotubes: Experimental and Theoretical Comparison," Applied Physics Letters, **88**, pp. 203122.

[96] Kayes, B. M., Atwater, H. A., and Lewis, N. S., 2005, "Comparison of the Device Physics Principles of Planar and Radial Pn Junction Nanorod Solar Cells," Journal of Applied Physics, **97**, pp. 114302.

[97] Tian, B., Zheng, X., Kempa, T. J., Fang, Y., Yu, N., Yu, G., Huang, J., and Lieber, C. M., 2007, "Coaxial Silicon Nanowires as Solar Cells and Nanoelectronic Power Sources," Nature, **449**, pp. 885-889.

[98] Kelzenberg, M. D., Turner-Evans, D. B., Kayes, B. M., Filler, M. A., Putnam, M. C., Lewis, N. S., and Atwater, H. A., 2008, "Photovoltaic Measurements in Single-Nanowire Silicon Solar Cells," Nano Lett, **8**, pp. 710-714.

[99] Lauhon, L. J., Gudiksen, M. S., Wang, D., and Lieber, C. M., 2002, "Epitaxial Core-Shell and Core-Multishell Nanowire Heterostructures," Nature, **420**, pp. 57-61.

[100] Law, M., Goldberger, J., and Yang, P., 2004, "Semiconductor Nanowires and Nanotubes," Annual Review of Materials Research, **34**, pp. 83-122.

[101] Pendry, J. B., 1994, "Photonic Band Structures," Journal of Modern Optics, **41**, pp. 209-229.

[102] Bell, P. M., Pendry, J. B., Moreno, L. M., and Ward, A. J., 1995, "A Program for Calculating Photonic Band Structures and Transmission Coefficients of Complex Structures," Computer Physics Communications, **85**, pp. 306-322.

[103] Yee, K. S., 1966, "Numerical Solution of Initial Boundary Value Problems Involving Maxwell ⁄ s Equations in Isotropic Media," IEEE Transactions on Antennas and Propagation, **14**, pp. 302-307.

[104] Petit, R., 1980, *Electromagnetic Theory of Gratings*, Springer-Verlag, Berlin.

[105] Jellison Jr, G. E., Modine, F. A., White, C. W., Wood, R. F., and Young, R. T., 1981, "Optical Properties of Heavily Doped Silicon between 1.5 and 4.1 Ev," Physical Review Letters, **46**, pp. 1414-1417.

[106] Brendel, R., Bergmann, R. B., Lölgen, P., Wolf, M., and Werner, J. H., 1997, "Ultrathin Crystalline Silicon Solar Cells on Glass Substrates," Applied Physics Letters, **70**, pp. 390.

[107] Yamamoto, K., Nakajima, A., Yoshimi, M., Sawada, T., Fukuda, S., Suezaki, T., Ichikawa, M., Koi, Y., Goto, M., and Meguro, T., 2004, "A High Efficiency Thin Film Silicon Solar Cell and Module," Solar Energy, **77**, pp. 939-949.

[108] Kattawar, G. W., and Eisner, M., 1970, "Radiation from a Homogeneous Isothermal Sphere," Applied Optics, **9**, pp. 2685.

[109] Krc, J., Zeman, M., Smole, F., and Topic, M., 2004, "Optical Modelling of Thin-Film Silicon Solar Cells Deposited on Textured Substrates," Thin Solid Films, **451**, pp. 298-302.

[110] Rand, B. P., Peumans, P., and Forrest, S. R., 2004, "Long-Range Absorption Enhancement in Organic Tandem Thin-Film Solar Cells Containing Silver Nanoclusters," Journal of Applied Physics, **96**, pp. 7519.

[111] Zhao, G., Kozuka, H., and Yoko, T., 1996, "Sol-Gel Preparation and Photoelectrochemical Properties of Tio2 Films Containing Au and Ag Metal Particles," Thin Solid Films, **277**, pp. 147-154.

[112] Kittel, C., 1996, *Introduction to Solid State Physics*, Wiley, New York.

[113] Raether, H., 1988, *Surface Plasmons on Smooth and Rough Surfaces and on Gratings*, Springer-Verlag, Berlin.

[114] Chang, R. K., and Furtak, T. E., 1982, *Surface Enhanced Raman Scattering*, Plenum Press, New York.

[115] Catchpole, K. R., and Pillai, S., 2006, "Absorption Enhancement Due to Scattering by Dipoles into Silicon Waveguides," Journal of Applied Physics, **100**, pp. 044504.

[116] Sudiarta, I. W., and Chylek, P., 2001, "Mie-Scattering Formalism for Spherical Particles Embedded in an Absorbing Medium," Journal of the Optical Society of America A, **18**, pp. 1275-1278.

[117] Mundy, W. C., Roux, J. A., and Smith, A. M., 1974, "Mie Scattering by Spheres in an Absorbing Medium," J. Opt. Soc. Am, **64**, pp. 1593-1597.

[118] Johnson, P. B., and Christy, R. W., 1972, "Optical Constants of the Noble Metals," Physical Review B, **6**, pp. 4370-4379.

[119] Doyle, W. T., 1958, "Absorption of Light by Colloids in Alkali Halide Crystals," Physical Review, **111**, pp. 1067-1072.

[120] Granqvist, C. G., and Hunderi, O., 1977, "Optical Properties of Ultrafine Gold Particles," Physical Review B, **16**, pp. 3513-3534.

[121] Jackson, J. D., 1999, *Classical Electrodynamics*, Academic, New York.

[122] Prodan, E., Radloff, C., Halas, N. J., and Nordlander, P., 2003, "A Hybridization Model for the Plasmon Response of Complex Nanostructures," Science, **302**, pp. 419-422.

[123] Kongtragool, B., and Wongwises, S., 2003, "A Review of Solar-Powered Stirling Engines and Low Temperature Differential Stirling Engines," Renewable and Sustainable Energy Reviews, **7**, pp. 131-154.

[124] Steinfeld, A., 2005, "Solar Thermochemical Production of Hydrogen—a Review," Solar Energy, **78**, pp. 603-615.

[125] Harding, G. L., 1976, "Sputtered Metal Carbide Solar-Selective Absorbing Surfaces," Journal of Vacuum Science and Technology, **13**, pp. 1070.

[126] Granqvist, C. G., 1981, "Radiative Heating and Cooling with Spectrally Selective Surfaces," Applied Optics, **20**, pp. 2606-2615.

[127] Zhang, Q. C., 1998, "Metal-Aln Cermet Solar Selective Coatings Deposited by Direct Current Magnetron Sputtering Technology," Journal of Physics D, Applied Physics(UK), **31**, pp. 355-362.

[128] Yin, Z. Q., and Harding, G. L., 1984, "Optical-Properties of Dc Reactively Sputtered Thin-Films," Thin Solid Films, **120**, pp. 81-108.

[129] Harding, G. L., Yin, Z. Q., Craig, S., and Chow, S. P., 1984, "Sputtered Solar Selective Absorbing Surfaces Based on Aluminum and Stainless-Steel Composites," Solar Energy Materials, **10**, pp. 187-207.

[130] Mcdonald, G. E., 1974, "Spectral Reflectance Properties of Black Chrome for Use as a Solar Selective Coating," Technical Report No. N-30121, National Aeronautics and Space Administration, Lewis Research Center, Cleveland, Ohio (USA).

[131] Andersson, Å., Hunderi, O., and Granqvist, C. G., 1980, "Nickel Pigmented Anodic Aluminum Oxide for Selective Absorption of Solar Energy," Journal of Applied Physics, **51**, pp. 754.

[132] Adsten, M., Joerger, R., Järrendahl, K., and Wäckelgård, E., 2000, "Optical Characterization of Industrially Sputtered Nickel–Nickel Oxide Solar Selective Surface," Solar Energy, **68**, pp. 325-328.

[133] Garnett, J. C. M., 1904, "Colours in Metal Glasses and in Metallic Films," Philosophical Transactions of the Royal Society of London, Series A, **203**, pp. 385-420.

[134] Bruggeman, D. A. G., 1935, "The Calculation of Various Physical Constants of Heterogeneous Substances. I. The Dielectric Constants and Conductivities of Mixtures Composed of Isotropic Substances," Ann. Phys, **24**, pp. 132.

[135] Yin, Y., and Collins, R. E., 1995, "Optimization and Analysis of Solar Selective Surfaces with Continuous and Multilayer Profiles," Journal of Applied Physics, **77**, pp. 6485.

[136] Tao, R., Chen, Z., and Sheng, P., 1990, "First-Principles Fourier Approach for the Calculation of the Effective Dielectric Constant of Periodic Composites," Physical Review B, **41**, pp. 2417-2420.

[137] Ritchie, I. T., and Window, B., 1977, "Applications of Thin Graded-Index Films to Solar Absorbers," Applied Optics, **16**, pp. 1438-1443.

[138] Window, B., Mckenzie, D., and Harding, G., 1980, "Selective Absorber Design," Solar Energy Materials, **2**, pp. 395-401.

[139] Craig, S., and Harding, G. L., 1983, "Composition, Optical-Properties and Degradation Modes of Cu (Graded Metal-Carbon) Solar Selective Surfaces," Thin Solid Films, **101**, pp. 97-113.

[140] Zhang, Q. C., and Mills, D. R., 1992, "New Cermet Film Structures with Much Improved Selectivity for Solar Thermal Applications," Applied Physics Letters, **60**, pp. 545.

[141] Farjadpour, A., Roundy, D., Rodriguez, A., Ibanescu, M., Bermel, P., Joannopoulos, J. D., Johnson, S. G., and Burr, G. W., 2006, "Improving Accuracy by Subpixel Smoothing in the Finite-Difference Time Domain," Optics Letters, **31**, pp. 2972-2974.

[142] Ung, B., and Sheng, Y., 2007, "Interference of Surface Waves in a Metallic Nanoslit," Optics Express, **15**, pp. 1182-1190.

[143] Zhang, Z., 1999, "Fabrication, Characterization and Transport Properties of Bismuth Nanowire Systems," Ph.D. thesis, Massachusetts Institute of Technology, Cambridge, MA.

[144] Lin, Y. M., 2003, "Thermoelectric Properties of $Bi_{1-X}sb_x$ Nanowires and Lead Salt Superlattice Nanowires," Ph.D. thesis, Massachusetts Institute of Technology, Cambridge, MA.

[145] Wäckelgård, E., 1996, "A Study of the Optical Properties of Nickel-Pigmented Anodic Alumina in the Infrared Region," Journal of Physics: Condensed Matter, **8**, pp. 5125-5138.

[146] Tesfamichael, T., and Roos, A., 1998, "Treatment of Antireflection on Tin Oxide Coated Anodized Aluminum Selective Absorber Surface," Solar Energy Materials and Solar Cells, **54**, pp. 213-221.